

Hardware-Tailored Resource Estimation for Magic-State Distillation on Silicon Spin Qubits

Songqinghao Yang,^{1,2} Christopher K. Long,^{1,2} Rubén M. Otxoa,²

Prakash Murali,³ Crispin H. W. Barnes,¹ and David R. M. Arvidsson-Shukur²

¹*Cavendish Lab., Department of Physics, Univ. of Cambridge, Cambridge CB3 0HE, UK*

²*Hitachi Cambridge Lab., J.J. Thomson Avenue, Cambridge CB3 0HE, UK*

³*Department of Computer Science and Technology, Univ. of Cambridge*

(Dated: May 29, 2026)

We present a resource analysis for generating high-fidelity logical magic states on silicon spin-qubit platforms. We consider a range of architectures, including a shuttling-based SpinBus design, a dense nearest-neighbor layout, and a hybrid scheme with shuttling-connected patches. We compare surface, color, and biased error-correcting codes, and analyze the $5 \rightarrow 1$ and $15 \rightarrow 1$ magic-state distillation protocols. Our approach combines bottom-up and top-down methodologies. We construct a hardware-level noise model based on a silicon-processor Hamiltonian with realistic parameters and $1/f$ non-Markovian noise, enabling estimation of physical resources required to reach target logical error rates. These results are propagated to system-level overheads for applications including spin dynamics, integer factorization, and quantum chemistry. Conversely, we fix target logical fidelities and derive corresponding constraints on hardware performance. Our framework enables systematic evaluation of resource-reduction strategies. We find that optimized control pulses reduce magic-state distillation overhead by 42% compared to standard gate implementations. In addition, silicon-tailored biased error-correcting codes achieve an approximately threefold reduction in physical footprint relative to the surface code, even without physical-bias-preserving operations.

I. INTRODUCTION

Quantum computers process information in ways that are fundamentally different from classical computers, offering the prospect of advances in cryptography [1, 2], Hamiltonian simulation [3–5], computational chemistry [6–8], and optimization [9, 10]. Rapid experimental progress across multiple platforms has led to steady improvements in qubit number, wall-clock time, and control fidelity, strengthening the case for scalable quantum computation [11–13]. However, current quantum hardware remains intrinsically noisy: decoherence and control imperfections prevent reliable execution of complex algorithms [14–20].

Scalable quantum computation, therefore, requires fault-tolerant architectures based on quantum error correction (QEC) [21–26]. Recent years have seen several platforms take steps towards fault-tolerant architectures [27–30]. In such architectures, logical qubits are encoded in multiple physical qubits. As long as the input states are restricted to stabilizer states and the operations to Clifford gates and Pauli measurements, standard QEC protocols actively detect and correct errors during computation. While QEC enables the detection and correction of noise, it does not provide a complete solution for universal quantum computation. In particular, Clifford gates and Pauli measurements are not universal [31]. To harness the full power of quantum computation, one needs access to non-Clifford operations.

Magic-state distillation (MSD) provides one path to promote error-corrected quantum computers to universal ones [32–39]. In MSD, noisy (non-stabilizer) magic

states are prepared at the physical-qubit level. These states are then injected into the hardware’s logical space. In the logical space, the magic states are distilled to improve their fidelity. After the fidelity reaches some target value, the magic states can be injected into the error-corrected computer to implement high-fidelity non-Clifford operations, thus enabling universal quantum computing [38, 40]. Recent proof-of-principle experimental work has demonstrated high-fidelity preparation and distillation of logical magic states on error-corrected qubits [41, 42].

In the last years, several studies have estimated the resources needed to utilize fault-tolerant hardware. These studies consider the total number of physical qubits and the wall-clock time needed to implement a specific quantum algorithm [13, 43–51]. Typically, the QEC and MSD protocols utilized in a specific implementation are identified as the major contributors to the computational overhead. The overheads incurred by a certain MSD protocol can only be quantified in light of a specific QEC protocol, and *vice versa* [39, 52]. Moreover, noise profiles and qubit-connectivity architectures vary widely across such platforms, with direct implications on the suitability of various QEC and MSD protocols. Thus, to attain the highest accuracy in resource estimation, one must consider the specific physical platform in which the quantum hardware is implemented. Previous works have estimated quantum-computational resources for quantum computation with neutral atoms [53, 54], photons [46, 55], and superconducting qubits [56, 57]. However, to the best of our knowledge, no thorough resources estimation has been conducted for quantum computation with electron-

spin qubits in silicon.

Quantum-computing hardware with electron-spin qubits in silicon was originally proposed in the seminal work of Loss and DiVincenzo [58]. Currently, such hardware is experiencing a surge in research interest [59–72]. In Loss-DiVincenzo processors, single electrons are trapped in arrays of gate-based quantum dots within a silicon substrate embedded in a semiconductor heterostructure [73, 74]. The spin of these electrons encode the physical qubits. A main selling point is the small spatial footprint of the physical qubits (tens of nanometers [75–78]). Moreover, the processors are compatible with current industrial production lines for CMOS and advanced semiconductor technologies, as well as with classical control electronics [77, 79, 81–84]. Spin qubits in silicon can have long T_1 times (around 1 ms to 1 s [66, 79, 85]) and T_2^* times (around 10 to 100 μ s [79]). Current gate fidelities are competitive [86–90] with 99.9% [91–94] for two-qubit operations and up to 99.999% [95, 96] for single-qubit operations. Earlier concerns about silicon spin-qubit connectivity have been partially alleviated by the demonstration of coherent electron shuttling over micrometer distances [97–99] at fidelities surpassing 99.5% over 10 μ m [100]. To summarize, electron spin-qubits in silicon provide a competitive platform for future quantum computation.

Motivated by these considerations, we present a hardware-tailored resource analysis of logical magic-state production in silicon spin-qubit architectures. We evaluate different physical-qubit-connectivity models, QEC codes and distillation protocols. With hardware-tailored noise modeling, we estimate the resulting space-time volumes for MSD. This allows us to estimate also the overheads for the implementation of specific quantum algorithms. Going beyond resource estimation, we also invert the analysis: for a target logical magic-state fidelity, we identify the corresponding hardware requirements on the physical noise and operational parameters. Thus, we can study the effect of hardware or software improvements on the resource budget for a specific algorithm. In particular, we gauge the potential resource benefits of using silicon-tailored QEC codes compared to standard QEC protocols. Together, our results clarify the tradeoffs between connectivity models, QEC codes, and MSD protocols in silicon spin-qubit systems. Further, our work provides a package for the analysis of experimental bottlenecks and a testbed for the construction and evaluation of new QEC and MSD protocols.

The remainder of this Article is structured as follows. In Sec. II, we summarize our study’s computational pipeline and main results. In Sec. III we provide background material for the silicon hardware (physical level) as well as the MSD and QEC protocols (logical level) studied in this work. In Sec. IV, we detail our methodology for pulse design and optimization. In Sec. V we present our noise analysis. And in Sec. VI we provide

MSD resource overheads. Finally, in Secs. VII, we discuss future directions and conclude our work.

II. MAIN RESULT

Here, we give a brief summary of our work. We start by describing the hardware and software settings which we analyze. Then, we outline our main findings. The goal of our work is to address the question:

Assuming that current experimental results on small-scale devices can be scaled up, what experimental resources will be needed to run quantum algorithms on silicon hardware?

To answer this question, we construct the following pipeline, illustrated in Fig. 1:

1. First, we identify the quantum algorithm that we aim to execute on a silicon spin-qubit quantum computer. We investigate three prototypical algorithms for quantum dynamics, integer factoring and quantum chemistry; details are given in Sec. VI C. The target algorithm is cast in terms of a logical circuit.
2. Next, we determine the target algorithm’s logical implementation by fixing (1) the form of logical operations (lattice surgery or transversal gates), (2) the QEC code (color, standard surface, or XZZX surface), and (3) the MSD protocol ($5 \rightarrow 1$ or $15 \rightarrow 1$). Further details are given in the Sec. III.
3. After completing the logical compilation, we select a silicon spin-qubit architecture. We consider three architectures: a dense 2D-grid layout, a shuttling-mediated SpinBus architecture, and a hybrid ‘patched’ layout (Sec. III A).
4. We then convert the logical circuits into physical circuits. We do so by optimizing hardware control pulses for the required circuit components (Sec. IV A). Our pulse optimizer considers a realistic silicon-device Hamiltonian and compresses pulses using the GRAPE algorithm. In conjunction with this analysis, we construct a noise and timing model that accounts for the device-specific decoherence times, with either Markovian noise or the $1/f$ -type temporal noise commonly observed in silicon devices [101, 102], shuttling-induced errors, and operational latency (Sec. V).
5. Finally, having mapped out a pipeline from the target algorithm to the physical-level implementation, we simulate the combined resource cost of the required MSD and QEC protocols. This allows us to estimate the total resource budget needed for the target application.

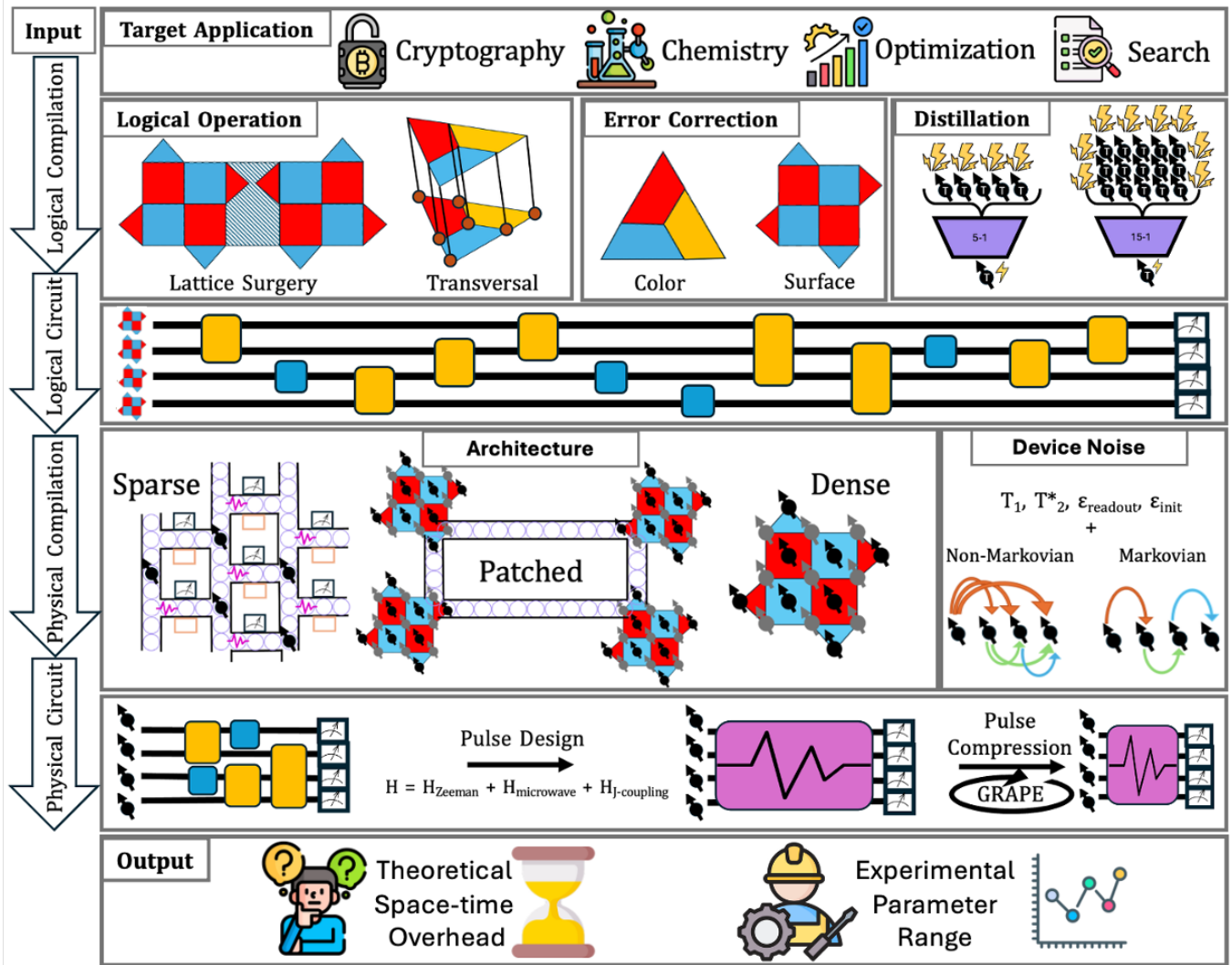


FIG. 1. **Resource-estimation pipeline.** From top to bottom: A target quantum application is compiled into a logical circuit based on the choice of (1) logical operations, (2) QEC code, and (3) MSD protocol. The logical circuits are compiled into physical circuits by considering specific hardware architectures. The relevant QEC and MSD overheads depend on a hardware-specific noise model. The physical circuits are compiled into a sequence of hardware-tailored control pulses using pulse design. We use GRAPE to optimize the controls, thereby compressing the pulse sequence and potentially reducing errors and runtime. Finally, we produce theoretical resource metrics—space-time volume, physical-qubit overhead, runtime—and experimental bounds and target ranges for device parameters—*e.g.*, required coherence times, gate fidelities, and operation timing thresholds.

Figure 2 shows the physical-qubit footprint of three representative quantum algorithms—quantum dynamics, Shor’s factoring (where we follow the logical construction from [2]), and quantum chemistry—as a function of computation time. We restrict the analysis to the dense architecture operated with the standard surface code and the sparse architecture operated with either the standard or the XZZX surface code. We demonstrate our framework on these popular and well-studied QEC schemes. However, our techniques are readily adaptable to other QEC schemes, which may reduce overheads. The noise model is described in Sec. V B. Moreover, we plot data only for

lattice-surgery operations and the $15 \rightarrow 1$ MSD protocol. A detailed comparison between alternative protocols is deferred Secs. VIB. The resource overheads reported in Fig. 2 can be considered as estimates of upper bounds: The data are produced using present-day physical parameters (see Tab. I) and can be improved by advances in algorithms and optimization techniques as well as by hardware and architecture advances. However, the resource estimates are also somewhat optimistic in that we assume that the demonstration of individual high-fidelity gates and shuttling can be scaled up efficiently to cover the entire hardware. For example, we assume that state-

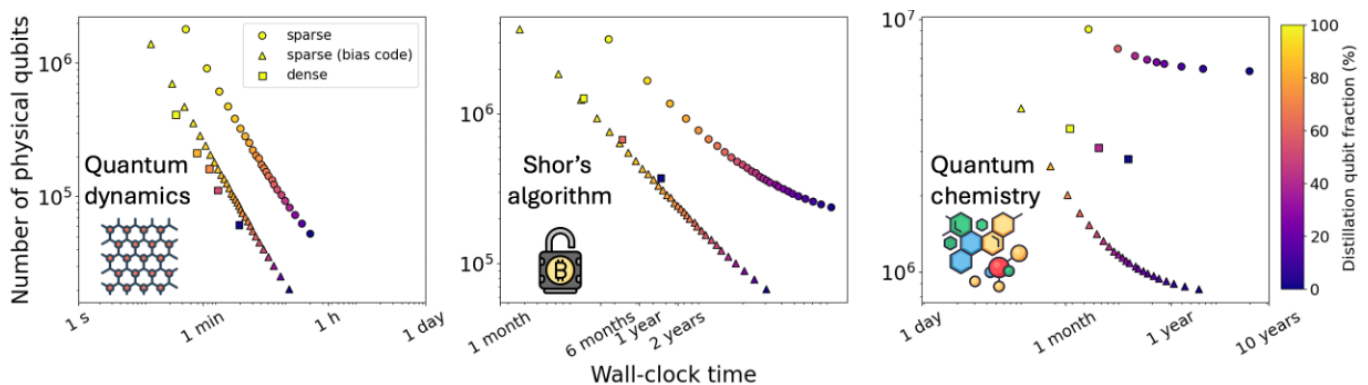


FIG. 2. **Algorithmic resource requirements.** We plot the wall-clock time (horizontal axis) and the number of physical qubits (vertical axis) needed to run three different quantum algorithms. The color map indicates the fraction of the qubits used for MSD. The circles label the sparse SpinBus architecture with the standard surface code; the triangles label the SpinBus architecture with the XZZX surface code; and the squares label the dense architecture with the standard surface code. The logical operations are implemented with lattice surgery and the ‘grow-and-distill’ MSD protocol is chosen to minimize the space-time overhead.

of-the-art shuttling fidelities will improve by an order of magnitude. Such improvements are necessary to enable the implementation of standard scalable QEC codes on shuttling-based processors. Moreover, we consider only first-order errors in the MSD process and ignore the effect of higher-order errors.

From Fig. 2, several trends emerge. The architecture with dense connectivity and fully local operations exhibit significantly lower space-time overheads than shuttling-based (sparse) layouts. This is intuitive as sparse architectures allocate additional runtime to qubit shuttling and shuttling-induced errors increase the resources required for error correction. Moreover, across all three applications, the execution time can be reduced by parallelizing MSD at the expense of a larger physical-qubit footprint. Conversely, the spatial overheads can be reduced by limiting the fraction of physical qubits allocated to MSD. These findings are consistent with the observation that MSD dominates the resource cost in the fault-tolerant architectures that we study. Whilst the dense architecture clearly outperforms the sparse one, practical wiring issues, etc., place the actual production of a dense platform well beyond current capabilities. It is, therefore, re-assuring to see that significant resource reductions can be obtained by means of improved and hardware-tailored software. We demonstrate this with our simulations of the sparse architecture with the XZZX code. Unlike the standard surface code, the XZZX code’s performance benefits from the biased nature of noise, inherit to Silicon spin qubits. The use of the XZZX code significantly improves the space-time overheads of all three algorithms.

In Sec. VIB, we analyze the aforementioned trends in more detail. We demonstrate how variations in hardware parameters directly affect the MSD resource overhead. We also introduce several techniques to reduce this overhead, including pulse-level optimization and the use

Parameter	Range	Default Value	Units	Refs
T_1	0.01–1	0.1 s		[66, 79]
T_2^*	10–1000	100 μ s		[66, 79]
t_I	1–100	50 ns		[92, 93, 96]
t_{II}	10–1000	225 ns		[92, 93, 96]
t_{readout}	0.1–10	1 μ s		[103–105]
t_{init}	0.01–1	0.1 μ s		[106]
ϵ_{defect}	0.01–1	0.1 %		—
v_{shuttle}	—	8 m/s		[107]
N_{hops}	10–100	10 dots		[107]
d_{dot}	—	100 nm		[107]
$\epsilon_{\text{readout}}$	—	0.01 %		[104, 106]
$\epsilon_{\text{shuttle}}$	—	0.001 %		[100]

TABLE I. **Summary of parameters for silicon hardware.** The ‘‘Range’’ column denotes the parameters’ typical range observed across experiments; the ‘‘Default Value’’ column specifies the values we used to produce the data in Fig. 2. We used the lower and upper values in the range for our optimistic and pessimistic analyses, respectively. T_1 and T_2^* denote the relaxation and inhomogeneous dephasing times, respectively. t_I and t_{II} denote the implementation times for high-fidelity single- and two-qubit gates. t_{readout} and t_{init} denote the readout and initialization times. ϵ_{defect} denotes the percentage of faulty quantum dots that incur re-routing overheads. v_{shuttle} denotes the average electron-shuttling speed and N_{hops} denotes the average number (plus one) of empty dots between separated physical qubits in the sparse and patched architectures. d_{dot} denotes the average quantum-dot separation. $\epsilon_{\text{readout}}$ and $\epsilon_{\text{shuttle}}$ denote the error probabilities of a single-spin readout and a shuttling operation over one quantum dot, respectively. To enable QEC simulations, we used a default value of $\epsilon_{\text{shuttle}}$ ten times smaller than the current state-of-the-art realisations [100].

of biased QEC codes. We benchmark these approaches across different hardware architectures and consistently observe that dense layouts outperform sparse architec-

tures in terms of resource overhead. In addition, we compare the performance of different QEC codes and MSD protocols. For example, we demonstrate the resource advantage of the $15 \rightarrow 1$ distillation protocol over the $5 \rightarrow 1$ protocol.

III. BACKGROUND

In this section, we first introduce our architectural models. Then we briefly outline the QEC codes we investigate. Finally, we summarize the MSD protocols used for benchmarking.

A. Architectural Motivation

To structure our resource analysis, we focus on three architectural regimes that span reasonable designs of silicon spin-qubit processors. The three architectures are not intended as an exhaustive list of possible blueprints, but as representative designs aimed at addressing the key hardware tradeoffs of connectivity, shuttle overhead, wiring complexity, and fidelity optimization. The SpinBus architecture [88, 97, 107–112] captures a sparse, shuttle-dominated regime closest to near-term experimental demonstrations and highlights the cost of long-range transport. The patched architecture represents an intermediate design in which local dense regions are embedded within a globally sparse design, enabling efficient local error correction while requiring shuttling for logical operations. This layout is inspired by Ref.[59] where shuttling connectivity is advocated to reduce the hardware burden of readout and power dissipation, *etc.* Finally, the dense architecture serves as an optimistic upper bound on future silicon-hardware architectures. In the dense architecture, all spin qubits are coupled via nearest-neighbor connectivity, and the need for shuttling is eliminated. The performance of the dense and patched architectures may be further enhanced by reducing operation times with pulse-level optimization (Sec. IV A). By producing resource estimates for these three designs, we can systematically assess the impact of the hardware architecture on silicon quantum computing.

SpinBus architecture: sparse, shuttling-mediated

The small physical footprint of silicon spin qubits is both a blessing and a curse. In principle, a small qubit size allows for a large number of qubits to be integrated on the same chip and fitted into a reasonably sized dilution refrigerator. However, if electron-spin qubits are packed densely on a chip, there are major implications for the possibility of adequate wiring of the control electronics. The **SpinBus** architecture [88, 97, 107–112] was

designed to overcome these difficulties. The architecture relies on a sparse connectivity regime in which several empty quantum dots sit between quantum dots occupied by electron-spin qubits. To facilitate computation, the electrons are coherently transported along shuttling lanes that connect regions with initialization and readout zones, as in Fig. 3. Typical distances between dots are on the order of ~ 10 – 100 nm, while straight shuttling lanes span lengths of $L \sim 1$ μm . This corresponds to approximately $N_{\text{hops}} \approx 10$ discrete movements over quantum dots per connectivity lane. Assuming a coherent shuttling velocity of $v \approx 8 \text{ m s}^{-1}$, the transit time for a single lane is $t_{\text{lane}} = L/v \approx 125$ ns, or $t_{\text{step}} \approx 12.5$ ns per hop [107].

Experimental results suggest that coherent spin-qubit transfer over one hop can be achieved with an overall infidelity on the order of 10^{-4} [100]. Optimistically, we set the per-dot shuttling error to be $\epsilon_{\text{shuttle}} \sim 10^{-5}$. When shuttling around corners or T-junctions, the incurred infidelity rises by roughly a factor of 4 [107]. In the SpinBus architecture, physical single-qubit operations are performed locally in manipulation zones using electric-dipole-spin-resonance (EDSR) pulses [107, 108]. Physical two-qubit gates are typically implemented via exchange interactions between physical qubits that have been shuttled to neighboring quantum dots. A typical stabilizer cycle (see Sec. III D), therefore, consists of ancillae initializations, multiple shuttling segments interleaved with local interactions, and a return shuttle that enables measurements in the readout zones.

Patched architecture: semi-dense layout

The **patched** architecture in Fig. 4 interpolates between sparse and dense regimes by partitioning the processor into locally dense patches connected by a reduced number of shuttling lanes [59]. Within each patch, physical single- and two-qubit operations are executed locally using EDSR and exchange coupling, respectively. The operations implemented on a specific patch can be compressed in time using pulse-level optimization (Sec. IV A). In this work, we consider the encoding of one or two logical qubits per patch. The number of physical qubits we consider per patch thus ranges from 17 (in a distance 3 rotated surface code) to 841 (in a distance 21 unrotated surface code). During the MSD process, the patch size is fixed at the number of physical qubits needed to implement the logical qubit with the largest code distance.

Inter-patch operations, including long-range logical interactions and MSD-factory routing, rely on SpinBus shuttling. Moreover, the separation of local and global operations simplifies modeling: local gates are treated as directly-connected operations subject to pulse compression, while inter-patch transfers incur the same shuttling

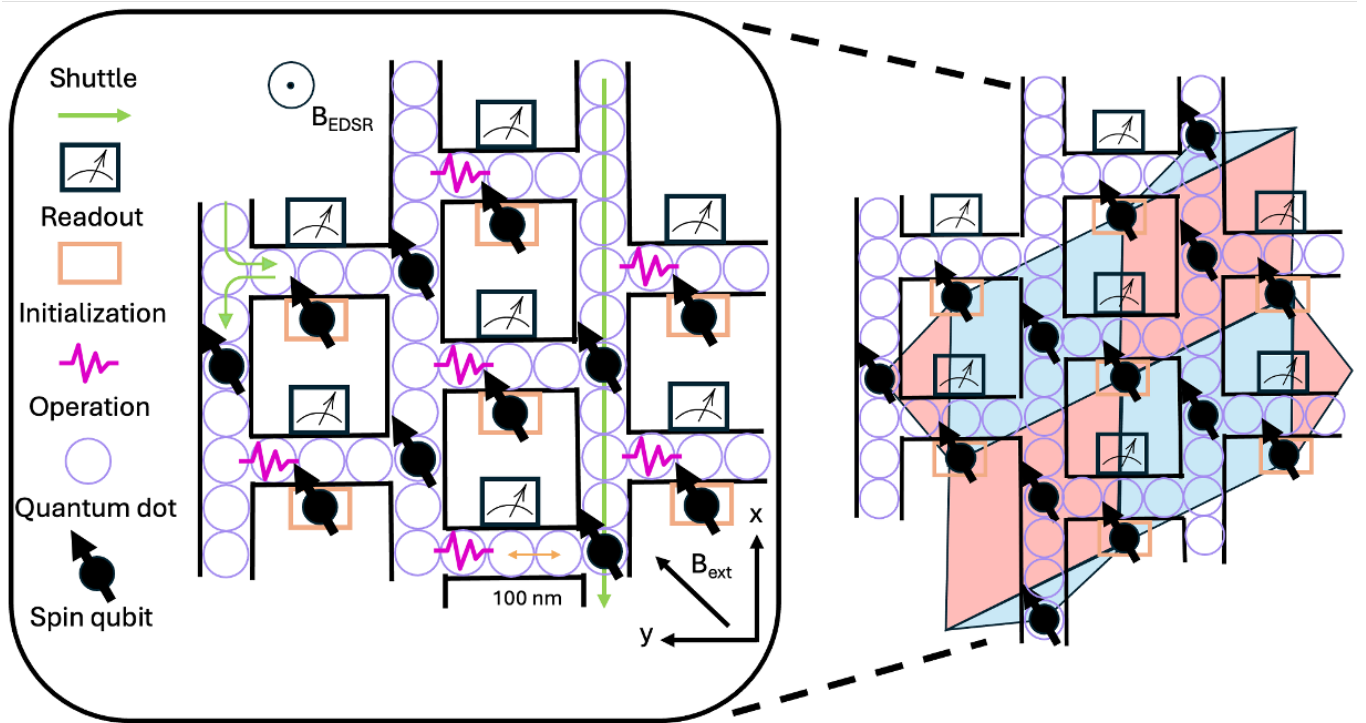


FIG. 3. **Sparse SpinBus architecture.** (Left) Hollow circles represent quantum dots and dark dots represent physical spin qubits. The parallel lines represent shuttling channels. An external magnetic field is applied in-plane in the diagonal direction to avoid bias in the x - and y -directions. Single-qubit operations are enabled by the magnetic field perpendicular to the plane. Qubit initializations, operations, and readout are conducted in their designated manipulation zones. (Right) Mapping of a rotated surface code onto the sparse architecture.

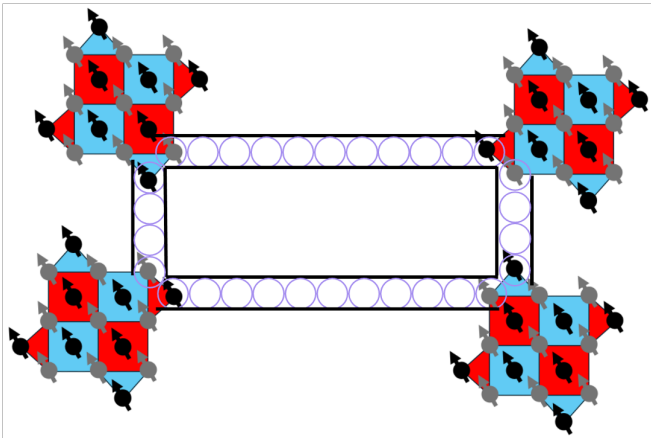


FIG. 4. **Patched architecture.** m logical qubits (here, we show $m = 1$ logical qubits at distance 3) are encoded onto the densely connected physical qubits within each patch. The logical qubits are interconnected via shuttling channels.

penalties as in the sparse architecture. Thus, the patched architecture, significantly reduces the average shuttling overheads while retaining many of the wiring and integration advantages of sparse layouts. For example, stabilizer cycles require substantially fewer shuttling operations compared to the sparse architecture. A comparison

between the space-time volume needed for one MSD factory in the sparse and patched architectures is shown in Fig. 5. Clearly, the resource benefits of the patched architecture increases as the fraction of physical qubits with a dense connectivity (or the number of logical qubits per patch) increases.

Dense architecture: good connectivity, bad wiring

The **dense** architecture represents a hardware-optimistic operating regime in which silicon spin qubits are arranged in a two-dimensional nearest-neighbor lattice with native exchange coupling available between all adjacent sites [75]. See Fig. 6. In the dense architecture, all logical operations—syndrome extraction, lattice surgery, and MSD—can be executed locally without explicit shuttling. Pulse-level optimization (Sec. IV A) can be applied directly to the underlying Hamiltonian controls used for all physical operations. Consequently, all physical operations can be implemented in times near the minimal evolution time in silicon structures [113]. This substantially suppresses errors, making the dense layout the theoretically ideal setting for high-quality-output MSD factories.

However, from an experimental perspective, the dense

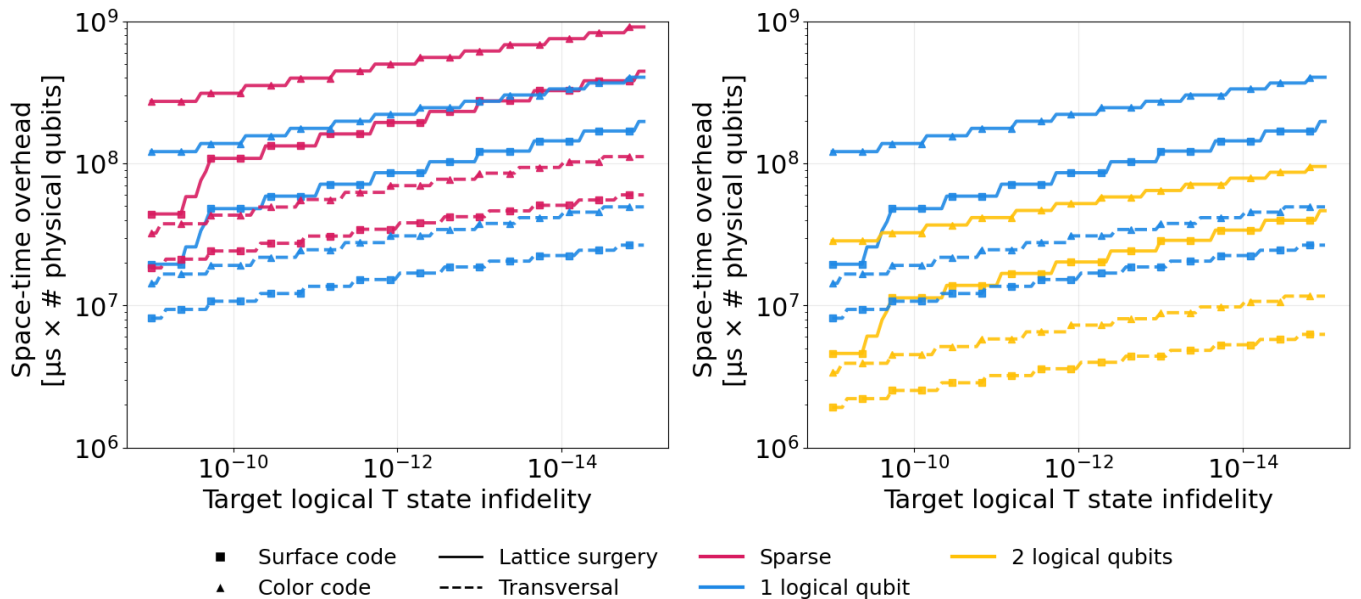


FIG. 5. **Space-time volume required for one MSD factory.** Space-time overhead reduction relative to baseline (sparse layout). We study sparse (separated) physical qubits and patched architectures where 1 or 2 logical qubits are one the same dense patch and direct pulse operations generate the desired evolutions. On the vertical axis we have the space-time overhead in unit of microseconds times the number of physical qubits.

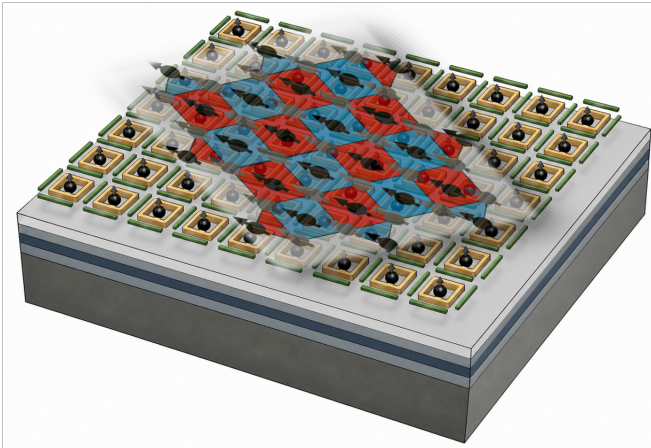


FIG. 6. **Dense architecture.** A schematic of the silicon spin-qubit quantum processor. A global external magnetic field, which generates a Zeeman splitting, lies along the 2D array of the qubits. Plunger (brown square plates) and barrier (green outlines) gates create an electronic potential which traps individual electrons in the potential wells of gate-defined quantum dots. The Hamiltonian description of the device is given in Eq. (7). For illustrative purposes, a small portion of surface code is projected on top of the array.

architecture is often regarded as hypothetical. This is predominantly related to the fact that silicon spin qubits are far smaller than the spatial footprint of control and readout electronics. If the number of control lines needed per physical qubits is constant with the size of the pro-

cessor, then the dense architecture is not scalable to the size needed for fault-tolerant computing. The number of interconnects and cryogenic I/O channels [64] grows too rapidly and quickly exceeds practical limits set by chip area and packing constraints [114]. To implement a dense silicon-qubit architecture one must address the wiring issues that currently limit the scalability of solid-state quantum processors.

Proposed solutions to these issues rely on multiplexing of control lines and sparse readout strategies that trade spatial density for wiring efficiency [114]. While such approaches can dramatically reduce the effective wiring overhead, there are yet no experimental realizations at the scales needed for fault-tolerant quantum computing. Moreover, the proposed solutions introduce additional layout complexity, power dissipation, and control serialization. Consequently, we view the dense architecture as a forward-looking benchmark rather than as a near-term design target.

In our analysis, the dense layout serves two purposes. First, it provides an architectural best-case reference point against which the costs imposed by shuttling, routing, and operations in more practical architectures can be quantified. Second, it allows us to isolate and study the benefits of pulse-level compilation in the absence of shuttling overhead.

B. Quantum error correction and thresholds

Quantum error correction (QEC) codes protect quantum information by encoding a number of logical qubits onto a larger number of physical qubits and repeatedly detecting and correcting errors through measurements [115]. A common class of QEC codes is the stabilizer codes.

Typically, a stabilizer code is defined by a set of commuting (Pauli) operators acting on subsets of the *data qubits* (which hold the logical information). The protected code space corresponds to the simultaneous $+1$ eigenspace of these stabilizers. Experimentally, the stabilizer observables are measured indirectly using *ancilla* qubits that couple to the data qubits through controlled operations. Measurements of the ancilla qubits produce outcomes corresponding to the stabilizer eigenvalues, from which an error syndrome can be extracted. Each round of syndrome extraction produces an error syndrome, which is decoded on classical hardware. The decoded syndrome specifies how to correct the physical errors. Repetition of this process suppresses the accumulation of errors and stabilizes the logical qubits over times exceeding the coherence of the underlying hardware.

Two central concepts for any QEC code are the *distance* d and the *threshold error rate* p^* [116]. The code distance is defined as the smallest number of physical qubits that must be corrupted to cause an undetectable logical error. Increasing the code distance at the expense of more physical qubits suppresses the logical-error probability exponentially. However, a QEC code suppresses errors only when the physical error rate p is below the threshold p^* . Then, the logical error rate p_L is approximated by

$$p_L \approx A \left(\frac{p}{p^*} \right)^{(d+1)/2}. \quad (1)$$

Here, A is a code- and decoder-dependent constant. While Eq. (1) provides only an approximation which may break under certain noise profiles, it does highlight the hardware-parameter cutoff ($p < p^*$) for which fault-tolerant quantum computation is possible.

Among two-dimensional stabilizer codes, the surface code [26] and the color code [117–119] are leading candidates for solid-state platforms. In the unrotated surface code, a distance- d logical qubit is encoded using d^2 physical data qubits arranged on a square lattice. Surface codes combine strictly local connectivity, high thresholds, and efficient decoding, which makes them well suited for current hardware. Triangular color codes encode one logical qubit using $(3d^2 - 1)/4$ physical data qubits, achieving a high encoding rate at the cost of larger stabilizer weights and typically small values of p^* . (The stabilizer weight is the number of qubits on which a stabilizer operator acts nontrivially.) Higher-weight stabilizers typically

enforce stronger parity constraints across larger regions of the QEC code's lattice. However, high-weight stabilizers require ancilla qubits to interact with more data qubits during the syndrome extraction. This leads to more opportunities for gate errors to propagate to multiple qubits (*e.g.*, hook errors [120]).

C. Biased codes

The XZZX surface code is a variant of the conventional surface code. It offers remarkable performance under biased noise where one type of Pauli error occurs more frequently than others [121–126]. The noise profile of semiconductor spin qubits is precisely of such a form, with dephasing noise being the dominant error mechanism. The XZZX code is locally equivalent to the standard surface code [121] but differs by a Hadamard rotation on alternate qubits, resulting in stabilizer operators that are the product XZZX of Pauli operators around each face of a square lattice of physical qubits.

To summarize the performance of the XZZX code, we recall the general single-qubit Pauli noise channel:

$$\mathcal{E}(\rho) = (1 - p)\rho + p(r_X X\rho X + r_Y Y\rho Y + r_Z Z\rho Z), \quad (2)$$

where $p \in [0, 1]$ is the error probability and $\mathbf{r} = (r_X, r_Y, r_Z)$ is a positive vector, with unit L_1 norm, that characterizes the noise profile. For (Z-biased) biased noise, the bias parameter is defined by

$$\eta = \frac{r_Z}{r_X + r_Y}, \quad (3)$$

with $r_X = r_Y$, such that $\eta = 1/2$ corresponds to depolarizing noise and $\eta \rightarrow \infty$ corresponds to completely Z-dominated noise. Following the result from [121], where the logical error rate is damped by a factor of $\sim \eta^{-d/4}$, we assume the following model:

$$p_L \approx A_z \left(\frac{p}{p_z^*} \right)^{(d_z+1)/2} + A_x \left(\frac{p}{p_x^*} \right)^{(d_x+1)/2} \quad (4)$$

with d_X and d_Z being the code distance in the logical X and Z directions, respectively. In silicon electron-spin processors, the Z errors dominate the X errors. By splitting up the logical error rate into the X direction and the Z direction, one can allocate fewer resources (a smaller code distance and thus fewer physical qubits) to the X direction. This amounts to constructing a rectangular surface code where the logical X direction has a shorter length.

Spin qubits exhibit strongly asymmetric error channels where dephasing dominates over bit-flip processes [66, 127]. As a result, Pauli-Z errors occur at a higher rate than Pauli-X or Pauli-Y errors. This leads to a physical noise bias parameter reaching values $\eta \sim 10^2$ – 10^3 in

experimentally relevant regimes [66, 127]. The advantage of the XZZX code relies critically on maintaining the physical noise bias throughout the full fault-tolerant circuit. That is to say, if the implemented gate set is *bias-preserving*, meaning that it maps dominant Z errors to Z errors without symmetrizing the noise channel, then the effective bias η_{eff} remains large and the threshold continues to increase with η . By contrast, when operations are not bias-preserving, such as when Hadamard gates or CNOTs mix X and Z error channels, the effective noise seen by the code becomes more isotropic. In this case, even if the physical qubits exhibit large η , the circuit-level noise bias saturates around a factor of 5 [128]. Consequently, the fault-tolerant threshold does not increase indefinitely with physical bias.

To illustrate the potential benefits of utilizing bias-preserving QEC codes on silicon hardware, we simulate and compare the space-time volume incurred by MSD factories operating with the unrotated surface code and with the XZZX-surface code. We limit our analysis to the sparse architecture. (Similar analyses for the patched and the dense architectures would require the investigation of bias-preservation through pulse optimization.) Our results are presented in Fig. 7. Our analysis shows a clear advantage for the XZZX code for both $5 \rightarrow 1$ and $15 \rightarrow 1$ MSD factories (as defined below). For high-fidelity magic-state production, the improvement is roughly by a factor of 3 to 5.

D. Syndrome checks

Next, we summarize the syndrome-check component of QECs, illustrating this with the standard surface code. The surface code is a two-dimensional stabilizer code defined on a square lattice of data qubits. Each edge of the lattice hosts a physical qubit, while the lattice’s nodes (“vertices”) and faces (“plaquettes”) provide the locations at which stabilizer checks are applied, as shown in Fig. 8. The code performs X-type checks on vertices and Z-type checks on plaquettes. The logical states are the simultaneous $+1$ eigenstates of a set of local stabilizer operators. The stabilizer group is generated by mutually commuting operators of the form

$$A_v = \prod_{j \in \text{adjacent}(v)} X_j, \quad B_p = \prod_{j \in \text{plaquette}(p)} Z_j. \quad (5)$$

$\text{adjacent}(v)$ denotes the set of data qubits adjacent to vertex v and $\text{plaquette}(p)$ denotes the qubits surrounding plaquette p . For the unrotated surface code, these stabilizers typically have weight four inside the bulk of the device: every qubit is connected to four other qubits.

Syndrome extraction is performed by coupling each stabilizer generator to a dedicated ancilla qubit and then measuring that ancilla. Consider a Z-type plaquette sta-

bilizer $B_p = Z_1 Z_2 Z_3 Z_4$. The corresponding ancilla is initialized in the state $|0\rangle_a$ and sequentially interacts with the data qubits via CNOT gates. The data qubits act as controls and the ancilla as the target. A computational-basis measurement of the ancilla yields a syndrome bit $s \in \{0, 1\}$ such that

$$(-1)^s = \langle \psi | B_p | \psi \rangle. \quad (6)$$

This procedure projects the data qubits onto an eigenstate of B_p without revealing or altering any information about the encoded logical state. The corresponding quantum circuit for a single plaquette measurement is shown in Fig. 9. An X-type star stabilizer A_v is measured analogously but with the ancilla initialized as $|+\rangle_a$.

The execution of these stabilizer checks across the lattice yields a syndrome vector \mathbf{s} and defines a single syndrome-extraction round. This process can be parallelized. Repeating the process over time yields a space-time syndrome history $\{\mathbf{s}(t)\}$. This history is decoded to infer the most likely configuration of physical errors with regard to spatial and temporal correlations. The decoded information is then used to construct error-correcting operations.

E. Logical operations: lattice surgery and transversal gates

Logical operations between encoded qubits can be implemented using two broadly applicable methods: lattice surgery and transversal gates. These approaches differ in their connectivity requirements, time overheads, and suitability for different hardware platforms [12].

Lattice surgery is a measurement-based technique with only local interactions [26, 129]. Logical operations are performed by temporarily merging and splitting code patches and measuring joint stabilizers across their boundaries. For surface codes, a logical two-qubit gate implemented via lattice surgery typically requires $\mathcal{O}(d)$ rounds of syndrome extraction, making its space-time cost proportional to $\mathcal{O}(d^3)$. While lattice surgery is flexible and hardware-efficient, its sequential execution can limit the processor’s clock speed, especially in resource-intensive protocols such as magic-state distillation.

Transversal gates, by contrast, apply logical operations through parallel physical gates between corresponding qubits in two code blocks [130]. When available, transversal implementations can directly realize logical Clifford operations (and, in some codes, non-Clifford gates) with a constant number of syndrome extraction rounds independent of d [33]. The primary advantage of transversal operations is their low temporal overhead and high compatibility with parallelization. On the negative side, the implementation of transversal gates generally requires either long-range connectivity or the ability to dynamically reposition qubits.

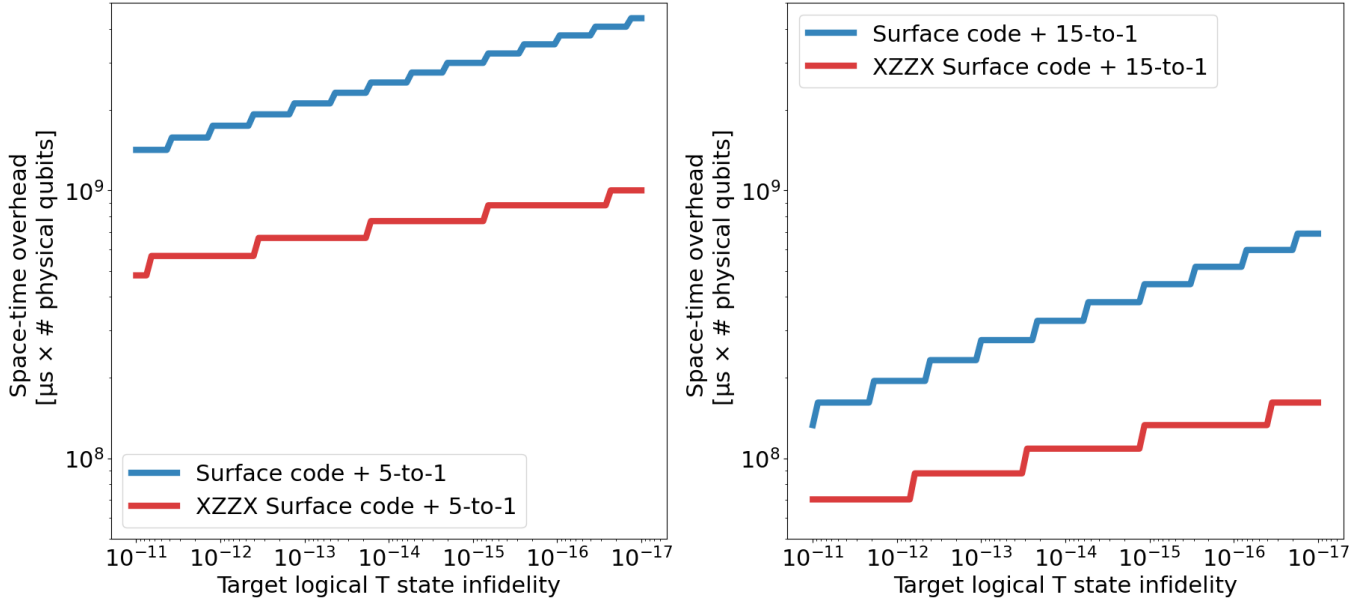


FIG. 7. **Resource cost of one magical state with and without biased surface codes.** We plot the resource cost, in terms of the space-time volume (vertical axis, in unit of microseconds times the number of physical qubits) needed to generate one logical magic state at the targeted infidelity (horizontal axis). The standard and XZZX surface codes are plotted in red and blue, respectively. The left panel analyzes the $5 \rightarrow 1$ protocol and the right one the $15 \rightarrow 1$ protocol.

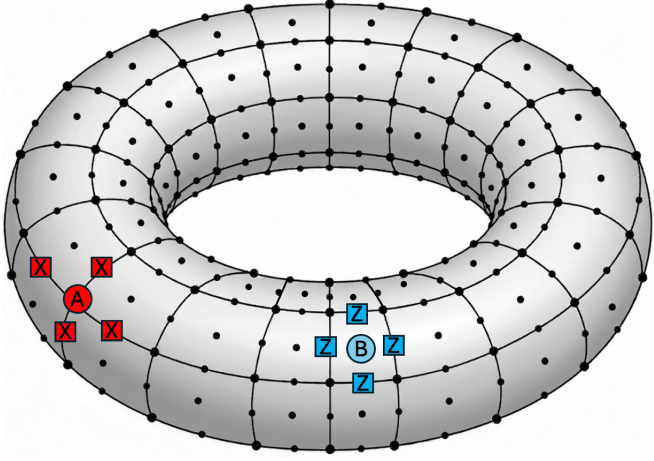


FIG. 8. **Illustration of surface code on a torus.** An illustration showing the implementation of a 2D surface code on a toroidal geometry. Two stabilizer components are highlighted: a red X-type vertex operator (A_v) at a specific vertex A, and a blue Z-type plaquette operator (B_p) on a specific plaquette B.

F. Magic-state distillation

Here, we review the workings of MSD protocol. We summarize a surface code’s performances with $[[N, k, d]]$, where N represents the total number of physical qubits on a QEC block, k represents the number of logical qubits that are protected within this block, and d represents the code distance. This triplet of parameters characterizes

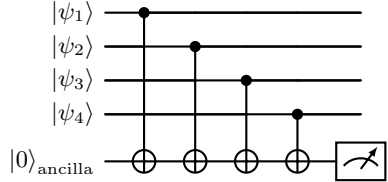


FIG. 9. **Syndrome extraction.** A circuit for QEC syndrome extraction using a Z-type plaquette stabilizer $B_p = Z_1 Z_2 Z_3 Z_4$ in the surface code.

the essential resources and power of the code, with larger N indicating more physical overhead, larger k indicating more encoded information, and larger d indicating stronger error protection.

The canonical example of a MSD protocol is the $15 \rightarrow 1$ protocol, originally introduced by Bravyi and Kitaev [33]. This protocol is based on the $[[15, 1, 3]]$ Reed-Muller code and takes 15 noisy T -type magic states (*i.e.*, non-stabilizer states $|T\rangle = (|0\rangle + e^{i\pi/4}|1\rangle)/\sqrt{2}$) as input to produce a single output magic state of higher fidelity. The protocol suppresses the output error rate from p to $\mathcal{O}(p^3)$. On the one hand, the protocol is resource intensive: it requires large qubit and circuit overheads. On the other hand, the protocol quickly improves the fidelity of the magic states.

An alternative approach is the $5 \rightarrow 1$ MSD protocol, which is based on the $[[5, 1, 3]]$ perfect stabilizer code [131–135]. This protocol consumes five noisy magic states and outputs one improved state. The protocol de-

fects single-qubit errors and implements a quadratic error suppression: $p \mapsto \mathcal{O}(p^2)$. Compared to the $15 \rightarrow 1$ protocol, the $5 \rightarrow 1$ protocol requires fewer physical qubits and uses a simpler circuit, making it an attractive candidate for early distillation demonstration [42]. Alternative codes and optimized protocols can substantially reduce the associated overhead for MSD [136–140]. In recent years, a growing body of work has demonstrated improved approaches [141–144], including code-specific optimizations [145–149] and magic-state cultivation techniques [150–155]. These techniques mitigate or circumvent conventional MSD costs. Nevertheless, we leave the study of such protocols for future work.

An important practical consideration in MSD is a protocol’s *rejection rate*. This rate is the probability that a distillation attempt is discarded due to the detection of an error during stabilizer measurements. For small input error rates ($p \ll 1$), the rejection probability scales linearly with p to leading order. However, the constant of proportionality is larger for protocols with a higher rates of error suppression. A detailed quantitative analysis of acceptance probabilities, rejection-induced overheads, and their dependence on architecture-specific noise models is deferred to later sections.

IV. METHODOLOGY

Our resource-estimation analysis is based on a theory-to-hardware pipeline that transforms a target algorithmic application into a silicon-processor-specific instruction set. By calculating the total overhead of that instruction set, we estimate the experimental resources required for the target application’s implementation. Further, we produce quantitative resource metrics for specific QEC codes and MSD protocols. In particular, we study the space-time volume, physical-qubit overhead and wall-clock runtime of quantum-computing subroutines. We also invert the analysis to calculate the experimental device performances needed to implement a subroutine within a fixed resource budget. In particular, we provide bounds on the single- and two-qubit gate fidelities, the coherence times, and the gate-implementation times needed to realize a given logical magic-state fidelity within a prescribed space-time budget.

The pipeline of the resource estimation is described in Sec. I. In the remainder of this section, we describe our device modeling and pulse-optimization techniques (Sec. IV A) and detail our results (Sec. IV B). In the next section, we describe our noise model and our techniques for evaluating MSD overheads.

A. Pulse optimization: setup

To transform an algorithm’s logical implementation into an experimental instruction set, one must model the underlying hardware. One way to produce a clock-time estimate of an algorithm is to simply add up single- and two-qubit gate times according to experimental tables. However, real hardware implements operations using control pulses. If the physical qubits are directly connected (as in dense and patched architectures), these pulses can be optimized (in time and fidelity) to implement a number of gates in one go. Thus, pulse optimization can dramatically lower the temporal resources needed to implement quantum circuits. Pulse-level optimization allows circuits, like syndrome checks, to approach their minimal durations by exploiting the full native Hamiltonian rather than a discrete gate set. This can reduce idling errors in QEC cycles and the space-time volume of distillation factories. Moreover, pulse-optimized implementations naturally incorporate hardware constraints making the modeling more realistic compared to hardware-agnostic studies [156–158]. We incorporate pulse optimization in our analysis of the dense architecture and inside the patched architecture’s dense regions. For the sparse layout, electron shuttling is used for qubit transport, which inhibits acceleration via pulse optimization.

There are several ways to simulate the implementation of quantum gates on semiconductor spin qubits [73, 159, 160]. We build our analysis around an effective Heisenberg model of a spin lattice [73]. In particular, we describe the dynamics of an N -qubit array using a driven Heisenberg Hamiltonian [73]:

$$H(t) = -\frac{1}{2} \sum_{i=1}^N B_i \sigma_z^{(i)} - \frac{1}{2} g(t) \sum_{i=1}^N \sigma_x^{(i)} + \sum_{1 \leq i < j \leq N} \frac{J_{ij}(t)}{4} \sigma^{(i)} \cdot \sigma^{(j)}, \quad (7)$$

where i, j label qubits and $\sigma^{(i)} = (\sigma_x^{(i)}, \sigma_y^{(i)}, \sigma_z^{(i)})$. The first term corresponds to the Zeeman splitting induced by the external magnetic field; the second term is the transverse microwave control, written in quadrature as

$$g(t) = \sum_{i=1}^N [I_i(t) \cos \omega_i t + Q_i(t) \sin \omega_i t]; \quad (8)$$

and the third term modulates the exchange couplings with $J_{ij}(t)$. Herein, we consider both linear and 2D arrays. We enforce this connectivity by fixing $J_{ij}(t) = 0$ for unconnected pairs of qubits. We define our qubits in the rotating frame of the first term. Using this Hamiltonian, we can emulate the effect of hardware pulses on the spin qubits using a Suzuki-Trotter algorithm [161, 162] adapted to the Heisenberg Hamiltonian as in Refs. [113, 163, 164]. Our emulator employs

the rotating wave approximation; thus, our simulations are agnostic to the value of $\frac{1}{N} \sum_{i=1}^N B_i$ and only depend on the differences $B_{i+1} - B_i = \Delta B = 10$ MHz [165]. Further, we bound $0 \leq J_i(t) \leq J_{\max} = 10$ MHz [166, 167], $|I_i(t)| \leq I_{\max}$, and $|Q_i(t)| \leq Q_{\max}$, where $I_{\max} = Q_{\max} = 4$ MHz, in accordance with state-of-the-art experimental data [79].

Our emulator tailors hardware pulses to implement a desired gate. Using a classical optimizer, we can compress these pulses until they reach the silicon hardware’s minimal evolution time (MET), that is, the smallest time within which the hardware can implement a target gate within a target fidelity [113]. To calculate the silicon METs, we split a pulse of duration T into M segments of equal duration $\Delta t = T/M$, which we then optimize. $J_i(t)$, $I_i(t)$, and $Q_i(t)$ are taken to be constant over each segment—*i.e.*, they are piecewise constant functions. We collect the m th segment’s pulse amplitudes [*i.e.*, Eq. (7)’s free parameters] into a vector $\vec{x}^{(m)}$, which makes up the m th column of our pulse-parameter matrix \mathbf{x} . That is, \mathbf{x} describes the Hamiltonian parameters throughout the duration of a pulse. For a given \mathbf{x} and set of drive frequencies $\vec{\omega}$, the Hamiltonian generates a time evolution $U(T)$ via the Schrödinger equation:

$$\frac{d}{dt}U(t) = -iH(t; \mathbf{x}, \vec{\omega})U(t), \quad (9)$$

where $U(0) = I$. We minimize T and optimize \mathbf{x} using the QuGrad [113, 168] implementation of GRAPE [169] with respect to a target operator infidelity. In our work, we set the MET to the shortest pulse duration which still achieves a physical-level infidelity of $\leq 0.1\%$.

To make pulse optimization computationally tractable at the magic-state-factory scale, we adopt a compartmentalized pulse-compression strategy. Each logical sub-circuit (*e.g.*, syndrome measurements and magic-state injections [40, 170]) is decomposed into segments acting on at most four physical qubits and each segment is pulse compressed. For a circuit decomposed as

$$\mathcal{C} = \mathcal{S}_1 \circ \mathcal{S}_2 \circ \dots \circ \mathcal{S}_K, \quad (10)$$

each sub-circuit \mathcal{S}_k is compiled into a locally optimized pulse with propagator $U_k = U(T_k^{MET}; \mathbf{x}^{(k)}, \vec{\omega}^{(k)})$, and concatenated in time to produce the logical circuit. This procedure allows us to quantify the cumulative error of concatenated compressed pulses.

B. Pulse optimization: results

Here, we summarize and interpret our memory experiments used to benchmark the effect of pulse compression and to characterize logical-memory error rates under different connectivity and coding choices. A memory experiment has three components. First, we prepare a logical

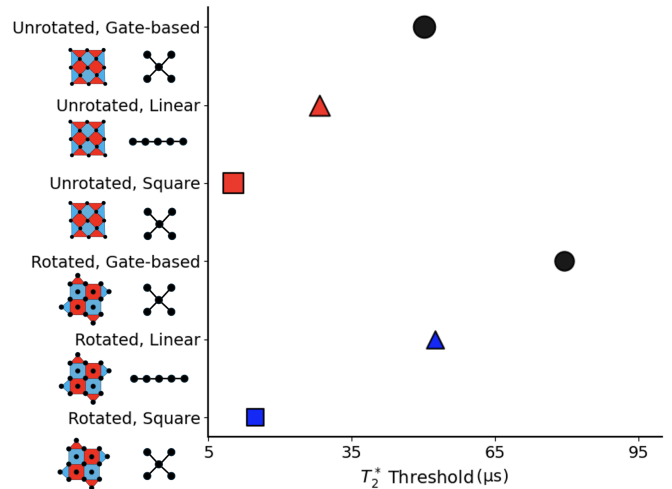


FIG. 10. **Coherence-time thresholds for Z memory experiments.** The minimum T_2^* coherence time (horizontal axis) for QEC protocols to improve the performance of an Z memory experiment with increased code distance. Various QEC schemes (vertical axis) are evaluated with or without pulse optimization. The rotated surface code is plotted in blue and the unrotated surface code in red. Linear connectivities are represented by triangles and square connectivities by squares. The black dots indicate the baseline (gate-based operation without pulse-optimization) values with square connectivity.

basis state. Second, we let the logical qubits idle for a chosen time window whilst syndrome checks are applied to the physical qubits. Third, we measure and decode the logical state. The observed logical infidelity is related to the underlying physical error processes through the specific decoding-and-syndrome-extraction schedules used in each configuration.

In this section, we limit our analysis to the standard surface code. Logical qubits are encoded in the joint (+1)-eigenvalued eigenspace of two sets of commuting stabilizers: Z- and X-type stabilizers, which can detect bit-flip and phase-flip errors, respectively. When implementing error correction throughout quantum computation, errors are detected by measuring both stabilizer types in syndrome extraction cycles. However, when benchmarking QEC codes or when quantifying error rates, one typically studies logical bit-flip and phase-flip errors individually. This can be done with a Z or X memory experiment. A Z memory experiment prepares a logical state $|0\rangle_L$ and measures how well it is preserved under repeated syndrome cycles, thereby quantifying logical X errors. An X memory experiment quantifies and detects Z errors.

To simplify the analysis, and to achieve tractable simulation times, we conduct our memory-experiment analysis with respect to local stochastic (Markovian) noise. Our noise model is specified in Sec. V A. We study two connectivity layouts (1D chain and square-grid nearest-

neighbor) and two surface-code geometries (rotated and unrotated). The main difference in the connectivity layouts comes from the fact that CNOT operations between non-neighboring physical qubits require SWAP chains in the linear architecture. In the square-grid architecture, which is utilized in the dense and patched architectures, there are next-neighbor interactions between all qubits in a local syndrome check. We compare the pulse optimized emulations with a gate-based baseline where the syndrome circuits are compiled into standard gates.

Figure 10 reports the threshold for Z-type memory experiments. To align our results with experimental parameters, we calculate our error thresholds in terms of the qubits' T_2^* decoherence times: if a silicon processor has longer T_2^* times than the threshold, then the logical error rate can be suppressed by increasing the code distance. We compare the rotated and unrotated surface codes. The unrotated surface code has a lower T_2^* threshold. This is because the unrotated surface code has fewer minimum-weight logical error paths (the smallest number of physical errors needed to form a chain stretching from one boundary of the code to the opposite boundary, flipping the logical qubit's state) [171]. However, the rotated surface code improves more with pulse optimization, yielding pulse-optimized T_2^* thresholds that are almost comparable. Moreover, the rotated surface code requires 25–30% fewer physical qubits to achieve the same logical error rate as the unrotated surface code at physical error rates less than 10^{-3} [171]. Despite the reduced qubit count of the rotated surface code, we proceed with the unrotated surface code for the rest of our analysis, because of the lower T_2^* threshold.

In addition to the memory experiments, we showcase the benefits of pulse optimization on logical states' coherence times throughout dephasing channels. In particular, we compare the infidelity ϵ of an idling single physical qubit ($|1\rangle$) with a logical qubit ($|1\rangle_L$) that undergoes pulse-optimized stabilizer cycles. The top panel of Fig. 11 shows the (log) infidelity as a function of the T_2^* time and the syndrome-check duration, which we have set to be larger than the MET. (The lower panel shows a contour version of the upper one.) The red and blue sheets represent the infidelities of the logical and physical qubits, respectively. The dotted black lines highlight the cross-over parameters after which the logical qubit has a lower infidelity than the physical one (i.e., the red sheet lies below the blue one). A clear trend emerges from the figure: when T_2^* increases or syndrome-check duration decreases, the performance of the logical qubit relative to the physical one improves. This observation highlights the benefits of pulse compression. MET-limited pulse optimization does not merely shorten gate sequences but can actively extend the effective logical coherence window by minimizing exposure to noise. The left and right plots show the linear and square connectivity, respectively. Clearly, compared to the linear connectivity, the

square one results in the logical qubits outperforming the physical qubits for a larger range of parameter values. This is because the syndrome checks in the linear connectivity rely on SWAP operations which introduce more noise.

V. NOISE MODELING

Most previous works on quantum-computational resource and overhead estimation, have utilized hardware agnostic and simplified noise models, for example, limiting the analysis to depolarizing noise. Here, we go beyond simple models. We tailor a silicon-specific noise model to align with real experiments. Our noise model builds on four components: (i) a Markovian error mechanism based on experimental relaxation and dephasing times; (ii) a non-Markovian mechanism obtained from a device-specific Hamiltonian and the filter-function formalism; (iii) a defect model appropriate for architectures with leakage and charge noise; and (iv) a model of the noise incurred when shuttling. Below, we specify each of these models.

A. Markovian error model

Most of the results presented in this work relies on a realistic silicon-tailored noise model. However, for computational tractability, we used a simplified Markovian noise model in Sec. IV B. In our simplified model, noise is characterized by the relaxation time T_1 and dephasing time T_2^* as in Refs. [172–175]. We used the following mapping to estimate the Pauli-error probabilities of single-qubit operations:

$$p_X = p_Y = \frac{1 - e^{-t/T_1}}{4}, \quad (11)$$

$$p_Z = \frac{1 - e^{-t/T_2^*}}{2} - \frac{1 - e^{-t/T_1}}{4}. \quad (12)$$

Intuitively, population relaxation contributes equally to bit-flip-type errors, while the additional dephasing component increases the effective Z-error probability. Two-qubit errors are modeled similarly, but with more convoluted formulae [172–174]. In the simulations of Sec. IV B, we applied these noise channels after each pulse operation [Eq. (10)] with the time t set by the pulse duration and T_1 and T_2^* as input parameters. We then used approximately fitted Pauli errors to estimate error-correction thresholds using STIM [176].

B. Non-Markovian error model

Here we present the main noise model of our work. The model is targeted towards the $1/f$ noise that domi-

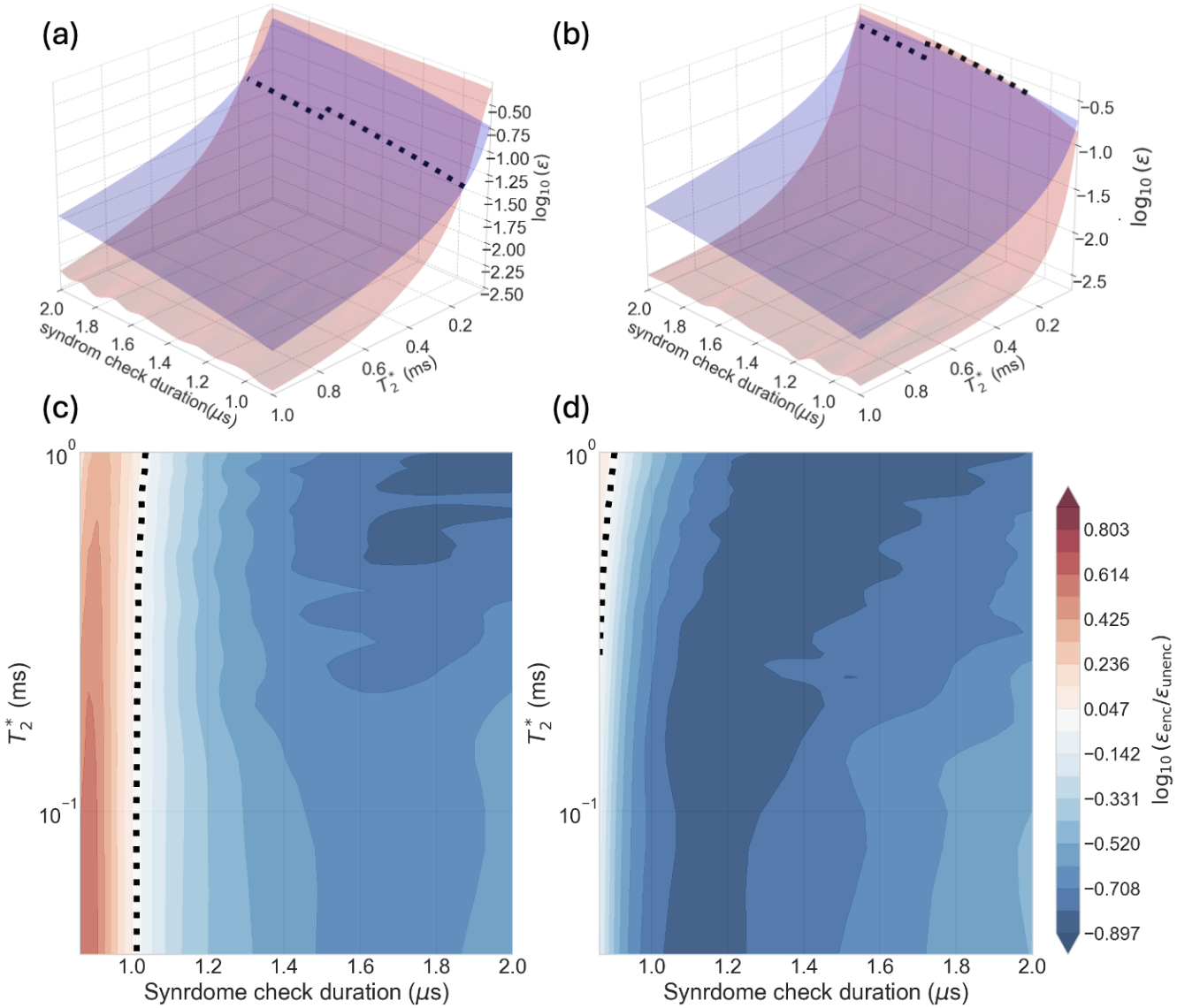


FIG. 11. **Logical vs physical memory performance.** The data presented in the left panels [(a) and (c)] was calculated using a linear connectivity, while the data presented in the right panels [(b) and (d)] was calculated using a square connectivity. In both (a) and (b), the semi-transparent blue sheet corresponds to the error on a physical state. The red sheet represents the error on the logical state encoded with a $d = 5$ code using 49 physical qubits. The black dotted line denotes the crossing point between parameter regions where the logical qubit outperforms the physical one. The bottom panels presents the same data in a contour plot. The region where the logical qubits have greater error probabilities than the physical ones are highlighted in blue. Conversely, in the red regions the logical qubits have smaller error probabilities than the physical ones. The black dotted line indicates the crossover regime.

nates spin-qubit systems [177–179]. This noise is caused by charge fluctuation in the semiconductor heterostructures and stray magnetic field gradients, spatial variations of the g -factor, or interface-induced spin-orbit interaction [180, 181]. When two-level charge systems stochastically switch between their levels, they produce a local electric-field fluctuation that shifts the quantum dot potential. The combination of such fluctuations, spanning timescales from nanoseconds to microseconds, gives rise to a noise spectrum dominated by slow components

and approximately proportional to $1/f$, where f denotes the transition frequency. To model temporally correlated noise, like the $1/f$ noise, we augment the Hamiltonian-level description (Sec. IV A) with the filter-function formalism [182]. Below, we summarize the methodology through a simple example. Detailed derivations are provided in App. I, where we rederive the relation between the infidelity, ϵ , and the noise spectrum:

$$\epsilon = \frac{1}{D+1} \sum_{\alpha} \int_{-\infty}^{\infty} \frac{d\omega}{2\pi} S_{\alpha}(\omega) F_{\alpha}(\omega). \quad (13)$$

Here, D is the dimensionality of the Hamiltonian of interest, $F_\alpha(\omega)$ is the filter function generated by the Hamiltonian, and $S_\alpha(\omega)$ is the noise spectral density function.

As a simple illustration of the filter-function treatment of noise, consider a single qubit driven by a control Hamiltonian $H_c = \frac{\Omega}{2}\sigma_x$ and subject to fluctuating dephasing noise $H_n = b(t)\sigma_z$. The noiseless ideal unitary evolution of the system is $U_c(t) = e^{-i(\Omega t/2)\sigma_x}$. However, H_n will corrupt this evolution. To see how, we first define the noise operators in the interaction picture as $\tilde{B}_\alpha(t) = U_c^\dagger(t)B_\alpha U_c(t)$ where B_α is related to H_n as shown in App. I. In our simple example, there is only one noise term generated by a Pauli-Z operator:

$$\tilde{B}_z(t) = e^{i(\Omega t/2)\sigma_x}\sigma_z e^{-i(\Omega t/2)\sigma_x} \quad (14)$$

$$= \cos(\Omega t)\sigma_z - \sin(\Omega t)\sigma_y. \quad (15)$$

We can then expand the noise operator within the interaction picture in the Pauli basis:

$$\tilde{H}_n(t) = b(t) \sum_k \tilde{B}_{z,k}(t)\sigma_k. \quad (16)$$

The coefficients are given by $\tilde{B}_{z,k}(t) = \frac{1}{2}\text{tr}[\tilde{B}_z(t)\sigma_k]$:

$$\tilde{B}_{z,\mathbb{1}}(t) = \frac{1}{2}\text{tr}[\tilde{B}_z(t)\mathbb{1}] = 0, \quad (17)$$

$$\tilde{B}_{z,x}(t) = \frac{1}{2}\text{tr}[\tilde{B}_z(t)\sigma_x] = 0, \quad (18)$$

$$\tilde{B}_{z,y}(t) = \frac{1}{2}\text{tr}[\tilde{B}_z(t)\sigma_y] = -\sin(\Omega t), \quad (19)$$

$$\tilde{B}_{z,z}(t) = \frac{1}{2}\text{tr}[\tilde{B}_z(t)\sigma_z] = \cos(\Omega t). \quad (20)$$

Next, we define the finite-time Fourier transforms $\tilde{B}_{z,k}(\omega) = \int_0^\tau dt \tilde{B}_{z,k}(t)e^{i\omega t}$ such that

$$\tilde{B}_{z,z}(\omega) = \int_0^\tau \cos(\Omega t)e^{i\omega t} dt \quad (21)$$

$$= \frac{1}{2} [I(\omega + \Omega, \tau) + I(\omega - \Omega, \tau)], \quad (22)$$

$$\tilde{B}_{z,y}(\omega) = -\int_0^\tau \sin(\Omega t)e^{i\omega t} dt \quad (23)$$

$$= \frac{i}{2} [I(\omega + \Omega, \tau) - I(\omega - \Omega, \tau)], \quad (24)$$

where $I(\omega \pm \Omega, \tau) = \int_0^\tau e^{i(\omega \pm \Omega)t} dt$. The filter function is given by the sum of the squares of the magnitudes of these coefficients:

$$F_z(\omega) = |\tilde{B}_{z,z}(\omega)|^2 + |\tilde{B}_{z,y}(\omega)|^2. \quad (25)$$

Evaluating Eq. (25), we find that

$$F_z(\omega) = \left| \frac{1}{2}(I_+ + I_-) \right|^2 + \left| \frac{i}{2}(I_+ - I_-) \right|^2 \quad (26)$$

$$= \frac{1}{2} (|I_+|^2 + |I_-|^2), \quad (27)$$

where $I_+ = I(\omega + \Omega, \tau)$ and $I_- = I(\omega - \Omega, \tau)$ and

$$|I(a, \tau)|^2 = \left| \frac{e^{ia\tau} - 1}{ia} \right|^2 = \frac{4 \sin^2\left(\frac{a\tau}{2}\right)}{a^2}. \quad (28)$$

Thus, the final expression for our simple example's filter function is

$$F(\omega) = \frac{\tau^2}{2} \left[\text{sinc}^2\left(\frac{(\omega + \Omega)\tau}{2}\right) + \text{sinc}^2\left(\frac{(\omega - \Omega)\tau}{2}\right) \right]. \quad (29)$$

In this particular example, we see, via Eq. (13), that the system is sensitive to noise around its Rabi frequency Ω : the filter function $F(\omega)$ is peaked around $\omega = \pm\Omega$. The actual device Hamiltonian of our system [Eq. (7)] is more complicated than that of this example. However, the calculation of the relevant filter function follows a similar derivation.

Next, we describe how we model the spectral density function $S_\alpha(\omega)$. Experimental observations of spin qubits show that the power spectrum of charge and magnetic noise follows a $1/f$ behavior in frequency, with some cut-offs [177–179]. We therefore construct a spectral density that satisfies the following requirements:

1. $1/f$ scaling over an intermediate frequency window.
2. Suppression of unphysical divergences at both low and high frequencies.

These considerations lead to the phenomenological equation

$$S(\omega) = \frac{A}{\max(|\omega|, \omega_{\text{low}}) \left[1 + \left(\frac{\omega}{\omega_{\text{high}}} \right)^2 \right]}. \quad (30)$$

Here, A sets the overall noise strength, ω_{low} is a low-frequency cutoff, and ω_{high} is a high-frequency cutoff. For example, when $|\omega| \ll \omega_{\text{low}}$, $S(\omega) \approx \frac{A}{\omega_{\text{low}}}$, corresponding to a white-noise plateau at low frequencies. Physically, $\omega_{\text{low}} \sim 1/T_{\text{max}}$ is set by the maximum experimental observation time T_{max} . In the intermediate regime $\omega_{\text{low}} \ll |\omega| \ll \omega_{\text{high}}$ we obtain the characteristic form $S(\omega) \approx \frac{A}{|\omega|}$.

Using the numerical pulse-evolution methods described in previous sections, we can construct estimates of operational infidelities in the following way.

1. We propagate a tomographically complete set of states $\{|g\rangle\}$ under the optimized control pulse to obtain the noiseless states $\{|\psi_g(t_i)\rangle\}$ at discrete time steps t_i . From these states, we can reconstruct the ideal unitary $U_c(t_i)$.
2. For each noise channel B_α (H_n in the previous example) labeled by α , we calculate the interaction-picture noise sensitivity $\tilde{B}_\alpha(t)$ at time t .

3. We perform finite-time Fourier transforms of $\tilde{B}_{\alpha k}(t)$ to obtain $\tilde{B}_{\alpha k}(\omega)$ and construct the filter functions $F_{\alpha}(\omega)$.
4. Using Eq. (13), we evaluate the spectral overlap between the filter function and the noise power spectral density $S_{\alpha}(\omega)$ to obtain the average gate infidelity ϵ .
5. We numerically fit a Pauli channel to the channel generated by the non-Markovian noise under the constraint that both channels yield the same infidelity (details in App. II).

In this way, we map the ideal pulse history onto a fully non-Markovian noise model and quantitatively predict the resulting operation (in)fidelties.

C. Defect error model

Spin-qubit architectures that rely on physical electron shuttling between operational zones will naturally suffer from localized fabrication defects [68, 183]. Such defects can include charge traps or interface impurities [78, 95, 184], which may render specific quantum dots temporarily unsuitable for qubit manipulation or transport. We model these defects as randomly blocked vertices on the device connectivity graph. Each node is independently defective with probability ϵ_{defect} .

We make the optimistic assumption that syndrome checks and efficient decoding can inform a quantum-computer user of the location of defects. Then, defect mitigation becomes a task of optimizing the shuttling routes such that defects are avoided. In our simulations, we compute the shortest viable shuttling path using breadth-first search [185] on the subgraph obtained by removing all defective vertices from the entire grid. The total shuttling time for a qubit transfer is given by $T_{\text{shuttle}} = t_{\text{step}} \cdot L_{\text{BFS}}$, where t_{step} is the time required to shuttle a qubit across a single edge (typically $t_{\text{step}} \sim 10$ ns for conveyor-mode shuttling over 100 nm), and L_{BFS} is the hop count of the shortest defect-free path. The Manhattan distance serves as a reference metric for the ideal, defect-free case.

Combined with gate and readout errors, the shuttling infidelity $\epsilon_{\text{shuttle}}$ contributes additively to the overall physical error budget. In Fig 12, we quantify how increased defect densities lead to longer shuttling detours (increasing L_{BFS}) and degrades the qubit fidelities.

D. Shuttling error model

Our simulations also account for errors induced by the motion of the electron-spin qubits during shuttling. Errors occur primarily as a result of field fluctuations and

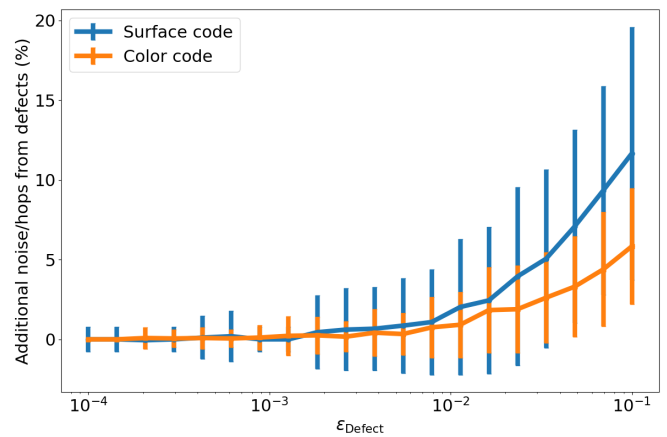


FIG. 12. **Noise impact of defects in shuttling-based architectures.** The additional amount of noise or number of hops is plotted as a function of the probability of defect errors ϵ_{defect} . The orange and blue lines denote data obtained from surface-code and color-code simulations, respectively. While fabrication defects typically increase shuttling distances by forcing routes around unavailable sites, the effective path length L_{BFS} can in principle be *shorter* than the ideal Manhattan distance: When the intended source or destination site is defective, the routing algorithm selects the nearest non-defective site. If both endpoints shift toward each other, the effective separation can decrease. Here, the simulation scale is restricted to a 20×20 lattice for illustrative purposes only.

the spin-orbit interaction at the point of acceleration and deceleration [186–188]. Experimental investigations quote shuttling errors on the order of 0.01% when shuttling over $10\mu\text{m}$. We inject the shuttling noise into our analysis simply as a source of error when qubits are shuttled.

VI. SPACE-TIME MODELING FOR MAGIC-STATE DISTILLATION

In this section, we outline our methodology for producing estimates of the space-time volume required to produce high-fidelity logical magic T states. We focus our study on ‘grow-and-distill’ MSD protocols [189]. First, we briefly summarize the distillation protocols. Second, we outline the logical components that contribute to errors. Third, we specify the mathematical model we use to convert per-operation logical error rates to end-to-end distillation-acceptance probabilities and output-fidelity estimates. Finally, we show how the per-round acceptance probabilities feed into an iterative, multi-round MSD process and outline how we calculate the total resources needed for MSD in terms of physical qubit count, runtime and space-time overhead.

The MSD protocols, shown in Fig. 13, typically consist of two stages: (i) injection of a noisy physical

magic state into a base quantum error-correcting code $[[N, k, d]]$ [170, 190] and (ii) logical distillation using a distillation code to suppress errors. This process is usually repeated iteratively, with each distillation round (ii) producing a single, high-fidelity logical magic state. Collectively, (i) and (ii) form what is known as an MSD factory. To further enhance efficiency, the logical code distance d can be increased after each iteration, enabling the factory to suppress noise further and produce a higher-quality output with reduced overhead in subsequent rounds.

The distillation framework considered here is slightly different from protocols where one directly expands the code distance by a large interval [39]. Practically, we can improve resource efficiency by gradually increasing the code distance. Recent work has proposed several techniques that could substantially reduce the overhead of MSD, including magic-state cultivation protocols [154] and improved encoding schemes [191, 192]. While these approaches show promising reductions in resource requirements, many are still under active development and lack comprehensive resource analyses across realistic hardware architectures. Therefore, in this work, we focus on the conventional MSD pipelines described above, which provide a well-established baseline for evaluating architectural tradeoffs.

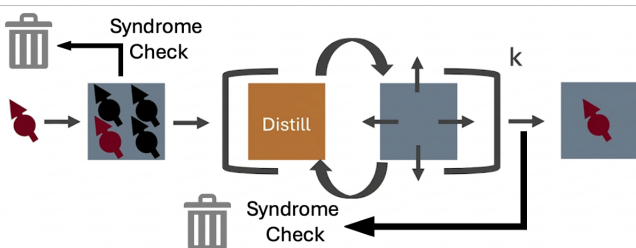


FIG. 13. **Magic-state-distillation protocol.** First, physical spin qubits (red) prepared in noisy magic states are injected into an underlying QEC code. This produces a low-fidelity logical magic state (first square patch, from the left). A distillation code (second square patch, from the left) is utilized to carry out syndrome checks of the logical magic states. If the syndrome checks fail, the MSD round is discarded. If the syndrome checks are successful, the QEC code distance is expanded (third square patch, from the left). The distillation process is repeated k times, after which a high-fidelity logical magic state (fourth square patch, from the left) is output.

A. MSD protocols

We first introduce the popular 15→1 MSD protocol. It is based on Haah–Hastings construction [193] and uses the transversality of T gates on the quantum Reed–Muller code [194]. Concretely: if we prepare some stabilizer states with $n = 16$ logical qubits, then we can inject 15 logical T states via teleportation and output

one higher-fidelity T state. Under ideal conditions, and for an input infidelity of q , the Reed–Muller code yields an output infidelity $q_{\text{out}} \propto q^3$. Noisy Clifford operations (preparation, idle and CNOT) result in actual implementations suffering from additional rejections and failure contributions. These issues are accounted for by the effective logical-operation error model described below.

A compact alternative to the 15→1 MSD protocol is the 5→1 protocol [132]. The 5→1 protocol uses a small, “perfect” $[[5, 1, 3]]$ code for both the encoding and decoding. A Clifford circuit maps five noisy input T states to one higher-fidelity T state. The leading-order power-law suppression of input- T errors under ideal conditions is given by $q_{\text{out}} \propto q^2$. In this work, we briefly compare the 5→1 protocol to the 15→1 protocol. However, the main parts of our analysis focuses on the 15→1 circuit for which we have numerically simulated the explicit mappings from the physical error rates to the logical ones.

To quantify the errors incurred during an MSD protocol, one must study its individual logical components. These logical components are implemented with an underlying QEC code using repeated QEC cycles or rounds. Each of these logical components have failure and rejection probabilities that depend on the physical-level noise strength p and on the code distance d used to protect the logical patch. The dominant sources of logical errors in MSD protocols are:

- *Logical state preparation* ($|\bar{0}\rangle, |\bar{+}\rangle$) fails with probability $\bar{p}_{\text{prep}}(p, d)$.
- *Logical idle* (one QEC cycle of idling) fails with probability $\bar{p}_{\text{idle}}(p, d)$.
- *Logical CNOT operations* fails with probability $\bar{p}_{\text{CNOT}}(p, d)$.
- *Initialization of low-fidelity T states* fails with failure probability $p_{\text{fail}}^T(q, p, d)$ and are rejected with probability $p_{\text{rej}}^T(q, p, d)$.

Given these per-operation failure probabilities, we model the performance of a logical MSD circuit as follows. Let $p_{\text{rej}}^{\text{dist}}(q, p, d)$ and $p_{\text{fail}}^{\text{dist}}(q, p, d)$ denote the rejection and failure probabilities of a single round of the logical distillation circuit (*i.e.*, the probability that the protocol aborts because syndrome checks indicate an error, and the probability that it accepts a faulty output, respectively). These probabilities can be approximated, to leading order, in terms of the aforementioned logical errors [189, 195]. We extract the linear coefficients using the following approach: (i) set all sources of logical errors except the one under test to zero, (ii) run Monte Carlo trials of the complete logical operation or distillation circuit, (iii) measure the fraction of trials leading to rejection or failure, and (iv) fit the measured rejection or failure probability to a linear function of the logical error

parameter under test. Repeating this for each source of logical error and combining the results yields

$$p_{\text{rej}}^{\text{dist}}(q, p, d) = p_{\text{rej}}^T(q, d) + 12.3\bar{p}_{\text{prep}} + (466 + 4.13d)\bar{p}_{\text{idle}} + 51.7\bar{p}_{\text{CNOT}}, \quad (31)$$

$$p_{\text{fail}}^{\text{dist}}(q, p, d) = p_{\text{fail}}^T(q, d) + 16.9\bar{p}_{\text{idle}} + 1.93\bar{p}_{\text{CNOT}}. \quad (32)$$

To produce our resource estimates for MSD, we must gauge the effect of Eqs. (31) and (32) on the MSD protocols. We use STIM to simulate the iterative MSD processes. (As STIM is a stabilizer simulator, we follow standard practice [154, 196] and simulate the distillation of $S|+\rangle$ states rather than T states.) The output infidelity is obtained by iterating the map

$$q^{(i)} = p_{\text{fail}}^{\text{dist}}(q^{(i-1)}, p, d^{(i)}), \quad q^{(0)} = p_{\text{fail}}^{\text{init}}(p), \quad (33)$$

until the desired target infidelity $q^{(k)} \leq p_{\text{target}}$ is reached on the k th iteration [197]. The expected number of *physical* qubits required by a k -round protocol is then

$$N_{\text{phy}} = \max_{i=1, \dots, k} \left[\alpha^{(i)} N(d^{(i)}) \prod_{j=i}^k \frac{R^{(j)}}{r^{(j)}} \right]. \quad (34)$$

Here,

$$r^{(i)} = 1 - p_{\text{rej}}^{\text{dist}}(q^{(i-1)}, p, d^{(i)}), \quad (35)$$

denotes the i th round's acceptance probability. $R^{(i)}$ denotes the number of input logical T states required in the i th round ($R^{(i)} = 15$ for the $15 \rightarrow 1$ protocol). $\alpha^{(i)}$ denotes the number of logical qubits consumed per input magic state ($\alpha^{(0)} = 15$ and $\alpha^{(i>0)} = (16 + 15)/15$ for the $15 \rightarrow 1$ protocol). Finally, $N(d)$ denotes the number of *physical* qubits required to implement a single distance- d logical qubit.

The protocol runtime is

$$\tau = \tau_{\text{init}} + \sum_{i=1}^k \tau_{\text{dist}}(d^{(i)}). \quad (36)$$

Here, τ_{init} is the initialization time and $\tau_{\text{dist}}(d)$ the time to execute a single logical distillation iteration at distance d . The total space-time overhead is the product $N_{\text{phy}} \times \tau$.

B. MSD in silicon devices

We now summarize our analysis of MSD protocols operated on silicon hardware. We start by investigating the effect of coherence and gate times as well as initialization and measurement errors on the resource overheads in the dense architecture. The patched and sparse architectures follow similar qualitative trends (App. III). Our results for the $15 \rightarrow 1$ protocol with lattice surgery and with transversal gates are presented in Figs 14. The left column displays the results from simulations of MSD with

the surface code and lattice-surgery operations; the right column presents analogous results from simulations with the color code and transversal operations. In the first two rows, we quantitatively demonstrate that faster measurements, initializations, and single- and two-qubit Clifford operation times reduces the space-time resources for MSD. Similarly, the last row shows that the space-time resources decrease with improved T_2^* times. For example, a T_2^* increase of an order of magnitude generates a space-time-volume decrease by about a factor of 2 to 3. The noise bias in silicon ($T_2^* \ll T_1$) means that the resource improvements with increased T_1 times are less prominent.

We also compared the $5 \rightarrow 1$ and $15 \rightarrow 1$ protocols operating with either surface or color codes, and either lattice surgery or transversal gates. In Fig. 15, we present the sparse architecture's space-time overhead and qubit footprint as a function of T -state target infidelity. Naturally, the overheads increase with decreased target infidelities. We observe that the $5 \rightarrow 1$ protocol has a higher resource cost compared to the $15 \rightarrow 1$ protocol. Among all configuration we analyzed, we find that the $15 \rightarrow 1$ protocol implemented with the surface code and transversal operation achieves the lowest space-time overheads. The lowest qubit footprint is achieved by the $15 \rightarrow 1$ protocol implemented with the color code and transversal operations. The $5 \rightarrow 1$ curve experience a large resource overhead divergence at a target infidelity of around 10^{-18} . Similarly, we observe a large increase in the overheads of the $15 \rightarrow 1$ protocol at target infidelities below 10^{-22} . These observation can be explained by the competition of resources for the lowering of T state infidelities and the increase of Clifford-operation fidelities. Initially, one can suppress both errors by increasing the QEC code distance, which generates the step-wise increase. However, for higher fidelities, it is cheaper, in terms of resources, to reduce the errors on the logical Clifford operations. Then, the input T -state infidelity becomes the bottleneck for the target distillation infidelity. Consequently, in addition to increasing the code distance, one must apply extra rounds of distillation. Due to the efficiency in suppressing the errors with $15 \rightarrow 1$ distillation protocol, the jump is not seen for the range of infidelity plotted. However, for the $5 \rightarrow 1$ protocol with only quadratic suppression in the infidelity, the jump is resources happens at infidelities around 10^{-18} .

Finally, we demonstrate how pulse compression (Sec. IV A) can reduce the MSD overhead in the dense architecture. Our findings are summarized in Tab. II. The top block displays data from simulations of MSD implemented with standardized gates. The parameters are taken from Tab. I. The different settings for the fault-tolerant implementation naturally leads to different requirements on the number of physical qubits and the wall-clock time needed for an MSD procedure. The bottom block of the table presents the same analysis but

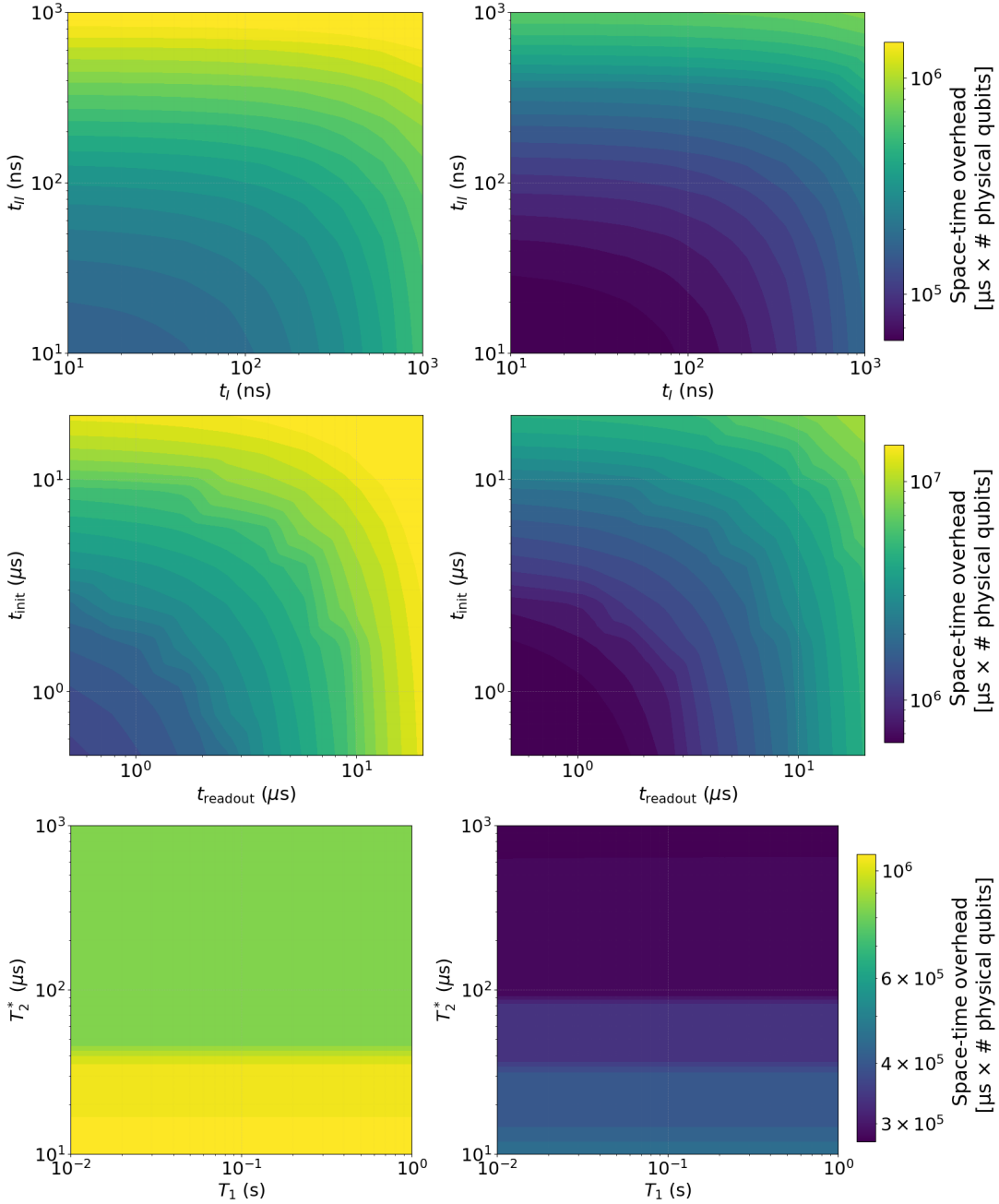


FIG. 14. **Space-time overhead for the production of one magic state.** The color bar indicates the space-time overhead (number of physical qubits times the wall-clock time in units of μs) as a function of gate times (top panel), readout and initialization times (middle panel), and coherence times (bottom panel) for the dense architecture. The left and right plots show data for the surface code with lattice-surgery operations and the color code with transversal operations, respectively. The logical magic state was produced using the $15 \rightarrow 1$ MSD protocol with a target infidelity of 10^{-12} .

with data from emulations with compressed and optimized hardware pulses. (The pulses were compressed in time to reach their MET at a cutoff infidelity of 10^{-4} .) Clearly, pulse compression reduces the physical footprint and shortens the wall-clock time for T -state generation. The fastest to perform distillation is achieved with the surface code and transversal operations. The

color code counterpart has less stringent requirements on the physical-qubit count.

C. Resource Estimation modeling

Finally, we outline the analysis used to produce the estimation of the resources used to implement archetypal

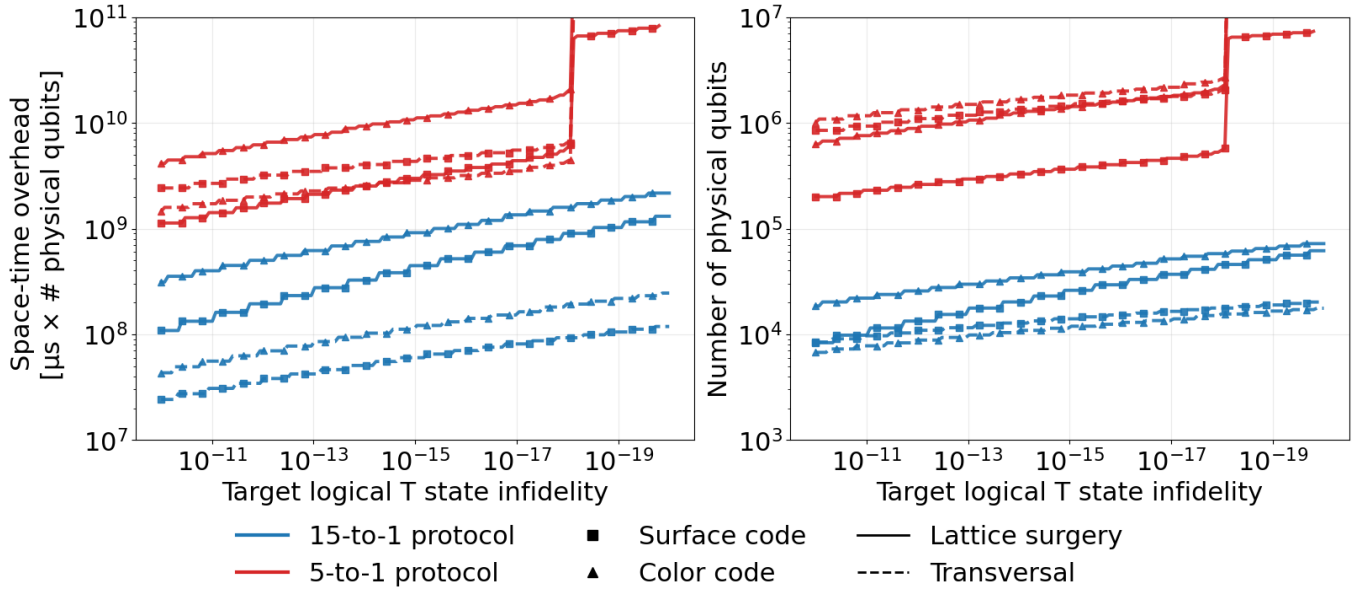


FIG. 15. **Resources vs. logical magic-state infidelity.** The space-time overhead (number of qubits times wall-clock time in μs) is plotted as a function of magic-state infidelity. The data is obtained for the sparse architecture. The noise model from Sec. VB is chosen in accordance with Table I. Eight different setups are plotted: the $5 \rightarrow 1$ and $15 \rightarrow 1$ distillation protocols are plotted in red and blue, respectively; transversal operations and lattice-surgery operations are plotted with dotted and solid lines, respectively; and the surface code and color code are highlighted with triangular and circular markers, respectively. The space-time overhead is plotted on the left plot’s vertical axis; the number of physical qubits is plotted on the right plot’s vertical axis. The target magic-state infidelity is plotted on the horizontal axis.

Gate-based operation							
surface				color			
surgery		transversal		surgery		transversal	
15-1	5-1	15-1	5-1	15-1	5-1	15-1	5-1
8 k (422 μs)	200 k (182 μs)	7 k (82 μs)	850 k (92 μs)	20 k (567 μs)	630 k (212 μs)	6 k (208 μs)	1086 k (473 μs)
Pulse-based operation (MET)							
surface				color			
surgery		transversal		surgery		transversal	
15-1	5-1	15-1	5-1	15-1	5-1	15-1	5-1
6 k (380 μs)	131 k (140 μs)	5 k (67 μs)	687 k (90 μs)	12 k (450 μs)	426 k (190 μs)	5 k (171 μs)	767 k (458 μs)

TABLE II. **Summary of MSD factory resources.** Number of qubits (and time) needed to generate one magic state with infidelity below 10^{-12} . The number of physical qubits and wall-clock time needed to distill one magic T state is given for eight logical configurations (left to right) and for gate-based and pulse-optimized implementations (top and bottom).

quantum algorithms on silicon hardware. Our results are summarized in Fig. 2. In large, we follow the strategies and conventions outlined in Ref. [13], but from a silicon-specific perspective. The data in Fig. 2 is calculated with respect to the standard surface code for dense and sparse architectures and the XZZX surface code for the sparse architecture.

Resource estimation for large-scale fault-tolerant quantum algorithms is commonly performed by reducing all operations to the Cliffords + T gate set. Under QEC, Clifford gates are cheap and T gates are expensive, requiring costly MSD. Our workflow begins by expressing

a target algorithm as modular subroutines and compiling these subroutines into a circuit model built from Toffoli gates, Clifford gates, and single-qubit rotations. Depending on the algorithm, we consider either the native T -gate count or the Toffoli count. Then, we convert all Toffoli gates via a standard fault-tolerant construction that uses a small number of T gates and Clifford gates [13, 44]. Next, we approximate the single-qubit rotations by short sequences of Clifford gates and T gates chosen to meet a target precision [198]. This conversion is efficient: the required circuit length of an approximation grows logarithmically with the desired accuracy. Thus, we calcu-

late the total number of T gates needed for the target algorithm by simply summing the contribution from the Toffoli gates and the single-qubit-gate approximations. Finally, we calculate the spatial and temporal resource cost of implementing the T gates needed for the target algorithm. We do so by simulating the performance of the MSD factories described in Secs. VI A and VI B.

We adopt the standard $15 \rightarrow 1$ distillation protocol, as we found it to outperform the $5 \rightarrow 1$ protocol at comparable target errors for larger quantum algorithms. We study three quantum algorithms. Together, they cover the different scientific and commercial areas where quantum computers are expected to be useful: quantum-dynamics simulation [199, 200], quantum chemistry [6, 49], and integer factoring [1, 2]. The three applications showcase different algorithmic structures and resource bottlenecks, highlighting complementary challenges for large-scale fault-tolerant quantum computation. Next, we give brief summaries of these algorithms.

The first benchmark algorithm simulates the quantum dynamics of a two-dimensional transverse-field Ising model with 100 spins. This task is one of the smallest scientifically meaningful problems believed to be intractable for classical computers [199]. The Ising Hamiltonian is

$$H = -J \sum_{\langle j,k \rangle} Z_j Z_k + g \sum_j X_j, \quad (37)$$

where $\langle j, k \rangle$ denotes nearest-neighbor pairs on a $\sqrt{N} \times \sqrt{N}$ lattice with $N = 100$, J is the coupling strength, and g is the transverse field. Time evolution for 20 steps is implemented, with an overall error capped at 0.1%, using a fourth-order Trotter-Suzuki product formula [200].

The second benchmark algorithm computes the activation energy level of the ZnS compound [49]. The calculation uses quantum phase estimation combined with the double-factorized qubitization algorithm [201, 202]. The algorithm constructs an exact block-encoding of the electronic structure Hamiltonian H and then uses qubitization [201] to form a quantum walk operator $W(H) = e^{i \arccos(H/\lambda)}$, whose eigenphases encode the eigenvalues of the Hamiltonian. And λ here is defined as the norm of the system Hamiltonian. Since this operator can be implemented exactly, applying quantum phase estimation to $W(H)$ recovers the spectrum with optimal query complexity. To design circuits whose T-gate cost for implementing $W(H)$ scales well, the Hamiltonian is decomposed into a linear combination of unitaries with efficiently implementable SELECT and PREPARE oracles [203]. When combined with phase estimation, this yields a simulation algorithm whose overall T-gate complexity scales linearly in system size and inverse precision.

The third benchmark algorithm applies Shor's period finding [1, 2, 56, 204] to factor a 2048-bit RSA task. This benchmark serves as a canonical benchmark

for fault-tolerant quantum architectures, directly related to the long-term security of widely deployed public-key cryptography systems. Our analysis relied on the logical construction from [2]. More advanced recent techniques [204–207] may lead to an overhead reduction by two orders of magnitude.

We work under the assumption that the algorithms are implemented on quantum hardware on which the MSD factories produce T states at a sufficiently fast rate to not limit the algorithms' clock-speeds. With respect to a specific target algorithm, let N_q^{phy} denote the number of physical qubits, and N_t the number of logical time cycles needed to generate all the T states required by the algorithm. Naturally, one can reduce the runtime of an algorithm by parallelization. However, this will come at the cost of more physical qubits. On the other hand, one can reduce the spatial footprint by sequentially injecting the minimal number of magic states needed at any one time. In such a scenario, the temporal cost is high. The space-time tradeoff is selected from a set of candidates as follows.

We illustrate our methodology with a calculation. If the total number of physical qubits is $N_q^{\text{phy}} = N_T^{\text{phys}} m$, then we can produce m magic states with N_{cycle} cycles. Suppose the algorithm requires M magic T states; we can produce all M in a $\lceil N_{\text{cycle}} M / m \rceil$ logical cycles with $N_T^{\text{phys}} m$ physical qubits. If our algorithm takes N_t logical cycles, then we need $N_t \geq \lceil N_{\text{cycle}} M / m \rceil$ to ensure that the T state production keeps up with the algorithm's T -state demands. We can minimize the number of physical qubits $N_T^{\text{phys}} m$ by imposing the equality: $N_t = \lceil N_{\text{cycle}} M / m \rceil = \lceil N_{\text{cycle}} N_T^{\text{phys}} M / N_q \rceil$. Finally, by slowing down the execution of our algorithm (increasing N_t) we can reduce the number of physical qubits required for magic state distillation. In our resource-estimation routine, we calculate the total space-time volume needed to execute the target algorithms. We also study how the spatial footprint and algorithmic runtime changes as a function of the fraction of the quantum hardware that is allocated to the MSD factories.

VII. DISCUSSION

Our resource analysis provides a hardware-aware evaluation of magic-state distillation for silicon spin-qubit architectures, bridging theoretical QEC and practical device constraints. By modeling three distinct connectivity regimes (sparse SpinBus, patched, and dense nearest-neighbor architectures) we have quantified the tradeoffs between connectivity, shuttling overheads, and space-time volume for high-fidelity production of logical T states. Several insights emerge.

First, connectivity is a dominant factor in distillation efficiency. Dense layouts consistently outperform sparse and patched architectures in space-time volume, primar-

ily by eliminating shuttling latency and minimizing idle errors. However, the dense regime remains aspirational due to unresolved wiring challenges. The patched architecture offers a pragmatic compromise, achieving overhead reduction by localizing error correction within dense patches while using shuttling only for inter-patch communication. This suggests that near-term experimental efforts should focus on developing modular, patch-based designs that balance connectivity with fabrication feasibility. Second, pulse-level optimization substantively enhances logical coherence and reduces resource overhead. Our memory experiments demonstrate that pulse compression can extend logical coherence further beyond that of the underlying physical qubits. Integrating hardware-native pulse optimization into syndrome extraction and distillation circuits should therefore be a priority for experimental implementations aiming to minimize space-time costs. Third, code and operation choices interact strongly with architecture. While surface codes with lattice surgery are widely adopted for their local connectivity, we find that both the surface code and the color code with transversal operations can achieve lower space-time overhead in dense regimes. This advantage becomes less obvious in sparse layouts where shuttling latency dominates. Thus, the optimal code choice is not universal, but depends on the underlying hardware connectivity and control capabilities. In addition, biased XZZX-surface code could lead to further resource reduction as it inherently fits the silicon spin-qubit platform where dephasing errors dominate. Finally, our hardware-tailored resource analysis—mapping target logical infidelities back to required physical parameters—provides actionable guidance for experimentalists. For example, in a dense surface-code layout with a target logical T -state infidelity of 10^{-12} , an order-of-magnitude improvement in gate speed or in T_2^* coherence time would reduce the space-time overhead by factors of approximately 6 and 2, respectively. These benchmarks help prioritize improvements in fabrication, control, and materials. A major bottleneck for the Sparse and Patched architectures is the shuttling fidelity. Our pipeline clarified the inability to implement basic QEC codes unless the current best-case shuttling fidelities are improved by an order of magnitude. A more detailed analysis would benefit the experimental development of improved shuttling channels. Such an analysis, which we leave for future work, should include the treatment of dynamic decoherence during shuttling [208], spin-orbit effects and valley excitations.

This work opens several avenues for future research. For example, our work could be extended to quantify the resource improvement available via MSD without measurements [209]. Integrating recent advances in qLDPC codes [210], constant-overhead magic-state injection, and distributed quantum computing architectures may also provide new pathways to reduce both qubit counts and

runtimes. Moreover, as indicated by our XZZX analysis, the design of bias- and hardware-tailored QEC codes could further lower the resource overheads. Future works should also aim to tailor the decoders to the silicon hardware’s correlated noise profile. Such results may also lower overheads by enabling, *e.g.*, single-shot QEC [211, 212]. More broadly, the resource-estimation pipeline developed in this work provides a general framework for systematically quantifying the impact of these future advances. As improved codes, decoders, state-injection protocols, and hardware architectures emerge, they can be incorporated into our workflow to evaluate their effects on logical error rates, qubit requirements, and execution times under realistic noise assumptions. In this sense, our framework is not limited to the present study, but can serve as a reusable benchmark platform for guiding future fault-tolerant quantum computing design.

-
- [1] P. W. Shor, Algorithms for quantum computation: discrete logarithms and factoring, in *Proceedings of the 35th Annual Symposium on Foundations of Computer Science* (1994) pp. 124–134.
 - [2] C. Gidney and M. Ekerå, How to factor 2048 bit rsa integers in 8 hours using 20 million noisy qubits, *Quantum* **5**, 433 (2021).
 - [3] S. Lloyd, Universal quantum simulators, *Science* **273**, 1073 (1996).
 - [4] A. M. Childs, D. Maslov, Y. Nam, N. J. Ross, and Y. Su, Toward the first quantum simulation with quantum speedup, *Proceedings of the National Academy of Sciences* **115**, 9456 (2018).
 - [5] D. W. Berry, G. Ahokas, R. Cleve, and B. C. Sanders, Efficient quantum algorithms for simulating sparse hamiltonians, *Communications in Mathematical Physics* **270**, 359 (2007).
 - [6] R. Babbush, C. Gidney, D. W. Berry, N. Wiebe, J. McClean, A. Paler, A. Fowler, and H. Neven, Encoding electronic spectra in quantum circuits with linear t complexity, *Physical Review X* **8**, 041015 (2018).
 - [7] Y. Dong, L. Lin, and Y. Tong, Ground-state preparation and energy estimation on early fault-tolerant quantum computers via quantum eigenvalue transformation of unitary matrices, *PRX quantum* **3**, 040305 (2022).
 - [8] S. Lee, J. Lee, H. Zhai, Y. Tong, A. M. Dalzell, A. Kumar, P. Helms, J. Gray, Z.-H. Cui, W. Liu, *et al.*, Evaluating the evidence for exponential quantum advantage in ground-state quantum chemistry, *Nature communications* **14**, 1952 (2023).
 - [9] A. Gilyén, S. Arunachalam, and N. Wiebe, Optimizing quantum optimization algorithms via faster quantum gradient computation, in *Proceedings of the Thirtieth Annual ACM-SIAM Symposium on Discrete Algorithms* (SIAM, 2019) pp. 1425–1444.
 - [10] E. Farhi, J. Goldstone, and S. Gutmann, A quantum approximate optimization algorithm, *arXiv preprint arXiv:1411.4028* (2014).
 - [11] H. Zhou, M. Cain, and M. D. Lukin, Opportunities in full-stack design of low-overhead fault-tolerant quantum

- computation, *Nature Computational Science* **5**, 1110 (2025).
- [12] M. Gutiérrez, M. Müller, and A. Bermúdez, Transversality and lattice surgery: Exploring realistic routes toward coupled logical qubits with trapped-ion quantum processors, *Physical Review A* **99**, 022330 (2019).
- [13] M. E. Beverland, P. Murali, M. Troyer, K. M. Svore, T. Hoefler, V. Kliuchnikov, G. H. Low, M. Soeken, A. Sundaram, and A. Vashillo, Assessing requirements to scale to practical quantum advantage, arXiv preprint arXiv:2211.07629 (2022).
- [14] E. Fontana, N. Fitzpatrick, D. M. n. Ramo, R. Duncan, and I. Rungger, Evaluating the noise resilience of variational quantum algorithms, *Phys. Rev. A* **104**, 022403 (2021).
- [15] D. Stilck França and R. García-Patrón, Limitations of optimization algorithms on noisy quantum devices, *Nature Physics* **17**, 1221 (2021).
- [16] G. De Palma, M. Marvian, C. Rouzé, and D. S. França, Limitations of variational quantum algorithms: A quantum optimal transport approach, *PRX Quantum* **4**, 010309 (2023).
- [17] K. Dalton, C. K. Long, Y. S. Yordanov, C. G. Smith, C. H. W. Barnes, N. Mertig, and D. R. M. Arvidsson-Shukur, Quantifying the effect of gate errors on variational quantum eigensolvers for quantum chemistry, *npj Quantum Information* **10**, 18 (2024).
- [18] J. Preskill, Quantum computing in the nisq era and beyond, *Quantum* **2**, 79 (2018).
- [19] A. Bouland, B. Fefferman, C. Nirkhe, and U. Vazirani, On the complexity and verification of quantum random circuit sampling, *Nature Physics* **15**, 159 (2019).
- [20] J. R. McClean, S. Boixo, V. N. Smelyanskiy, R. Babbush, and H. Neven, Barren plateaus in quantum neural network training landscapes, *Nature communications* **9**, 4812 (2018).
- [21] A. M. Steane, Error correcting codes in quantum theory, *Physical Review Letters* **77**, 793 (1996).
- [22] E. T. Campbell, B. M. Terhal, and C. Vuillot, Roads towards fault-tolerant universal quantum computation, *Nature* **549**, 172 (2017).
- [23] E. Knill, R. Laflamme, and W. H. Zurek, Resilient quantum computation, *Science* **279**, 342 (1998).
- [24] D. Gottesman, An introduction to quantum error correction and fault-tolerant quantum computation, in *Quantum information science and its contributions to mathematics, Proceedings of Symposia in Applied Mathematics*, Vol. 68 (2010) pp. 13–58.
- [25] B. M. Terhal, Quantum error correction for quantum memories, *Reviews of Modern Physics* **87**, 307 (2015).
- [26] A. G. Fowler, M. Mariantoni, J. M. Martinis, and A. N. Cleland, Surface codes: Towards practical large-scale quantum computation, *Physical Review A* **86**, 032324 (2012).
- [27] A. Bermudez, X. Xu, R. Nigmatullin, J. O’Gorman, V. Negnevitsky, P. Schindler, T. Monz, U. G. Poschinger, C. Hempel, J. Home, *et al.*, Assessing the progress of trapped-ion processors towards fault-tolerant quantum computation, *Physical Review X* **7**, 041061 (2017).
- [28] Suppressing quantum errors by scaling a surface code logical qubit, *Nature* **614**, 676 (2023).
- [29] Quantum error correction below the surface code threshold, *Nature* **638**, 920 (2025).
- [30] F. Tripier, W. C. Chung, J. Young, S. Alam, B. Bjork, A. Brodutch, F. L. Buessen, N. J. Coble, T. Dellaert, D. Maslov, *et al.*, Fault-tolerant quantum computing with trapped ions: The walking cat architecture, arXiv preprint arXiv:2604.19481 (2026).
- [31] S. Aaronson and D. Gottesman, Improved simulation of stabilizer circuits, *Physical Review A—Atomic, Molecular, and Optical Physics* **70**, 052328 (2004).
- [32] B. W. Reichardt, Improved magic states distillation for quantum universality, arXiv preprint quant-ph/0411036 (2004).
- [33] S. Bravyi and A. Kitaev, Universal quantum computation with ideal clifford gates and noisy ancillas, *Physical Review A—Atomic, Molecular, and Optical Physics* **71**, 022316 (2005).
- [34] B. W. Reichardt, Quantum universality from magic states distillation applied to css codes, *Quantum Information Processing* **4**, 251 (2005).
- [35] B. W. Reichardt, Quantum universality by state distillation, arXiv preprint quant-ph/0608085 (2006).
- [36] A. M. Meier, B. Eastin, and E. Knill, Magic-state distillation with the four-qubit code, arXiv preprint arXiv:1204.4221 (2012).
- [37] C. Jones, Multilevel distillation of magic states for quantum computing, arXiv preprint arXiv:1210.3388 (2012).
- [38] S. Bravyi and J. Haah, Magic-state distillation with low overhead, *Physical Review A—Atomic, Molecular, and Optical Physics* **86**, 052329 (2012).
- [39] D. Litinski, Magic state distillation: Not as costly as you think, *Quantum* **3**, 205 (2019).
- [40] Y. Li, A magic state’s fidelity can be superior to the operations that created it, *New Journal of Physics* **17**, 023037 (2015).
- [41] L. Daguerre, R. Blume-Kohout, N. C. Brown, D. Hayes, and I. H. Kim, Experimental demonstration of high-fidelity logical magic states from code switching, *Physical Review X* **15**, 041008 (2025).
- [42] P. Sales Rodriguez, J. M. Robinson, P. N. Jepsen, Z. He, C. Duckering, C. Zhao, K.-H. Wu, J. Campo, K. Bagnall, M. Kwon, *et al.*, Experimental demonstration of logical magic state distillation, *Nature* **645**, 620 (2025).
- [43] BenchQ, <https://github.com/zapatacomputing/benchq>, accessed: 2026-03-03.
- [44] M. P. Harrigan, T. Khattar, C. Yuan, A. Peduri, N. Yosri, F. D. Malone, R. Babbush, and N. C. Rubin, Expressing and analyzing quantum algorithms with qualtran (2024), arXiv:2409.04643 [quant-ph].
- [45] W. van Dam, M. Mykhailova, and M. Soeken, Using azure quantum resource estimator for assessing performance of fault tolerant quantum computation, in *Proceedings of the SC’23 Workshops of the International Conference on High Performance Computing, Network, Storage, and Analysis* (2023) pp. 1414–1419.
- [46] D. Litinski, A game of surface codes: Large-scale quantum computing with lattice surgery, *Quantum* **3**, 128 (2019).
- [47] M. Mohseni, A. Scherer, K. G. Johnson, O. Wertheim, M. Otten, N. A. Aadit, Y. Alexeev, K. M. Bresniker, K. Y. Camsari, B. Chapman, *et al.*, How to build a quantum supercomputer: Scaling from hundreds to millions of qubits, arXiv preprint arXiv:2411.10406 (2024).
- [48] D. Litinski, How to compute a 256-bit elliptic curve private key with only 50 million toffoli gates, arXiv preprint arXiv:2306.08585 (2023).

- [49] D. Filippov, P. Yang, and P. Murali, Architecting distributed quantum computers: Design insights from resource estimation, arXiv preprint arXiv:2508.19160 (2025).
- [50] C. Campbell, R. Rines, V. Omole, T. Oberoi, P. Goiporia, R. Roy, R. P. Cline, E. B. Jones, and T. Tomesh, Resource estimation via efficient compilation of key quantum primitives, arXiv preprint arXiv:2604.01376 (2026).
- [51] S. Sunami, A. Goban, and H. Yamasaki, Transversal surface-code game powered by neutral atoms, arXiv preprint arXiv:2506.18979 (2025).
- [52] K. H. Wan, Constant-time magic state distillation, arXiv preprint arXiv:2410.17992 (2024).
- [53] R. Ismail, I. Chen, C. Zhao, R. Weiss, F. Liu, H. Zhou, S.-T. Wang, A. Sornborger, and M. Kornjača, Transversal star architecture for megaqubit-scale quantum simulation with neutral atoms, arXiv preprint arXiv:2509.18294 (2025).
- [54] H. Zhou, C. Duckering, C. Zhao, D. Bluvstein, M. Cain, A. Kubica, S.-T. Wang, and M. D. Lukin, Resource analysis of low-overhead transversal architectures for reconfigurable atom arrays, in *Proceedings of the 52nd Annual International Symposium on Computer Architecture* (2025) pp. 1432–1448.
- [55] D. Litinski, Blocklet concatenation: Low-overhead fault-tolerant protocols for fusion-based quantum computation, arXiv preprint arXiv:2506.13619 (2025).
- [56] C. Gidney, How to factor 2048 bit rsa integers with less than a million noisy qubits, arXiv preprint arXiv:2505.15917 (2025).
- [57] W. J. Huggins, T. Khattar, A. Xu, M. Harrigan, C. Kang, G. H. Low, A. Fowler, N. C. Rubin, and R. Babbush, The fluid allocation of surface code qubits (flasq) cost model for early fault-tolerant quantum algorithms, arXiv preprint arXiv:2511.08508 (2025).
- [58] D. Loss and D. P. DiVincenzo, Quantum computation with quantum dots, *Physical Review A* **57**, 120 (1998).
- [59] L. M. Vandersypen, H. Bluhm, J. S. Clarke, A. S. Dzurak, R. Ishihara, A. Morello, D. J. Reilly, L. R. Schreiber, and M. Veldhorst, Interfacing spin qubits in quantum dots and donors—hot, dense, and coherent, *npj Quantum Information* **3**, 34 (2017).
- [60] Z. Cai, A. Siegel, and S. Benjamin, Looped pipelines enabling effective 3d qubit lattices in a strictly 2d device, *PRX Quantum* **4**, 020345 (2023).
- [61] Z. Sun and Z. Cai, A folded surface code architecture for 2d quantum hardware, arXiv preprint arXiv:2601.19823 (2026).
- [62] J. D. Chadwick, W. Yang, J. Viszlai, and F. T. Chong, A manufacturable surface code architecture for spin qubits with fast transversal logic, arXiv preprint arXiv:2512.07131 (2025).
- [63] D. Pataki and A. Pályi, Compiling the surface code to crossbar spin qubit architectures, *Physical Review B* **111**, 115307 (2025).
- [64] J. M. Boter, J. P. Dehollain, J. P. Van Dijk, Y. Xu, T. Hensgens, R. Versluis, H. W. Naus, J. S. Clarke, M. Veldhorst, F. Sebastiano, *et al.*, Spiderweb array: A sparse spin-qubit array, *Physical review applied* **18**, 024053 (2022).
- [65] A. Siegel, A. Strikis, and M. Fogarty, Towards early fault tolerance on a $2 \times n$ array of qubits equipped with shuttling, *PRX Quantum* **5**, 040328 (2024).
- [66] R. M. Otxoa, J. E. Martinez, P. Schnabl, N. Mertig, C. Smith, and F. Martins, Spinhex: A low-crosstalk, spin-qubit architecture based on multi-electron couplers, arXiv preprint arXiv:2504.03149 (2025).
- [67] R. Li, L. Petit, D. P. Franke, J. P. Dehollain, J. Helsen, M. Steudtner, N. K. Thomas, Z. R. Yoscovits, K. J. Singh, S. Wehner, *et al.*, A crossbar network for silicon quantum dot qubits, *Science advances* **4**, eaar3960 (2018).
- [68] A. Siegel, Z. Cai, H. Jnane, B. Koczor, S. Pexton, A. Strikis, and S. Benjamin, Snakes on a plane: mobile, low dimensional logical qubits on a 2d surface, arXiv preprint arXiv:2501.02120 (2025).
- [69] A. Micciche, F. A. Mian, A. Chatterjee, A. McGregor, and S. Krastanov, Optimizing compilation of error correction codes for $2 \times n$ quantum dot arrays and its np-hardness, arXiv preprint arXiv:2501.09061 (2025).
- [70] M. Gonzalez-Zalba, S. De Franceschi, E. Charbon, T. Meunier, M. Vinet, and A. Dzurak, Scaling silicon-based quantum computing using cmos technology, *Nature Electronics* **4**, 872 (2021).
- [71] T. Ladd, M. Reed, and J. Blumoff, A digitally controlled silicon quantum processing unit, arXiv preprint arXiv:2604.16216 (2026).
- [72] A. J. Moncy, R. Dastbaste, J. E. Martinez, R. Nagai, P. M. Crespo, N. Mertig, C. Smith, and R. M. Otxoa, Surface-code thresholds and qubit footprints in shuttling-based spin-qubit railways, arXiv preprint arXiv:2605.05881 (2026).
- [73] G. Burkard, T. D. Ladd, A. Pan, J. M. Nichol, and J. R. Petta, Semiconductor spin qubits, *Reviews of Modern Physics* **95**, 025003 (2023).
- [74] F. A. Zwanenburg, A. S. Dzurak, A. Morello, M. Y. Simmons, L. C. Hollenberg, G. Klimeck, S. Rogge, S. N. Coppersmith, and M. A. Eriksson, Silicon quantum electronics, *Reviews of modern physics* **85**, 961 (2013).
- [75] M. Veldhorst, H. G. Eenink, C.-H. Yang, and A. S. Dzurak, Silicon cmos architecture for a spin-based quantum computer, *Nature communications* **8**, 1766 (2017).
- [76] S. Neyens, O. K. Zietz, T. F. Watson, F. Luthi, A. Nethewala, H. C. George, E. Henry, M. Islam, A. J. Wagner, F. Borjans, *et al.*, Probing single electrons across 300-mm spin qubit wafers, *Nature* **629**, 80 (2024).
- [77] A. Zwerver, T. Krähenmann, T. Watson, L. Lampert, H. C. George, R. Pillarisetty, S. Bojarski, P. Amin, S. Amitonov, J. Boter, *et al.*, Qubits made by advanced semiconductor manufacturing, *Nature Electronics* **5**, 184 (2022).
- [78] A. Elsayed, M. Shehata, C. Godfrin, S. Kubicek, S. Massar, Y. Canvel, J. Jussot, G. Simion, M. Mongillo, D. Wan, *et al.*, Low charge noise quantum dots with industrial cmos manufacturing, *npj Quantum Information* **10**, 70 (2024).
- [79] P. Stano and D. Loss, Review of performance metrics of spin qubits in gated semiconducting nanostructures, *Nature Reviews Physics* **4**, 672 (2022), (The preprint [80] is regularly updated with new data.).
- [80] P. Stano and D. Loss, Review of performance metrics of spin qubits in gated semiconducting nanostructures (2021), (This preprint is a regularly updated version of Ref. [79]. The latest update at the time of writing is from the 24th of March 2025.), arXiv:2107.06485 [quant-ph].
- [81] R. Maurand, X. Jehl, D. Kotekar-Patil, A. Corna, H. Bohuslavskiy, R. Laviéville, L. Hutin, S. Barraud,

- M. Vinet, M. Sanquer, *et al.*, A cmos silicon spin qubit, *Nature communications* **7**, 13575 (2016).
- [82] I. C. Clarke, V. Ciriano-Tejel, D. J. Ibberson, G. M. Noah, T. H. Swift, M. A. Johnson, R. C. Leon, A. Gomez-Saiz, J. J. Morton, and M. F. Gonzalez-Zalba, Spin readout in a 22 nm node integrated circuit, arXiv preprint arXiv:2510.13674 (2025).
- [83] T. H. Swift, A. Gomez-Saiz, V. N. Ciriano-Tejel, D. F. Wise, G. M. Noah, J. J. Morton, M. F. Gonzalez-Zalba, and M. A. Johnson, Large-scale characterization of single-hole transistors in 22-nm fdsoi cmos technology, arXiv preprint arXiv:2507.21306 (2025).
- [84] T. H. Swift, F. Olivieri, G. Aizpurua-Iraola, J. Kirkman, G. M. Noah, M. de Kruijf, F.-E. von Horstig, A. Gomez-Saiz, J. J. Morton, and M. F. Gonzalez-Zalba, A superinductor in a deep sub-micron integrated circuit, arXiv preprint arXiv:2507.13202 (2025).
- [85] N. W. Hendrickx, W. I. Lawrie, M. Russ, F. Van Riggelen, S. L. De Snoo, R. N. Schouten, A. Sammak, G. Scappucci, and M. Veldhorst, A four-qubit germanium quantum processor, *Nature* **591**, 580 (2021).
- [86] O. Crawford, J. Cruise, N. Mertig, and M. Gonzalez-Zalba, Compilation and scaling strategies for a silicon quantum processor with sparse two-dimensional connectivity, *npj Quantum Information* **9**, 13 (2023).
- [87] F. Ginzler, M. Fellner, C. Ertler, L. R. Schreiber, H. Bluhm, and W. Lechner, Scalable parity architecture with a shuttling-based spin qubit processor, *Physical Review B* **110**, 075302 (2024).
- [88] V. Langrock, J. A. Krzywda, N. Focke, I. Seidler, L. R. Schreiber, and Ł. Cywiński, Blueprint of a scalable spin qubit shuttle device for coherent mid-range qubit transfer in disordered si/sige/sio₂, *PRX Quantum* **4**, 020305 (2023).
- [89] C.-A. Wang, V. John, H. Tidjani, C. X. Yu, A. S. Ivlev, C. Déprez, F. van Riggelen-Doelman, B. D. Woods, N. W. Hendrickx, W. I. Lawrie, *et al.*, Operating semiconductor quantum processors with hopping spins, *Science* **385**, 447 (2024).
- [90] C. Zhang, C. Li, Z. Tian, Y. Jiang, F. Xu, S. Zhang, H. Wang, Y.-N. Zhang, X. Bai, B. Zhao, *et al.*, Demonstration of quantum error detection in a silicon quantum processor, arXiv preprint arXiv:2509.24766 (2025).
- [91] M. T. Mądzik, S. Asaad, A. Youssry, B. Joecker, K. M. Rudinger, E. Nielsen, K. C. Young, T. J. Proctor, A. D. Baczewski, A. Laucht, *et al.*, Precision tomography of a three-qubit donor quantum processor in silicon, *Nature* **601**, 348 (2022).
- [92] A. Noiri, K. Takeda, T. Nakajima, T. Kobayashi, A. Sammak, G. Scappucci, and S. Tarucha, Fast universal quantum gate above the fault-tolerance threshold in silicon, *Nature* **601**, 338 (2022).
- [93] A. R. Mills, C. R. Guinn, M. J. Gullans, A. J. Sigillito, M. M. Feldman, E. Nielsen, and J. R. Petta, Two-qubit silicon quantum processor with operation fidelity exceeding 99%, *Science Advances* **8**, eabn5130 (2022).
- [94] P. Steinacker, N. Dumoulin Stuyck, W. H. Lim, T. Tanttu, M. Feng, S. Serrano, A. Nickl, M. Candido, J. D. Cifuentes, E. Vahapoglu, *et al.*, Industry-compatible silicon spin-qubit unit cells exceeding 99% fidelity, *Nature*, 1 (2025).
- [95] J. Yoneda, K. Takeda, T. Otsuka, T. Nakajima, M. R. Delbecq, G. Allison, T. Honda, T. Kodera, S. Oda, Y. Hoshi, *et al.*, A quantum-dot spin qubit with coherence limited by charge noise and fidelity higher than 99.9%, *Nature nanotechnology* **13**, 102 (2018).
- [96] Y.-H. Wu, L. C. Camenzind, P. Büttler, I. K. Jin, A. Noiri, K. Takeda, T. Nakajima, T. Kobayashi, G. Scappucci, H.-S. Goan, *et al.*, Simultaneous high-fidelity single-qubit gates in a spin qubit array, arXiv preprint arXiv:2507.11918 (2025).
- [97] I. Seidler, T. Struck, R. Xue, N. Focke, S. Trellenkamp, H. Bluhm, and L. R. Schreiber, Conveyor-mode single-electron shuttling in si/sige for a scalable quantum computing architecture, *npj Quantum information* **8**, 100 (2022).
- [98] M. Volmer, T. Struck, J.-S. Tu, S. Trellenkamp, D. D. Eposti, G. Scappucci, Ł. Cywiński, H. Bluhm, and L. R. Schreiber, Reduction of the impact of the local valley splitting on the coherence of conveyor-belt spin shuttling in 28 si/sige, arXiv preprint arXiv:2510.03773 (2025).
- [99] N. Citroth, A. Sala, R. Xue, L. Ermoneit, T. Koprucki, M. Kantner, and L. R. Schreiber, Numerical simulation of coherent spin-shuttling in a qubus with charged defects, arXiv preprint arXiv:2512.03588 (2025).
- [100] M. De Smet, Y. Matsumoto, A.-M. J. Zwerver, L. Tryputen, S. L. de Snoo, S. V. Amitonov, S. R. Katiraeefar, A. Sammak, N. Samkharadze, Ö. Gül, *et al.*, High-fidelity single-spin shuttling in silicon, *Nature Nanotechnology*, 1 (2025).
- [101] Ł. Cywiński, R. M. Lutchyn, C. P. Nave, and S. Das Sarma, How to enhance dephasing time in superconducting qubits, *Physical Review B* **77**, 174509 (2008).
- [102] P. Cerfontaine, T. Hangleiter, and H. Bluhm, Filter functions for quantum processes under correlated noise, *Physical Review Letters* **127**, 170403 (2021).
- [103] J. Z. Blumoff, A. S. Pan, T. E. Keating, R. W. Andrews, D. W. Barnes, T. L. Brecht, E. T. Croke, L. E. Euliss, J. A. Fast, C. A. Jackson, *et al.*, Fast and high-fidelity state preparation and measurement in triple-quantum-dot spin qubits, *PRX Quantum* **3**, 010352 (2022).
- [104] G. Oakes, V. Ciriano-Tejel, D. Wise, M. Fogarty, T. Lundberg, C. Lainé, S. Schaal, F. Martins, D. Ibberson, L. Hutin, *et al.*, Fast high-fidelity single-shot readout of spins in silicon using a single-electron box, *Physical Review X* **13**, 011023 (2023).
- [105] E. J. Connors, J. Nelson, and J. M. Nichol, Rapid high-fidelity spin-state readout in si/si-ge quantum dots via rf reflectometry, *Physical Review Applied* **13**, 024019 (2020).
- [106] D. Keith, M. House, M. Donnelly, T. Watson, B. Weber, and M. Simmons, Single-shot spin readout in semiconductors near the shot-noise sensitivity limit, *Physical Review X* **9**, 041003 (2019).
- [107] M. Künnle, A. Willmes, M. Oberländer, C. Gorjaew, J. D. Teske, H. Bhardwaj, M. Beer, E. Kammerloher, R. Otten, I. Seidler, *et al.*, The spinbus architecture for scaling spin qubits with electron shuttling, *Nature Communications* **15**, 4977 (2024).
- [108] P. Escofet, E. Alarcón, S. Abadal, A. Semenov, N. Murphy, E. Blokhina, and C. G. Almudéver, Quantum reverse mapping: Synthesizing an optimal spin qubit shuttling bus architecture for the surface code, arXiv preprint arXiv:2510.17689 (2025).
- [109] T. Struck, M. Volmer, L. Visser, T. Offermann, R. Xue, J.-S. Tu, S. Trellenkamp, Ł. Cywiński, H. Bluhm, and

- L. R. Schreiber, Spin-epr-pair separation by conveyor-mode single electron shuttling in si/sige, *Nature Communications* **15**, 1325 (2024).
- [110] M. P. Losert, M. Oberländer, J. D. Teske, M. Volmer, L. R. Schreiber, H. Bluhm, S. Coppersmith, and M. Friesen, Strategies for enhancing spin-shuttling fidelities in si/si ge quantum wells with random-alloy disorder, *PRX Quantum* **5**, 040322 (2024).
- [111] R. Xue, M. Beer, I. Seidler, S. Humpohl, J.-S. Tu, S. Trelenkamp, T. Struck, H. Bluhm, and L. R. Schreiber, Si/sige qubus for single electron information-processing devices with memory and micron-scale connectivity function, *Nature Communications* **15**, 2296 (2024).
- [112] M. Volmer, T. Struck, A. Sala, B. Chen, M. Oberländer, T. Offermann, R. Xue, L. Visser, J.-S. Tu, S. Trelenkamp, *et al.*, Mapping of valley splitting by conveyor-mode spin-coherent electron shuttling, *npj Quantum Information* **10**, 61 (2024).
- [113] C. K. Long, N. J. Mayhall, S. E. Economou, E. Barnes, C. H. Barnes, F. Martins, D. R. Arvidsson-Shukur, and N. Mertig, Minimal state-preparation times for silicon spin qubits, *npj Quantum Information* **11**, 113 (2025).
- [114] D. P. Franke, J. S. Clarke, L. M. Vandersypen, and M. Veldhorst, Rent's rule and extensibility in quantum computing, *Microprocessors and Microsystems* **67**, 1 (2019).
- [115] S. J. Devitt, W. J. Munro, and K. Nemoto, Quantum error correction for beginners, *Reports on Progress in Physics* **76**, 076001 (2013).
- [116] A. M. Steane, Overhead and noise threshold of fault-tolerant quantum error correction, *Physical Review A* **68**, 042322 (2003).
- [117] N. Lacroix, A. Bourassa, F. J. Heras, L. M. Zhang, J. Bausch, A. W. Senior, T. Edlich, N. Shutty, V. Sivak, A. Bengtsson, *et al.*, Scaling and logic in the color code on a superconducting quantum processor, *Nature*, 1 (2025).
- [118] F. Thomsen, M. S. Kesselring, S. D. Bartlett, and B. J. Brown, Low-overhead quantum computing with the color code, *Physical Review Research* **6**, 043125 (2024).
- [119] C. Chamberland, A. Kubica, T. J. Yoder, and G. Zhu, Triangular color codes on trivalent graphs with flag qubits, *New Journal of Physics* **22**, 023019 (2020).
- [120] K. Fujiu, S. Nagayama, S. Nishio, H. Kawaguchi, and T. Satoh, Dense packing of the surface code: Code deformation procedures and hook-error-avoiding gate scheduling, *Physical Review A* **113**, 042412 (2026).
- [121] J. P. Bonilla Ataides, D. K. Tuckett, S. D. Bartlett, S. T. Flammia, and B. J. Brown, The xxxz surface code, *Nature communications* **12**, 2172 (2021).
- [122] J. Roffe, L. Z. Cohen, A. O. Quintavalle, D. Chandra, and E. T. Campbell, Bias-tailored quantum ldpc codes, *Quantum* **7**, 1005 (2023).
- [123] D. K. Tuckett, S. D. Bartlett, and S. T. Flammia, Ultra-high error threshold for surface codes with biased noise, *Physical review letters* **120**, 050505 (2018).
- [124] D. K. Tuckett, A. S. Darmawan, C. T. Chubb, S. Bravyi, S. D. Bartlett, and S. T. Flammia, Tailoring surface codes for highly biased noise, *Physical Review X* **9**, 041031 (2019).
- [125] J. F. San Miguel, D. J. Williamson, and B. J. Brown, A cellular automaton decoder for a noise-bias tailored color code, *Quantum* **7**, 940 (2023).
- [126] D. K. Tuckett, S. D. Bartlett, S. T. Flammia, and B. J. Brown, Fault-tolerant thresholds for the surface code in excess of 5% under biased noise, *Physical review letters* **124**, 130501 (2020).
- [127] A. Messinger, V. Torggler, B. Klaver, M. Fellner, and W. Lechner, Fault-tolerant quantum computing with the parity code and biased-noise qubits, *Physical Review Applied* **23**, 044032 (2025).
- [128] J. Etchezarreta Martinez, P. Schnabl, J. Oliva del Moral, R. Dastbasteh, P. M. Crespo, and R. M. Otxoa, Leveraging biased noise for more efficient quantum error correction at the circuit level with two-level qubits, *Physical Review Applied* **25**, 014021 (2026).
- [129] A. J. Landahl and C. Ryan-Anderson, Quantum computing by color-code lattice surgery, *arXiv preprint arXiv:1407.5103* (2014).
- [130] K. Sahay, Y. Lin, S. Huang, K. R. Brown, and S. Puri, Error correction of transversal cnot gates for scalable surface-code computation, *PRX quantum* **6**, 020326 (2025).
- [131] C. Ryan-Anderson, N. Brown, M. Allman, B. Arkin, G. Asa-Attuah, C. Baldwin, J. Berg, J. Bohnet, S. Braxton, N. Burdick, *et al.*, Implementing fault-tolerant entangling gates on the five-qubit code and the color code, *arXiv preprint arXiv:2208.01863* (2022).
- [132] R. Laflamme, C. Miquel, J. P. Paz, and W. H. Zurek, Perfect quantum error correcting code, *Physical Review Letters* **77**, 198 (1996).
- [133] M. Gong, X. Yuan, S. Wang, Y. Wu, Y. Zhao, C. Zha, S. Li, Z. Zhang, Q. Zhao, Y. Liu, *et al.*, Experimental exploration of five-qubit quantum error-correcting code with superconducting qubits, *National Science Review* **9**, nwab011 (2022).
- [134] C. Chamberland and E. T. Campbell, Circuit-level protocol and analysis for twist-based lattice surgery, *Physical Review Research* **4**, 023090 (2022).
- [135] D. Litinski and F. von Oppen, Lattice surgery with a twist: Simplifying clifford gates of surface codes, *Quantum* **2**, 62 (2018).
- [136] G. Zhang, Y. Zhu, X. Yuan, and Y. Li, Constant-overhead magic state injection into qldpc codes with error independence guarantees, *arXiv preprint arXiv:2505.06981* (2025).
- [137] S. Yoshida, S. Tamiya, and H. Yamasaki, Concatenate codes, save qubits, *npj Quantum Information* **11**, 88 (2025).
- [138] D. Ruiz, J. Guillaud, C. Vuillot, and M. Mirrahimi, Unfolded distillation: very low-cost magic state preparation for biased-noise qubits, *arXiv preprint arXiv:2507.12511* (2025).
- [139] S. Wu, T. A. Brun, and D. A. Lidar, Bias-tailored single-shot quantum ldpc codes, *arXiv preprint arXiv:2507.02239* (2025).
- [140] H. Goto, Step-by-step magic state encoding for efficient fault-tolerant quantum computation, *Scientific Reports* **4**, 7501 (2014).
- [141] M. Erew, M. Goldstein, Y. Oz, and H. Suchowski, Pre-distillation of magic states via composite schemes, *arXiv preprint arXiv:2510.00804* (2025).
- [142] N. Fazio, M. Webster, and Z. Cai, Low-overhead magic state circuits with transversal cnots, *arXiv preprint arXiv:2501.10291* (2025).
- [143] H. Choi, F. T. Chong, D. Englund, and Y. Ding, Fault

- tolerant non-clifford state preparation for arbitrary rotations, arXiv preprint arXiv:2303.17380 (2023).
- [144] J. Gavriel, D. Herr, A. Shaw, M. J. Bremner, A. Paler, and S. J. Devitt, Transversal injection: A method for direct encoding of ancilla states for non-clifford gates using stabiliser codes, arXiv preprint arXiv:2211.10046 (2022).
- [145] F. Butt, S. Heußen, M. Rispler, and M. Müller, Fault-tolerant code-switching protocols for near-term quantum processors, PRX Quantum **5**, 020345 (2024).
- [146] L. Daguerre and I. H. Kim, Code switching revisited: Low-overhead magic state preparation using color codes, Physical Review Research **7**, 023080 (2025).
- [147] J. Zhang, Y.-C. Wu, and G.-P. Guo, Facilitating practical fault-tolerant quantum computing based on color codes, Physical Review Research **6**, 033086 (2024).
- [148] S. Yoshida, C. Gidney, M. McEwen, and A. Zalcman, Low depth color code circuits with cxswap gate, arXiv preprint arXiv:2510.00370 (2025).
- [149] S.-H. Lee, F. Thomsen, N. Fazio, B. J. Brown, and S. D. Bartlett, Low-overhead magic state distillation with color codes, PRX Quantum **6**, 030317 (2025).
- [150] Y. Hirano, R. Toshio, T. Itogawa, and K. Fujii, Efficient magic state cultivation with lattice surgery, arXiv preprint arXiv:2510.24615 (2025).
- [151] Z.-H. Chen, M.-C. Chen, C.-Y. Lu, and J.-W. Pan, Efficient magic state cultivation on $\mathbb{R}\mathbb{P}^2$, arXiv preprint arXiv:2503.18657 (2025).
- [152] Y. Vaknin, S. Jacoby, A. Grimsmo, and A. Retzker, Magic state cultivation on the surface code, arXiv preprint arXiv:2502.01743 (2025).
- [153] E. Rosenfeld, C. Gidney, G. Roberts, A. Morvan, N. Lacroix, D. Kafri, J. Marshall, M. Li, V. Sivak, D. Abanin, *et al.*, Magic state cultivation on a superconducting quantum processor, arXiv preprint arXiv:2512.13908 (2025).
- [154] C. Gidney, N. Shutty, and C. Jones, Magic state cultivation: growing t states as cheap as cnot gates, arXiv preprint arXiv:2409.17595 (2024).
- [155] T. Itogawa, Y. Takada, Y. Hirano, and K. Fujii, Even more efficient magic state distillation by zero-level distillation, arXiv preprint arXiv:2403.03991 (2024).
- [156] K. Bolsmann, T. L. Guedes, W. Li, J. W. Wilkinson, I. Lesanovsky, and M. Müller, Fast native three-qubit gates and fault-tolerant quantum error correction with trapped rydberg ions, arXiv preprint arXiv:2512.16641 (2025).
- [157] J. Old, S. Tasler, M. J. Hartmann, and M. Müller, Fault-tolerant stabilizer measurements in surface codes with three-qubit gates, Physical Review Letters **135**, 240601 (2025).
- [158] S. Tasler, J. Old, L. Heunisch, V. Feulner, T. Eckstein, M. Müller, and M. J. Hartmann, Optimizing superconducting three-qubit gates for surface-code error correction, arXiv preprint arXiv:2506.09028 (2025).
- [159] D. R. M. Arvidsson-Shukur, H. V. Lepage, E. T. Owen, T. Ferrus, and C. H. W. Barnes, Protocol for fermionic positive-operator-valued measures, Phys. Rev. A **96**, 052305 (2017).
- [160] H. V. Lepage, A. A. Lasek, D. R. M. Arvidsson-Shukur, and C. H. W. Barnes, Entanglement generation via power-of-swap operations between dynamic electron-spin qubits, Phys. Rev. A **101**, 022329 (2020).
- [161] D. W. Berry, G. Ahokas, R. Cleve, and B. C. Sanders, Efficient quantum algorithms for simulating sparse hamiltonians, Communications in Mathematical Physics **270**, 359 (2007).
- [162] M. Suzuki, Fractal decomposition of exponential operators with applications to many-body theories and Monte Carlo simulations, Phys. Lett. A **146**, 319 (1990).
- [163] C. K. Long, C. H. W. Barnes, and N. Mertig, Suzukitrotter-evolver (v1.1.0) (2025), <https://doi.org/10.5281/zenodo.17116352>.
- [164] H. Gothen, C. K. Long, D. Hiller, Y. Qian, C. H. W. Barnes, N. Mertig, and D. R. M. Arvidsson-Shukur, Pulse-optimised circuit elements for scalable and noise-resilient quantum chemistry, in preparation.
- [165] J. Y. Huang, R. Y. Su, W. H. Lim, M. Feng, B. van Straaten, B. Severin, W. Gilbert, N. Dumoulin Stuyck, T. Tanttu, S. Serrano, J. D. Cifuentes, I. Hansen, A. E. Seedhouse, E. Vahapoglu, R. C. C. Leon, N. V. Abrosimov, H.-J. Pohl, M. L. W. Thewalt, F. E. Hudson, C. C. Escott, N. Ares, S. D. Bartlett, A. Morello, A. Saraiva, A. Laucht, A. S. Dzurak, and C. H. Yang, High-fidelity spin qubit operation and algorithmic initialization above 1 K, Nature **627**, 772 (2024).
- [166] T. Tanttu, W. H. Lim, J. Y. Huang, N. Dumoulin Stuyck, W. Gilbert, R. Y. Su, M. Feng, J. D. Cifuentes, A. E. Seedhouse, S. K. Seritan, C. I. Ostrove, K. M. Rudinger, R. C. C. Leon, W. Huang, C. C. Escott, K. M. Itoh, N. V. Abrosimov, H.-J. Pohl, M. L. W. Thewalt, F. E. Hudson, R. Blume-Kohout, S. D. Bartlett, A. Morello, A. Laucht, C. H. Yang, A. Saraiva, and A. S. Dzurak, Assessment of the errors of high-fidelity two-qubit gates in silicon quantum dots, Nat. Phys. **20**, 1804 (2024).
- [167] S. G. Philips, M. T. Madzik, S. V. Amitonov, S. L. de Snoo, M. Russ, N. Kalhor, C. Volk, W. I. Lawrie, D. Brousse, L. Tryputen, *et al.*, Universal control of a six-qubit quantum processor in silicon, Nature **609**, 919 (2022).
- [168] C. K. Long, C. H. W. Barnes, and N. Mertig, Qugrad (2025).
- [169] N. Khaneja, T. Reiss, C. Kehlet, T. Schulte-Herbrüggen, and S. J. Glaser, Optimal control of coupled spin dynamics: design of nmr pulse sequences by gradient ascent algorithms, Journal of Magnetic Resonance **172**, 296 (2005).
- [170] L. Lao and B. Criger, Magic state injection on the rotated surface code, in *Proceedings of the 19th ACM International Conference on Computing Frontiers* (2022) pp. 113–120.
- [171] A. R. O'Rourke and S. Devitt, Compare the pair: Rotated versus unrotated surface codes at equal logical error rates, Physical Review Research **7**, 033074 (2025).
- [172] Y. Tomita and K. M. Svore, Low-distance surface codes under realistic quantum noise, arXiv preprint arXiv:1404.3747 (2014).
- [173] J. Ghosh, A. G. Fowler, and M. R. Geller, Surface code with decoherence: An analysis of three superconducting architectures, Physical Review A—Atomic, Molecular, and Optical Physics **86**, 062318 (2012).
- [174] P. K. Sarvepalli, A. Klappenecker, and M. Rötteler, Asymmetric quantum codes: constructions, bounds and performance, Proceedings of the Royal Society A: Mathematical, Physical and Engineering Sciences **465**, 1645 (2009).
- [175] M. Silva, E. Magesan, D. W. Kribs, and J. Emerson,

- Scalable protocol for identification of correctable codes, *Physical Review A—Atomic, Molecular, and Optical Physics* **78**, 012347 (2008).
- [176] C. Gidney, Stim: a fast stabilizer circuit simulator, *Quantum* **5**, 497 (2021).
- [177] P. Dutta and P. Horn, Low-frequency fluctuations in solids: 1/f noise, *Reviews of Modern physics* **53**, 497 (1981).
- [178] S. Machlup, Noise in semiconductors: spectrum of a two-parameter random signal, *Journal of Applied Physics* **25**, 341 (1954).
- [179] D. Fleetwood, 1/f noise and defects in microelectronic materials and devices, *IEEE Transactions on Nuclear Science* **62**, 1462 (2015).
- [180] M. M. E. K. Shehata, G. Simion, R. Li, F. A. Mohiyaddin, D. Wan, M. Mongillo, B. Govoreanu, I. Radu, K. De Greve, and P. Van Dorpe, Modeling semiconductor spin qubits and their charge noise environment for quantum gate fidelity estimation, *Physical Review B* **108**, 045305 (2023).
- [181] J. Ager III, J. Beeman, W. Hansen, E. Haller, I. Sharp, C. Liao, A. Yang, M. Thewalt, and H. Riemann, High-purity, isotopically enriched bulk silicon, *Journal of the Electrochemical Society* **152**, G448 (2005).
- [182] T. Hangleiter, P. Cerfontaine, and H. Bluhm, Filter-function formalism and software package to compute quantum processes of gate sequences for classical non-markovian noise, *Physical Review Research* **3**, 043047 (2021).
- [183] M. Newman and R. M. Ziff, Efficient monte carlo algorithm and high-precision results for percolation, *Physical Review Letters* **85**, 4104 (2000).
- [184] D. Culcer, X. Hu, and S. Das Sarma, Dephasing of si spin qubits due to charge noise, *Applied Physics Letters* **95** (2009).
- [185] T. H. Cormen, C. E. Leiserson, R. L. Rivest, and C. Stein, *Introduction to algorithms* (MIT press, 2022).
- [186] C. Flindt, A. S. Sørensen, and K. Flensberg, Spin-orbit mediated control of spin qubits, *Physical review letters* **97**, 240501 (2006).
- [187] L. Levitov and E. Rashba, Dynamical spin-electric coupling in a quantum dot, arXiv preprint cond-mat/0209507 (2002).
- [188] E. Rashba and A. L. Efros, Orbital mechanisms of electron-spin manipulation by an electric field, *Physical review letters* **91**, 126405 (2003).
- [189] M. E. Beverland, A. Kubica, and K. M. Svore, Cost of universality: A comparative study of the overhead of state distillation and code switching with color codes, *PRX Quantum* **2**, 020341 (2021).
- [190] Y. Kim, M. Sevier, and M. Usman, Magic state injection on ibm quantum processors above the distillation threshold, arXiv preprint arXiv:2412.01446 (2024).
- [191] J. Claes, Lower-depth local encoding circuits for the surface code, arXiv preprint arXiv:2509.09779 (2025).
- [192] O. Higgott, M. Wilson, J. Hefford, J. Dborin, F. Hanif, S. Burton, and D. E. Browne, Optimal local unitary encoding circuits for the surface code, *Quantum* **5**, 517 (2021).
- [193] M. B. Hastings and J. Haah, Distillation with sublogarithmic overhead, *Physical review letters* **120**, 050504 (2018).
- [194] A. M. Steane, Quantum reed-muller codes, *IEEE Transactions on Information Theory* **45**, 1701 (2002).
- [195] T. Jochym-O'Connor, Y. Yu, B. Helou, and R. Laflamme, The robustness of magic state distillation against errors in clifford gates, arXiv preprint arXiv:1205.6715 (2012).
- [196] S. Dasu, S. Burton, K. Mayer, D. Amaro, J. A. Gerber, K. Gilmore, D. Gresh, D. DelVento, A. C. Potter, and D. Hayes, Breaking even with magic: demonstration of a high-fidelity logical non-clifford gate, arXiv preprint arXiv:2506.14688 (2025).
- [197] J. O’Gorman and E. T. Campbell, Quantum computation with realistic magic-state factories, *Physical Review A* **95**, 032338 (2017).
- [198] V. Kliuchnikov, K. Lauter, R. Minko, A. Paetznick, and C. Petit, Shorter quantum circuits via single-qubit gate approximation, *Quantum* **7**, 1208 (2023).
- [199] Y. Kim, A. Eddins, S. Anand, K. X. Wei, E. Van Den Berg, S. Rosenblatt, H. Nayfeh, Y. Wu, M. Zaletel, K. Temme, *et al.*, Evidence for the utility of quantum computing before fault tolerance, *Nature* **618**, 500 (2023).
- [200] N. Hatano and M. Suzuki, Finding exponential product formulas of higher orders, in *Quantum annealing and other optimization methods* (Springer, 2005) pp. 37–68.
- [201] G. H. Low and I. L. Chuang, Hamiltonian simulation by qubitization, *Quantum* **3**, 163 (2019).
- [202] V. von Burg, G. H. Low, T. Häner, D. S. Steiger, M. Reiher, M. Roetteler, and M. Troyer, Quantum computing enhanced computational catalysis, *Physical Review Research* **3**, 033055 (2021).
- [203] A. M. Childs and N. Wiebe, Hamiltonian simulation using linear combinations of unitary operations, arXiv preprint arXiv:1202.5822 (2012).
- [204] M. Cain, Q. Xu, R. King, L. R. Picard, H. Levine, M. Endres, J. Preskill, H.-Y. Huang, and D. Bluvstein, Shor’s algorithm is possible with as few as 10,000 reconfigurable atomic qubits, arXiv preprint arXiv:2603.28627 (2026).
- [205] R. Babbush, A. Zalcman, C. Gidney, M. Broughton, T. Khattar, H. Neven, T. Bergamaschi, J. Drake, and D. Boneh, Securing elliptic curve cryptocurrencies against quantum vulnerabilities: Resource estimates and mitigations, arXiv preprint arXiv:2603.28846 (2026).
- [206] P. Webster, L. Berent, O. Chandra, E. T. Hockings, N. Baspin, F. Thomsen, S. C. Smith, and L. Z. Cohen, The pinnacle architecture: Reducing the cost of breaking rsa-2048 to 100 000 physical qubits using quantum ldpc codes, arXiv preprint arXiv:2602.11457 (2026).
- [207] H. Luo, Z. Yang, Z. Wang, Y. Su, and T. Li, Space-efficient quantum algorithm for elliptic curve discrete logarithms with resource estimation, arXiv preprint arXiv:2604.02311 (2026).
- [208] D. Q. Nguyen, M. Rimbach-Russ, and S. Bosco, Suppressing spin qubit decoherence during shuttling via confinement modulation, arXiv preprint arXiv:2605.00611 (2026).
- [209] S. Heußen, Magic state distillation without measurements and post-selection, arXiv preprint arXiv:2504.17509 (2025).
- [210] J. D. Chadwick and F. T. Chong, Cablecar: efficiently scheduling qldpc codes on a tileable spin qubit chip with shuttling, arXiv preprint arXiv:2604.24739 (2026).
- [211] H. Bombín, Resilience to time-correlated noise in quantum computation, *Physical Review X* **6**, 041034 (2016).

- [212] Z. Liu, Y. Xiao, and Z. Cai, Non-markovian noise suppression simplified through channel representation, arXiv preprint arXiv:2412.11220 (2024).
- [213] S. Blanes, F. Casas, J.-A. Oteo, and J. Ros, The magnus expansion and some of its applications, *Physics reports* **470**, 151 (2009).
- [214] T. J. Green, J. Sastrawan, H. Uys, and M. J. Biercuk, Arbitrary quantum control of qubits in the presence of universal noise, *New Journal of Physics* **15**, 095004 (2013).
- [215] S. Kimmel, M. P. da Silva, C. A. Ryan, B. R. Johnson, and T. Ohki, Robust extraction of tomographic information via randomized benchmarking, *Physical Review X* **4**, 011050 (2014).
- [216] M. A. Nielsen, A simple formula for the average gate fidelity of a quantum dynamical operation, *Physics Letters A* **303**, 249 (2002).

Supplemental Material

I. NON-MARKOVIAN NOISE DERIVATION

In this appendix, we will derive the expression for Eq. 13. We start by considering a system evolving under a time-dependent Hamiltonian

$$H(t) = H_c(t) + H_n(t), \quad H_n(t) = \sum_{\alpha} b_{\alpha}(t)B_{\alpha}, \quad (\text{S1})$$

where $H_c(t)$ is the control Hamiltonian as in Eq. (7) and $H_n(t)$ describes classical stochastic noise [182]. The stochastic processes $b_{\alpha}(t)$ are assumed to be zero mean, and the operators B_{α} are fixed Pauli strings acting on the noisy subsystem, which are time independent. We direct the interested readers to [102] for the general time-dependent framework. We denote the control propagator by $U_c(t)$ satisfying Schrödinger's equation $i\frac{d}{dt}U_c(t) = H_c(t)U_c(t)$, $U_c(0) = \mathbb{I}$. In the interaction picture, the noise Hamiltonian is

$$\tilde{H}_n(t) = U_c^{\dagger}(t)H_n(t)U_c(t),$$

and the interaction-picture propagator $\tilde{U}(t) = U_c^{\dagger}(t)U(t)$ obeys

$$i\frac{d}{dt}\tilde{U}(t) = \tilde{H}_n(t)\tilde{U}(t), \quad \tilde{U}(0) = \mathbb{I}.$$

Applying the Magnus expansion [213] over a gate interval $[0, \tau]$ we can write down the evolution operator,

$$\tilde{U}(\tau) = \exp(-i\tau H_{\text{eff}}), \quad H_{\text{eff}} = \sum_{\mu \geq 1} H_{\text{eff};\mu},$$

in terms of an effective Hamiltonian, H_{eff} . Providing the noise strength $\xi \equiv \sum \|B_{\alpha}\| \sqrt{\langle b_{\alpha}(0)^2 \rangle} \tau \ll 1$ we can neglect higher order terms and just retain the first two:

$$H_{\text{eff};1} = 1/\tau \int_0^{\tau} dt \tilde{H}_n(t) \quad (\text{S2})$$

$$H_{\text{eff};2} = -\frac{i}{2\tau} \int_0^{\tau} dt_1 \int_0^{t_1} dt_2 [\tilde{H}_n(t_1), \tilde{H}_n(t_2)]. \quad (\text{S3})$$

Taylor expanding the evolution to second order yields the map

$$\tilde{U}\rho\tilde{U}^{\dagger} = \rho + \mathcal{L}^{(1)}(\rho) + \mathcal{L}^{(2)}(\rho) + O(\xi^3),$$

where $\mathcal{L}^{(1)}(\rho) = -i\tau[H_{\text{eff};1}, \rho]$, and $\mathcal{L}^{(2)}(\rho) = -i\tau[H_{\text{eff};2}, \rho] + \tau^2 H_{\text{eff};1}\rho H_{\text{eff};1} - \frac{1}{2}\tau^2\{H_{\text{eff};1}^2, \rho\}$. Because the stochastic processes $b_{\alpha}(t)$ are zero mean, any terms with an odd number of $\tilde{H}_n(t)$ will average to zero, such as $\mathbb{E}[H_{\text{eff};1}] = 0$ and consequently $\mathbb{E}[\mathcal{L}^{(1)}] = 0$. Keeping terms to $O(\xi^2)$ and averaging over the noise yields the leading-order dissipative contribution

$$\frac{\mathbb{E}[\tilde{U}\rho\tilde{U}^{\dagger}] - \rho}{\tau} = -i\mathbb{E}[H_{\text{eff};2}, \rho] + \tau\mathbb{E}[H_{\text{eff};1}\rho H_{\text{eff};1}] - \frac{1}{2}\tau\mathbb{E}\{H_{\text{eff};1}^2, \rho\} + O(\xi^3).$$

To obtain explicit expressions we expand \tilde{H}_n in an orthonormal basis of the Hermitian operators, $\{\sigma_k\}$ (with $\text{Tr}(\sigma_k\sigma_l) = D\delta_{kl}$):

$$\begin{aligned} \tilde{H}_n(t) &= \sum_{\alpha,k} b_{\alpha}(t)\tilde{B}_{\alpha k}(t)\sigma_k, \\ \tilde{B}_{\alpha k}(t) &= \text{Tr}[U_c^{\dagger}(t)B_{\alpha}U_c(t)\sigma_k]. \end{aligned}$$

Next, we define the second-order kernels, where the scalar $\tilde{B}_{\alpha k}(t)$ is time-dependent and the expectation value is taken over the stochastic process $b_{\alpha}(t)$:

$$\Gamma_{\alpha;kl} \equiv \int_0^{\tau} dt_1 \int_0^{\tau} dt_2 \mathbb{E}[b_{\alpha}(t_1)b_{\alpha}(t_2)]\tilde{B}_{\alpha k}(t_1)\tilde{B}_{\alpha l}(t_2). \quad (\text{S4})$$

Then, we define the two-point autocorrelation function $C_\alpha(\tau)$, which depends only on the time difference,

$$C_\alpha(\tau) = C_\alpha(t_1 - t_2) = \mathbb{E}[b_\alpha(t_1)b_\alpha(t_2)] \quad (\text{S5})$$

so that

$$\Gamma_{\alpha;kl} = \int_0^\tau dt_1 \int_0^\tau dt_2 C_\alpha(t_1 - t_2) \tilde{B}_{\alpha k}(t_1) \tilde{B}_{\alpha l}(t_2). \quad (\text{S6})$$

Assuming a noise spectral density $S_\alpha(\omega)$ defined via

$$C_\alpha(\tau) = \int_{-\infty}^{\infty} \frac{d\omega}{2\pi} S_\alpha(\omega) e^{-i\omega\tau}, \quad (\text{S7})$$

we substitute this representation into Eq. (S6) to obtain

$$\begin{aligned} \Gamma_{\alpha;kl} &= \int_0^\tau dt_1 \int_0^\tau dt_2 \int_{-\infty}^{\infty} \frac{d\omega}{2\pi} S_\alpha(\omega) e^{-i\omega(t_1-t_2)} \tilde{B}_{\alpha k}(t_1) \tilde{B}_{\alpha l}(t_2) \\ &= \int_{-\infty}^{\infty} \frac{d\omega}{2\pi} S_\alpha(\omega) \left[\int_0^\tau dt_1 e^{-i\omega t_1} \tilde{B}_{\alpha k}(t_1) \right] \left[\int_0^\tau dt_2 e^{+i\omega t_2} \tilde{B}_{\alpha l}(t_2) \right]. \end{aligned} \quad (\text{S8})$$

Defining the finite-time Fourier transforms

$$\tilde{\mathbb{B}}_{\alpha k}(\omega) \equiv \int_0^\tau dt e^{i\omega t} \tilde{B}_{\alpha k}(t), \quad (\text{S9})$$

we identify

$$\int_0^\tau dt_1 e^{-i\omega t_1} \tilde{B}_{\alpha k}(t_1) = \tilde{\mathbb{B}}_{\alpha k}^*(\omega), \quad (\text{S10})$$

which finally yields

$$\Gamma_{\alpha;kl} = \int_{-\infty}^{\infty} \frac{d\omega}{2\pi} S_\alpha(\omega) \tilde{\mathbb{B}}_{\alpha k}^*(\omega) \tilde{\mathbb{B}}_{\alpha l}(\omega). \quad (\text{S11})$$

Assuming independent noise channels $\mathbb{E}[b_\alpha(t_1)b_\beta(t_2)] = \delta_{\alpha\beta}\mathbb{E}[b_\alpha(t_1)b_\alpha(t_2)]$, we obtain

$$\tau^2 \mathbb{E}[H_{\text{eff};1} \rho H_{\text{eff};1}] = \sum_\alpha \sum_{k,l} \int_0^\tau dt_1 \int_0^\tau dt_2 \mathbb{E}[b_\alpha(t_1)b_\alpha(t_2)] \tilde{B}_{\alpha k}(t_1) \tilde{B}_{\alpha l}(t_2) \sigma_k \rho \sigma_l.$$

We can also express it with the kernel

$$\tau^2 \mathbb{E}[H_{\text{eff};1} \rho H_{\text{eff};1}] = \sum_{\alpha,k,l} \Gamma_{\alpha;kl} \sigma_k \rho \sigma_l. \quad (\text{S12})$$

Similarly,

$$\mathbb{E}[H_{\text{eff};1}^2] = \frac{1}{\tau^2} \sum_{\alpha,k,l} \Gamma_{\alpha;kl} \sigma_k \sigma_l. \quad (\text{S13})$$

Therefore,

$$\frac{1}{2} \tau^2 \mathbb{E}[\{H_{\text{eff};1}^2, \rho\}] = \frac{1}{2} \sum_{\alpha,k,l} \Gamma_{\alpha;kl} \{\sigma_k \sigma_l, \rho\}. \quad (\text{S14})$$

One then finds the averaged dissipator

$$\mathbb{E}[\tilde{U} \rho \tilde{U}^\dagger] - \rho = \sum_\alpha \sum_{k,l} \Gamma_{\alpha;kl} \left(\sigma_k \rho \sigma_l - \frac{1}{2} \{\sigma_k \sigma_l, \rho\} \right) - i\tau \mathbb{E}[[H_{\text{eff};2}, \rho]] + O(\xi^3).$$

Since the term containing $H_{\text{eff};2}$, it does not contribute to the average gate fidelity of the quantum operation. Thus, we will drop this term from now on. To calculate the average gate fidelity, we express $\mathbb{E}[\tilde{U}\rho\tilde{U}^\dagger]$ as $\tilde{\mathcal{E}}[\rho]$, the noise-averaged quantum process. Then we can use the average gate fidelity formula $F = (\text{Tr}[\tilde{\mathcal{E}}] + D)/(D^2 + D)$ [214–216] where D is the Hilbert-space dimension. Writing $\tilde{\mathcal{E}} = \mathbb{1} + \mathcal{D} + O(\xi^3)$, with

$$\mathcal{D}(\rho) = \sum_{\alpha,k,l} \Gamma_{\alpha;kl} \left(\sigma_k \rho \sigma_l - \frac{1}{2} \{ \sigma_k \sigma_l, \rho \} \right), \quad (\text{S15})$$

and since $\text{Tr}[\mathbb{1}] = D$, the leading-order infidelity is

$$\epsilon = \frac{D^2 - \text{Tr}[\mathcal{D}]}{D(D+1)}. \quad (\text{S16})$$

Substituting the explicit form of \mathcal{D} and decomposing it in the complete basis σ_i yields

$$\sum_j \text{Tr}[\sigma_j \mathcal{D}(\sigma_j)] = \sum_{\alpha,k,l} \Gamma_{\alpha;kl} \sum_j \text{Tr} \left[\sigma_j \left(\sigma_k \sigma_j \sigma_l - \frac{1}{2} \{ \sigma_k \sigma_l, \sigma_j \} \right) \right].$$

Using completeness and orthonormality of the operator basis, the fidelity yields

$$\epsilon = \frac{1}{D+1} \sum_{\alpha,k} \Gamma_{\alpha;kk}. \quad (\text{S17})$$

Using the frequency-domain representation of the kernel,

$$\Gamma_{\alpha;kk} = \int_{-\infty}^{\infty} \frac{d\omega}{2\pi} S_\alpha(\omega) |\tilde{\mathbb{B}}_{\alpha k}(\omega)|^2, \quad (\text{S18})$$

we finally obtain Eq. 13. For the noise spectral-density function considered as Eq. 30, the autocorrelation function becomes

$$C(\tau) \approx \int_{\omega_{\text{low}}}^{\omega_{\text{high}}} \frac{d\omega}{\pi} \frac{\cos(\omega\tau)}{\omega} A = \frac{A}{\pi} \int_{\omega_{\text{low}}}^{\omega_{\text{high}}} \frac{\cos(\omega\tau)}{\omega} d\omega = \frac{A}{\pi} [\text{Ci}(\omega_{\text{high}}\tau) - \text{Ci}(\omega_{\text{low}}\tau)], \quad (\text{S19})$$

where $\text{Ci}(x)$ is the cosine integral function $\text{Ci}(x) = -\int_x^\infty \frac{\cos t}{t} dt$. For intermediate times $\tau \gg 1/\omega_{\text{high}}$, $\text{Ci}(\omega_{\text{high}}\tau) \rightarrow 0$ and $\text{Ci}(\omega_{\text{low}}\tau) \approx \gamma_E + \ln(1/(\omega_{\text{low}}\tau))$, so

$$C(\tau) \approx \frac{A}{\pi} \left(\ln \left(\frac{1}{\omega_{\text{high}}\tau} \right) - \gamma_E \right), \quad (\text{S20})$$

where γ_E is Euler's constant. The correlation function decays logarithmically in this regime, while we can show that at high frequencies $S(\omega) \approx \frac{A\omega_{\text{high}}^2}{|\omega|^3}$, and the correlations decay quadratically, $C(\tau) \sim \frac{A}{\omega_{\text{low}} \tau^2}$, reflecting the finite span of the correlation noise. This scaling is derived by approximating the integral in the $\tau \ll 1/\omega$, then

$$\begin{aligned} C(\tau) &= \int_0^\infty \frac{d\omega}{\pi} \cos(\omega\tau) \frac{A\omega_{\text{high}}^2}{\omega^3} \\ &\approx \frac{A\omega_{\text{high}}^2}{\pi} \int_{\omega_{\text{high}}}^{\frac{1}{\tau}} d\omega \left(1 - \frac{(\omega\tau)^2}{2} \right) \frac{1}{\omega^3} \sim \tau^2. \end{aligned} \quad (\text{S21})$$

II. MAPPING NON-MARKOVIAN NOISE ONTO PAULI CHANNEL

In this appendix, we explain how we mapped the correlated noise onto the Pauli channel. For a single qubit, the maximally entangled state $|\Phi_2^+\rangle = \frac{1}{\sqrt{2}}(|00\rangle + |11\rangle)$ can be expressed in the Pauli basis as,

$$|\Phi_2^+\rangle\langle\Phi_2^+| = \frac{1}{4} \sum_{P \in \{I, X, Y, Z\}} P \otimes P^T. \quad (\text{S22})$$

For n qubits, the maximally entangled state $|\Phi_{2^n}^+\rangle$ between subsystems A and B (each of dimension 2^n) factorizes,

$$\begin{aligned} |\Phi_{2^n}^+\rangle_{AB} &:= \sum_{i \in \{0,1\}^n} |i\rangle_A \otimes |i\rangle_B \\ &= \sum_{i_1, \dots, i_n \in \{0,1\}} |i_1 \dots i_n\rangle_A \otimes |i_1 \dots i_n\rangle_B \\ &= \sum_{i_1, \dots, i_n \in \{0,1\}} |i_1\rangle_A |i_1\rangle_B \otimes \dots \otimes |i_n\rangle_A |i_n\rangle_B \\ &= \left(\sum_{i_1 \in \{0,1\}} |i_1\rangle_A |i_1\rangle_B \right) \otimes \dots \otimes \left(\sum_{i_n \in \{0,1\}} |i_n\rangle_A |i_n\rangle_B \right) \\ &= |\Phi_2^+\rangle_{AB} \otimes \dots \otimes |\Phi_2^+\rangle_{AB}. \end{aligned} \quad (\text{S23})$$

Therefore, the density matrix is,

$$\begin{aligned} |\Phi_{2^n}^+\rangle\langle\Phi_{2^n}^+|_{AB} &= |\Phi_2^+\rangle\langle\Phi_2^+|_{AB} \otimes \dots \otimes |\Phi_2^+\rangle\langle\Phi_2^+|_{AB} \\ &= \left(\frac{1}{4} \sum_{P_1 \in \{I, X, Y, Z\}} P_{1,A} \otimes (P_{1,B})^T \right) \otimes \dots \otimes \left(\frac{1}{4} \sum_{P_n \in \{I, X, Y, Z\}} P_{n,A} \otimes (P_{n,B})^T \right) \\ &= \frac{1}{4^n} \sum_{P_1, \dots, P_n \in \{I, X, Y, Z\}} P_{1,A} \otimes (P_{1,B})^T \otimes \dots \otimes P_{n,A} \otimes (P_{n,B})^T \\ &= \frac{1}{4^n} \sum_{P_1, \dots, P_n \in \{I, X, Y, Z\}} [P_{1,A} \otimes \dots \otimes P_{n,A}] \otimes [P_{1,B} \otimes \dots \otimes P_{n,B}]^T \\ &= \frac{1}{D^2} \sum_{P \in \{I, X, Y, Z\}^{\otimes n}} P_A \otimes (P_B)^T \end{aligned} \quad (\text{S24})$$

where $D = 2^n$ and $D^2 = 4^n$. An n -qubit Pauli channel acts as,

$$\mathcal{E}_{\text{Pauli}}(\rho) = \sum_{i=0}^{D^2-1} \theta_i P_i \rho P_i^\dagger \quad (\text{S25})$$

where $\{P_i\}$ are n -qubit Pauli operators. The Choi matrix is:

$$\begin{aligned} J_{\text{Pauli}} &= (\mathcal{E}_{\text{Pauli}} \otimes \mathbf{1})(|\Phi_{2^n}^+\rangle\langle\Phi_{2^n}^+|) \\ &= \sum_{i=0}^{D^2-1} \theta_i (P_i \otimes \mathbf{1}) \left(\frac{1}{D^2} \sum_{P \in \{I, X, Y, Z\}^{\otimes n}} P \otimes P^T \right) (P_i^\dagger \otimes \mathbf{1}). \end{aligned} \quad (\text{S26})$$

Using the identity $\langle\Phi^+|(A \otimes \mathbf{1}) = \langle\Phi^+|(\mathbf{1} \otimes A^T)$, and since $P_i^T = \bar{P}_i$,

$$\begin{aligned} J_{\text{Pauli}} &= \sum_{i=0}^{D^2-1} \theta_i (P_i \otimes \mathbf{1}) \left(\frac{1}{D^2} \sum_{P \in \{I, X, Y, Z\}^{\otimes n}} P \otimes P^T \right) (\mathbf{1} \otimes \bar{P}_i) \\ &= \frac{1}{D^2} \sum_{i=0}^{D^2-1} \sum_{P \in \{I, X, Y, Z\}^{\otimes n}} \theta_i (P_i P) \otimes (\bar{P}_i \bar{P}). \end{aligned} \quad (\text{S27})$$

The filter function channel including both dissipative and coherent contributions is

$$\mathcal{E}_{\text{FF}}(\rho) = \rho - i[H_{\text{coh}}, \rho] + \sum_{\alpha=1}^M \sum_{k,l=0}^{D^2-1} \Gamma_{\alpha,kl} \left(\sigma_k \rho \sigma_l - \frac{1}{2} \{ \sigma_k \sigma_l, \rho \} \right), \quad (\text{S28})$$

where $\Gamma_{\alpha,kl} = \int_0^\tau dt_1 \int_0^\tau dt_2 C_\alpha(t_1 - t_2) \tilde{B}_{\alpha k}(t_1) \tilde{B}_{\alpha l}(t_2)$ is the symmetric part of the noise kernel, and the coherent Hamiltonian is induced by $\mathbb{E}[[H_{\text{eff};2}, \rho]]$. The Choi matrix is

$$J_{\text{FF}} = (\mathcal{E}_{\text{FF}} \otimes \mathbb{1})(|\Phi_{2^n}^+\rangle \langle \Phi_{2^n}^+|). \quad (\text{S29})$$

Express it in Pauli basis,

$$J_{\text{FF}} = (\mathcal{E}_{\text{FF}} \otimes \mathbb{1}) \left(\frac{1}{D^2} \sum_{r=0}^{D^2-1} P_r \otimes \bar{P}_r \right) = \frac{1}{D^2} \sum_{r=0}^{D^2-1} [\mathcal{E}_{\text{FF}}(P_r) \otimes \bar{P}_r] \quad (\text{S30})$$

Using the definition of \mathcal{E}_{FF}

$$\mathcal{E}_{\text{FF}}(P_r) = P_r - i[H_{\text{coh}}, P_r] + \sum_{\alpha=1}^M \sum_{k,l=0}^{D^2-1} \Gamma_{\alpha,kl} \left(\sigma_k P_r \sigma_l - \frac{1}{2} \{ \sigma_k \sigma_l, P_r \} \right) \quad (\text{S31})$$

so that

$$J_{\text{FF}} = \frac{1}{D^2} \sum_{r=0}^{D^2-1} \left[P_r \otimes \bar{P}_r - i[H_{\text{coh}}, P_r] \otimes \bar{P}_r + \sum_{\alpha=1}^M \sum_{k,l=0}^{D^2-1} \Gamma_{\alpha,kl} \left(\sigma_k P_r \sigma_l \otimes \bar{P}_r - \frac{1}{2} \{ \sigma_k \sigma_l, P_r \} \otimes \bar{P}_r \right) \right]. \quad (\text{S32})$$

We want to write J_{FF} in the Pauli basis $\{P_p \otimes \bar{P}_q\}$

$$J_{\text{FF}} = \frac{1}{D^2} \sum_{p,q=0}^{D^2-1} J_{pq} (P_p \otimes \bar{P}_q). \quad (\text{S33})$$

Our goal is to seek Pauli channel parameters $\{\theta_i\}_{i=0}^{D^2-1}$ that minimize,

$$\mathcal{L}(\boldsymbol{\theta}, \lambda_1, \lambda_2) = d_F(J_{\text{FF}}, J_{\text{Pauli}}(\boldsymbol{\theta})) + \lambda_1 (\mathcal{F}_{\text{FF}} - \mathcal{F}_{\text{Pauli}}(\boldsymbol{\theta})) + \lambda_2 \left(\sum_{i=0}^{D^2-1} \theta_i - 1 \right) \quad (\text{S34})$$

where

- d_F is the Frobenius norm distance
- λ_1, λ_2 are Lagrange multipliers for constraints
- \mathcal{F}_{FF} and $\mathcal{F}_{\text{Pauli}}$ are the process fidelities

The constraints are

$$\mathcal{F}_{\text{FF}} - \mathcal{F}_{\text{Pauli}}(\boldsymbol{\theta}) = 0 \quad (\text{fidelity matching}) \quad (\text{S35})$$

$$\sum_{i=0}^{D^2-1} \theta_i = 1 \quad (\text{normalization}) \quad (\text{S36})$$

We consider the first term,

$$d_F(J_1, J_2) = \|J_1 - J_2\|_F^2 = \text{tr}[(J_1 - J_2)^\dagger (J_1 - J_2)]. \quad (\text{S37})$$

Expanding

$$d_F = \underbrace{\text{tr}(J_{\text{FF}}^\dagger J_{\text{FF}})}_{T_1} + \underbrace{\text{tr}(J_{\text{Pauli}}(\boldsymbol{\theta})^\dagger J_{\text{Pauli}}(\boldsymbol{\theta}))}_{T_2} - 2 \underbrace{\text{Re}[\text{tr}(J_{\text{FF}}^\dagger J_{\text{Pauli}}(\boldsymbol{\theta}))]}_{T_3}. \quad (\text{S38})$$

We do not explicitly calculate T_1 since it is a constant with respect to $\boldsymbol{\theta}$ though. Note that the Pauli strings are an orthonormal basis with respect to the Hilbert–Schmidt inner product. And since it is generally hard to evaluate the commutation rules with Pauli strings to simplify the notation, we choose to write $\boldsymbol{\theta}$ in the Pauli basis directly,

$$\begin{aligned} T_2 &= \text{tr} \left[\left(\frac{1}{D^2} \sum_{i=0}^{D^2-1} \theta_i \right)^\dagger \left(\frac{1}{D^2} \sum_{j=0}^{D^2-1} \theta_j \right) \right] \\ &= \frac{1}{D^4} \left(\sum_{i,j} \theta_i \theta_j \delta_{ij} \right) = \frac{1}{D^2} \sum_{i,j} \theta_i^2 \end{aligned} \quad (\text{S39})$$

For T_3

$$T_3 = \text{tr} \left[J_{\text{FF}}^\dagger J_{\text{Pauli}}(\boldsymbol{\theta}) \right] = \frac{1}{D^2} \sum_{i,j} \theta_i J_{ij} \quad (\text{S40})$$

Now, from

$$\mathcal{F}_{\text{FF}} = 1 - \frac{1}{d+1} \sum_{\alpha=1}^M \sum_{k=0}^{D^2-1} \Gamma_{\alpha,kk}, \quad (\text{S41})$$

we define

$$\gamma = \frac{1}{D} \sum_{\alpha=1}^M \sum_{k=0}^{D^2-1} \Gamma_{\alpha,kk}. \quad (\text{S42})$$

Then

$$\mathcal{F}_{\text{FF}} = 1 - \frac{d}{d+1} \gamma \equiv 1 - \kappa \gamma. \quad (\text{S43})$$

where $\kappa = \frac{d}{d+1}$. For the Pauli channel

$$\begin{aligned} \mathcal{F}_{\text{Pauli}}(\boldsymbol{\theta}) &= \frac{1}{d(d+1)} \left(d + \sum_{i=0}^{D^2-1} \theta_i |\text{tr}(P_i)|^2 \right) \\ &= \frac{1}{d(d+1)} (d + \theta_0 D^2) = \frac{1 + d\theta_0}{d+1}. \end{aligned} \quad (\text{S44})$$

Using $\theta_0 = 1 - \sum_{i=1}^{D^2-1} \theta_i$

$$\mathcal{F}_{\text{Pauli}}(\boldsymbol{\theta}) = \frac{1 + d(1 - \sum_{i=1}^{D^2-1} \theta_i)}{d+1} = 1 - \kappa \sum_{i=1}^{D^2-1} \theta_i. \quad (\text{S45})$$

Let us write down the full lagrangian

$$\mathcal{L}(\boldsymbol{\theta}, \lambda_1, \lambda_2) = \sum_{p,q} |J_{pq}|^2 + \frac{1}{D^2} \sum_{i=0}^{D^2-1} \theta_i^2 + \frac{1}{D^2} \sum_{i,j=0}^{D^2-1} \theta_i J_{ij} + \lambda_1 \kappa \left(\sum_{i=1}^{D^2-1} \theta_i - \gamma \right) + \lambda_2 \left(\sum_{i=0}^{D^2-1} \theta_i - 1 \right). \quad (\text{S46})$$

Next we want to calculate the stationary conditions. For $i = 0$,

$$\frac{\partial \mathcal{L}}{\partial \theta_0} = \frac{2}{D^2} \theta_0 + \frac{1}{D^2} J_{00}^* + \lambda_2 = 0 \implies \theta_0 = \frac{-1}{2} J_{00}^* - \frac{\lambda_2 D^2}{2}. \quad (\text{S47})$$

For $i \geq 1$,

$$\frac{\partial \mathcal{L}}{\partial \theta_i} = \frac{2}{D^2} \theta_i + \frac{1}{D^2} J_{ii}^* + \lambda_1 \kappa + \lambda_2 = 0 \quad (\text{S48})$$

$$\implies \theta_i = \frac{-1}{2} J_{ii}^* - D^2 \frac{\lambda_1 \kappa + \lambda_2}{2}. \quad (\text{S49})$$

Let $S = \sum_{i=1}^{D^2-1} \theta_i$. The normalization constraint $\sum_{i=0}^{D^2-1} \theta_i = 1$ gives

$$\theta_0 + S = 1 \implies \frac{-1}{2} \sum_i^{D^2-1} J_{ii}^* - \frac{\lambda_2 D^2}{2} - (D^2 - 1) D^2 \frac{\lambda_1 \kappa + \lambda_2}{2} = 1. \quad (\text{S50})$$

The fidelity constraint $\mathcal{F}_{\text{FF}} = \mathcal{F}_{\text{Pauli}}(\boldsymbol{\theta})$ gives

$$1 - \kappa\gamma = 1 - \kappa S \implies S = \gamma, \quad (\text{S51})$$

which leads to

$$\gamma = \frac{-1}{2} \sum_{i=1}^{D^2-1} J_{ii}^* - D^2 (D^2 - 1) \frac{\lambda_1 \kappa + \lambda_2}{2}. \quad (\text{S52})$$

Let $J_{\text{sum}}^* = \sum_{i=0}^{D^2-1} J_{ii}^*$. Then

$$-\frac{1}{2} J_{\text{sum}}^* - \frac{D^2}{2} \lambda_2 - \frac{D^2}{2} (D^2 - 1) (\lambda_1 \kappa + \lambda_2) = 1. \quad (\text{S53})$$

Now solve for λ_1 and λ_2

$$\lambda_1 \kappa + \lambda_2 = -\frac{1}{D^2 (D^2 - 1)} \left(\sum_{i=1}^{D^2-1} J_{ii}^* + 2\gamma \right). \quad (\text{S54})$$

Make a substitution

$$-\frac{1}{2} J_{\text{sum}}^* - \frac{D^2}{2} \lambda_2 - \frac{1}{2} D^2 (D^2 - 1) \left[-\frac{1}{D^2 (D^2 - 1)} \left(\sum_{i=1}^{D^2-1} J_{ii}^* + 2\gamma \right) \right] = 1. \quad (\text{S55})$$

Simplify the third term

$$-\frac{1}{2} J_{\text{sum}}^* - \frac{D^2}{2} \lambda_2 + \frac{1}{2} \sum_{i=1}^{D^2-1} J_{ii}^* + \gamma = 1. \quad (\text{S56})$$

Note that $J_{\text{sum}}^* = J_{00}^* + \sum_{i=1}^{D^2-1} J_{ii}^*$, so,

$$-\frac{1}{2} J_{00}^* - \frac{D^2}{2} \lambda_2 + \gamma = 1. \quad (\text{S57})$$

Solving for λ_2

$$\lambda_2 = (2\gamma - 2 - J_{00}^*) / D^2. \quad (\text{S58})$$

Now for λ_1 ,

$$\lambda_1 \kappa = -\frac{1}{D^2 (D^2 - 1)} \left(\sum_{i=1}^{D^2-1} J_{ii}^* + 2\gamma \right) - \lambda_2. \quad (\text{S59})$$

Substitute λ_2 ,

$$\lambda_1 = -\frac{1}{\kappa D^2 (D^2 - 1)} \left(\sum_{i=1}^{D^2-1} J_{ii}^* + 2\gamma \right) + \frac{2\gamma - J_{00}^* - 2}{D^2 \kappa}. \quad (\text{S60})$$

Now we can solve for theta using the setup here with the analytical form of λ_1 and λ_2 .

III. SUPPLEMENTARY DATA

In this appendix, we give all the data simulated in the Sec. VI B. First, we show the space-time overhead for the dense architecture in Fig. 1. Compared to the sparse layout's space-time overhead, the trend is very similar, but we obtain about an order-of-magnitude reduction.

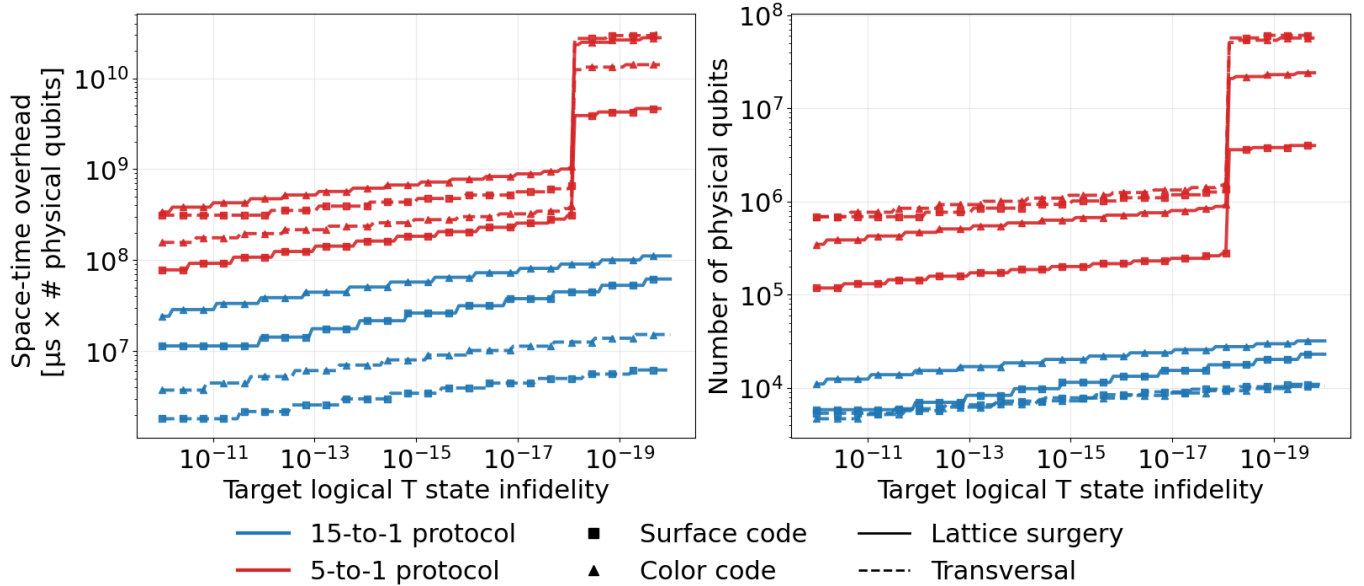


FIG. 1. Experimental space-time overhead data plot for the dense layout where the label shows three different setups: red for the $5 \rightarrow 1$ distillation protocol and blue for the $15 \rightarrow 1$ distillation protocol; dotted line for transversal operation and solid line for lattice surgery-based operation; triangular marker for the surface code and circular marker for the color code. The noise parameters here are chosen according to Tab. I. On the vertical axis, we show the number of physical qubits (right) as well as the space-time overhead (left) with the time in units of μs . And on the horizontal axis, we have the targeted logical infidelity for the logical T state.

Next, we present parameter sweeps of hardware values in the following figures for all three architectures. These data are for the interested reader to compare different architectural choices and QEC setups.

A. Dense architecture data

The figures on this page and the next show the space-time overhead for the dense layout with the $5 \rightarrow 1$ and $15 \rightarrow 1$ MSD protocol, respectively (complementary to Fig. 14 in the main text).

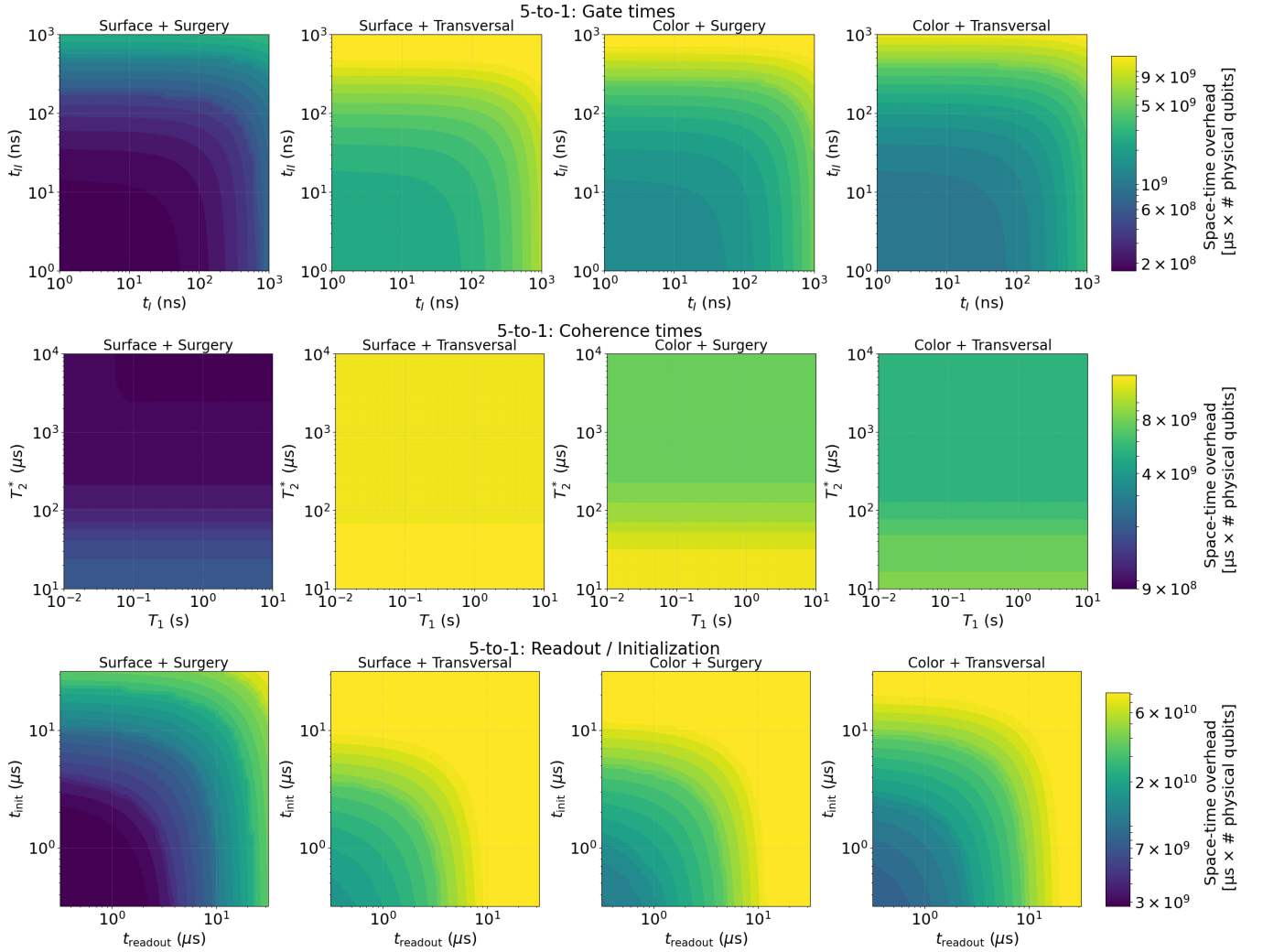


FIG. 2. Space-time overhead for the dense architecture using $5 \rightarrow 1$ MSD as a function of gate times (top row), coherence times (middle row), and readout and initialization times (bottom row). The four columns from left to right correspond to the surface code with lattice surgery and transversal operations, and the color code with lattice surgery and transversal operations, respectively.

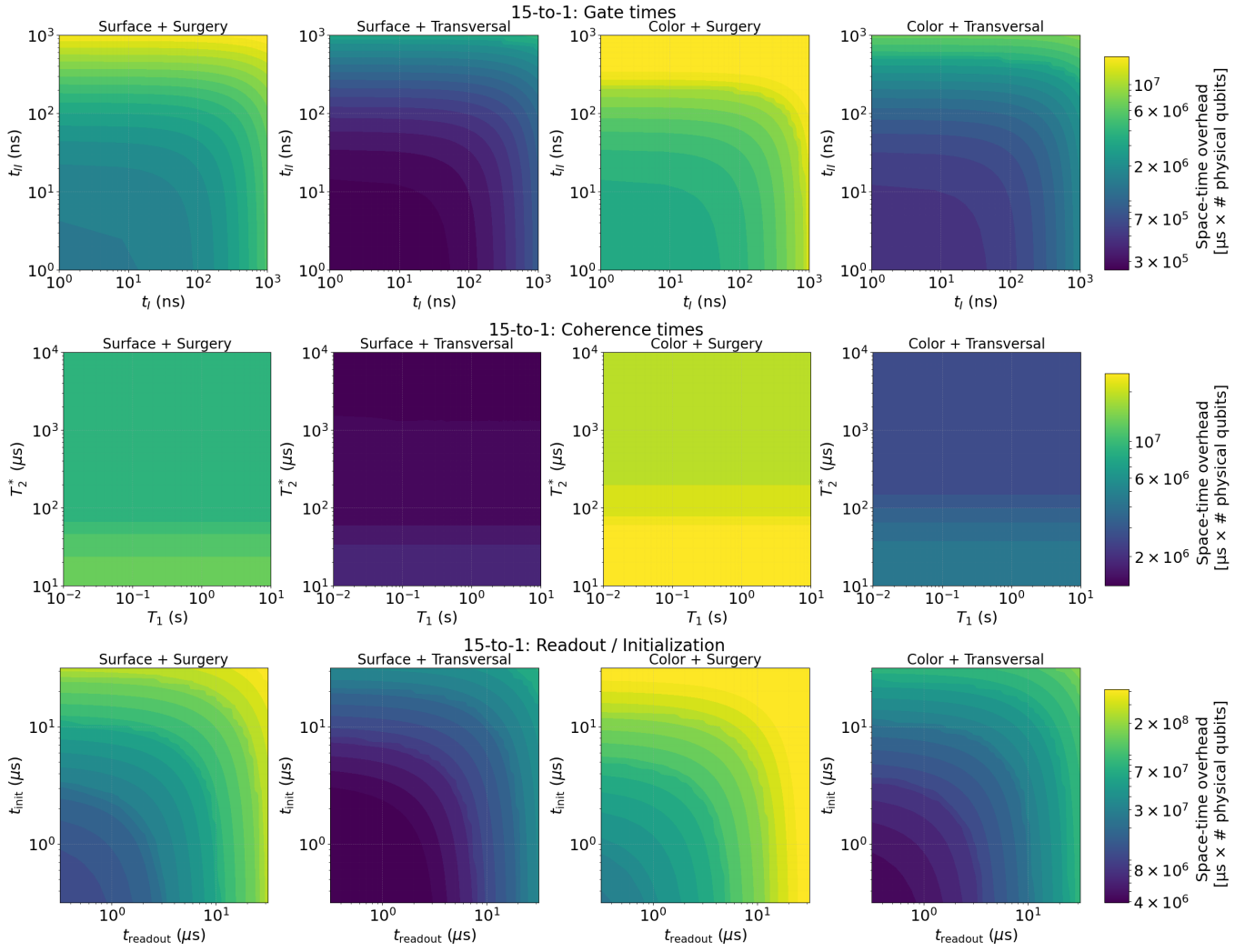


FIG. 3. Space-time overhead for the dense architecture using $15 \rightarrow 1$ MSD as a function of gate times (top row), coherence times (middle row), and readout and initialization times (bottom row). The four columns from left to right correspond to the surface code with lattice surgery and transversal operations, and the color code with lattice surgery and transversal operations, respectively.

B. Sparse architecture data

The figures on this page and the next show the space-time overhead for the sparse layout with the $5 \rightarrow 1$ and $15 \rightarrow 1$ MSD protocol, respectively (complementary to Fig. 14 in the main text).

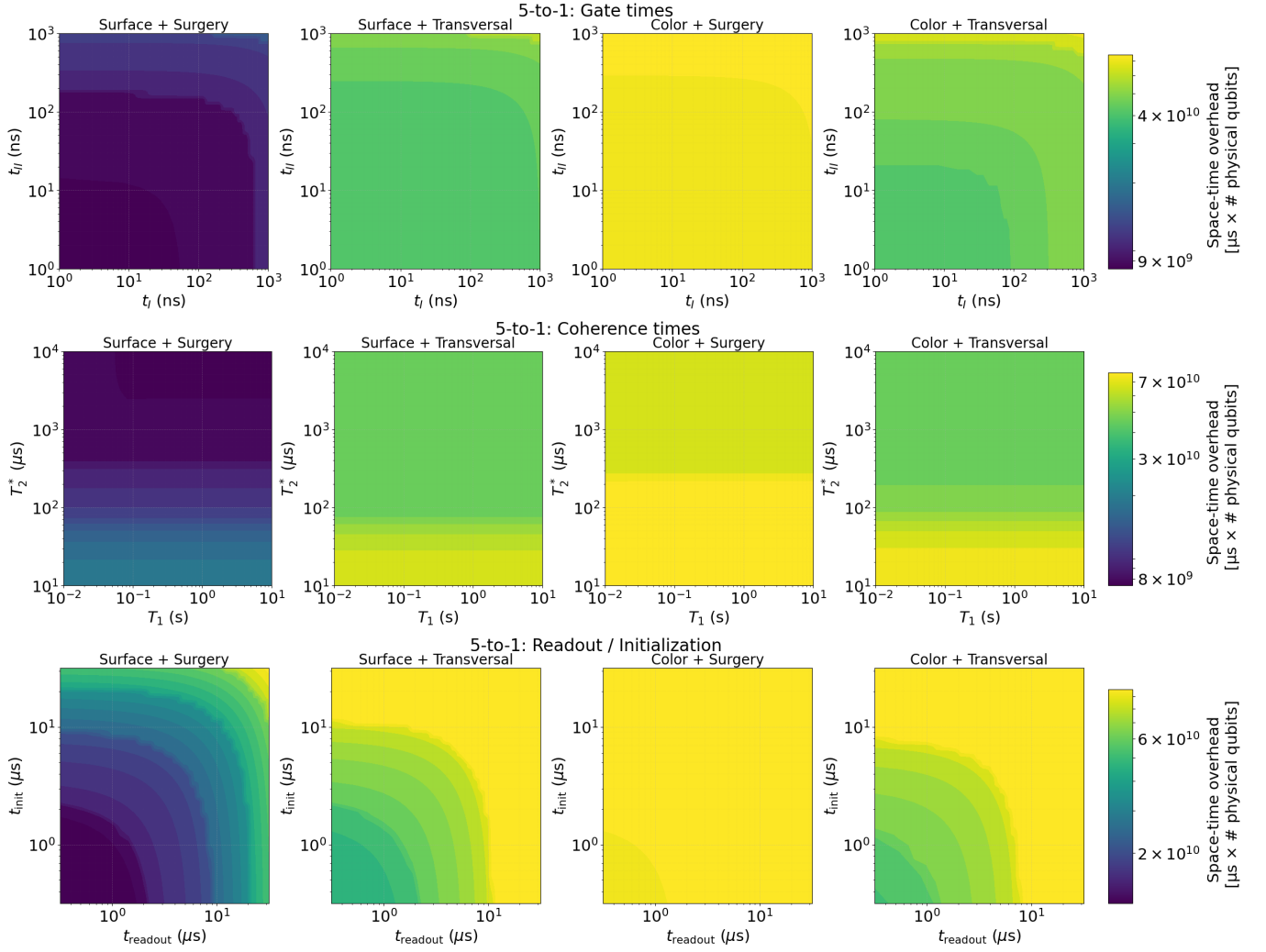


FIG. 4. Space-time overhead for the sparse architecture using $5 \rightarrow 1$ MSD as a function of gate times (top row), coherence times (middle row), and readout and initialization times (bottom row). The four columns from left to right correspond to the surface code with lattice surgery and transversal operations, and the color code with lattice surgery and transversal operations, respectively.

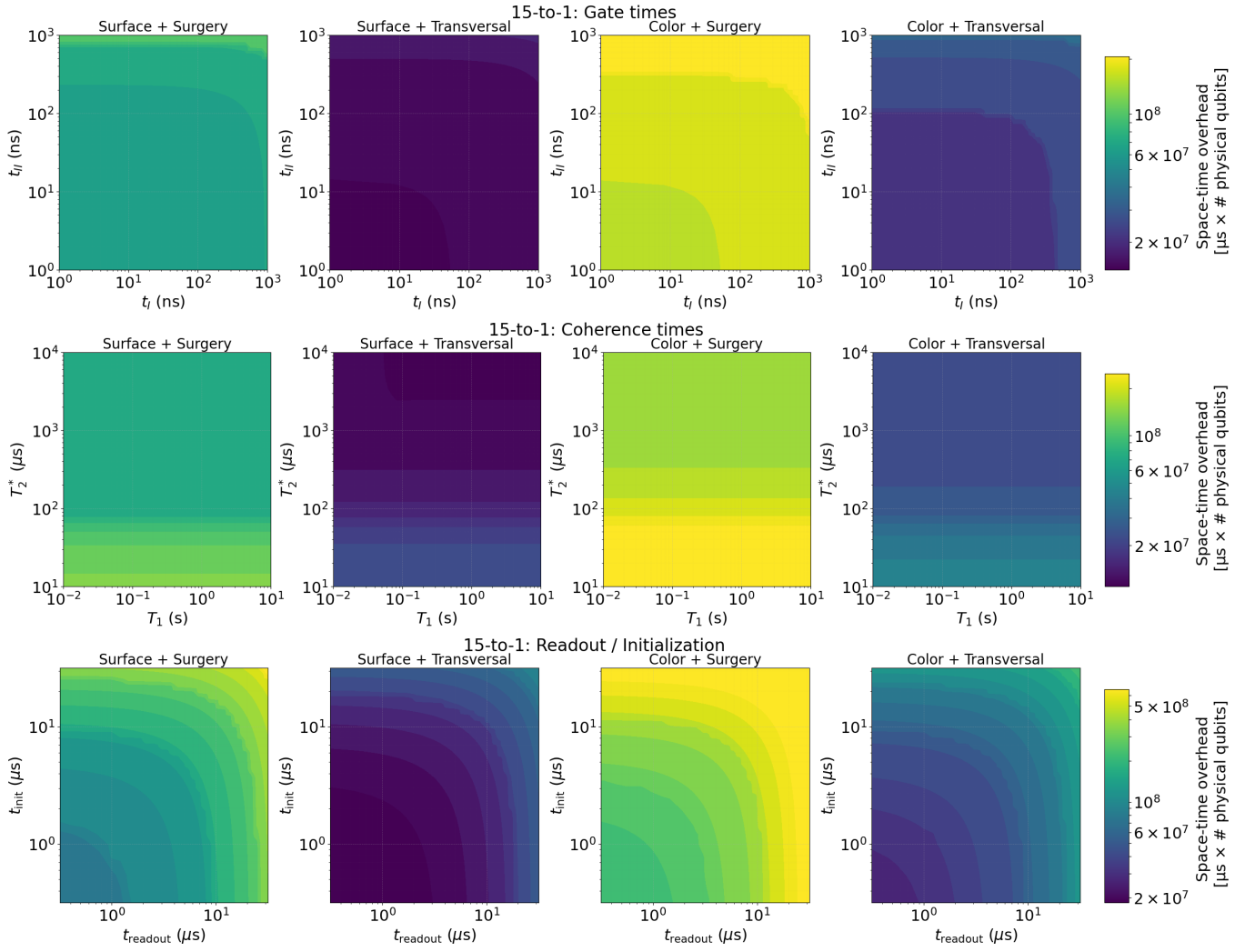


FIG. 5. Space-time overhead for the sparse architecture using $15 \rightarrow 1$ MSD as a function of gate times (top row), coherence times (middle row), and readout and initialization times (bottom row). The four columns from left to right correspond to the surface code with lattice surgery and transversal operations, and the color code with lattice surgery and transversal operations, respectively.

C. Patched architecture data

The figures on this page and the next show the space-time overhead for the patched layout with 2 logical qubits per patch, using the $5 \rightarrow 1$ and $15 \rightarrow 1$ MSD protocols, respectively (complementary to Fig. 14 in the main text).

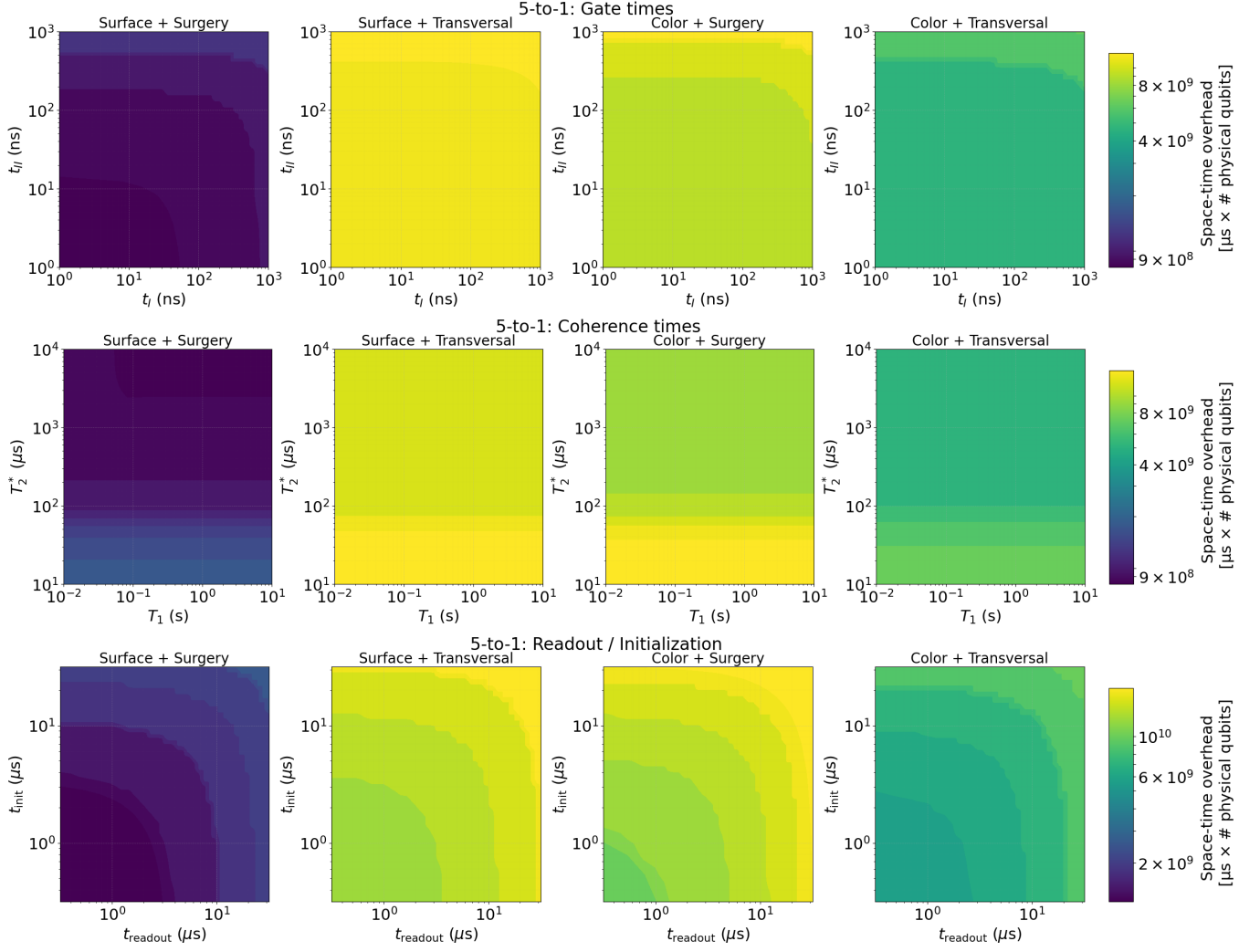


FIG. 6. Space-time overhead for the patched architecture using $5 \rightarrow 1$ MSD with 2 logical qubits as a function of gate times (top row), coherence times (middle row), and readout and initialization times (bottom row). The four columns from left to right correspond to the surface code with lattice surgery and transversal operations, and the color code with lattice surgery and transversal operations, respectively.

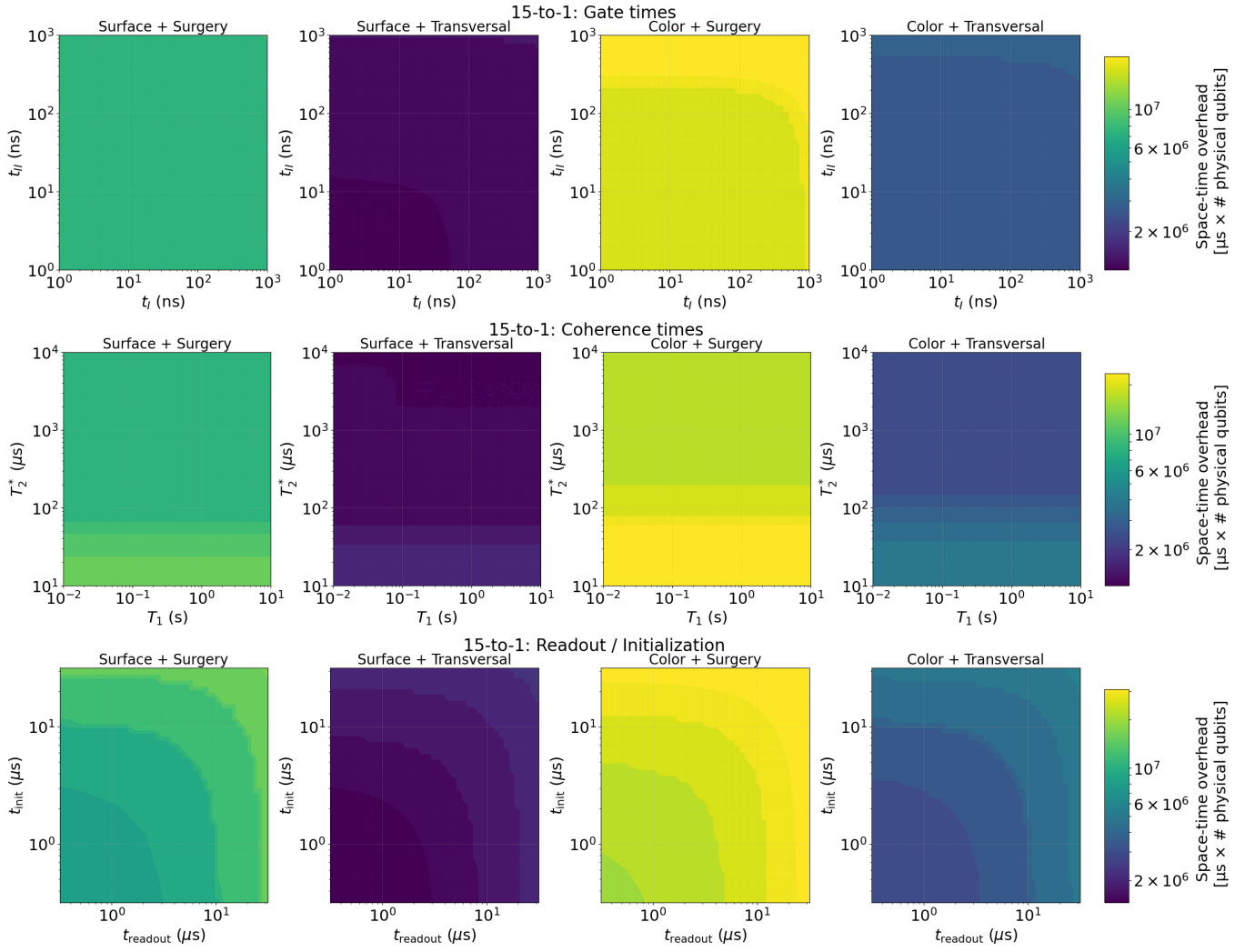


FIG. 7. Space-time overhead for the dense architecture using $15 \rightarrow 1$ MSD with 2 logical qubits as a function of gate times (top row), coherence times (middle row), and readout and initialization times (bottom row). The four columns from left to right correspond to the surface code with lattice surgery and transversal operations, and the color code with lattice surgery and transversal operations, respectively.